

## Mars high resolution gravity fields from MRO, Mars seasonal gravity, and other dynamical parameters

Alex S. Konopliv<sup>a,\*</sup>, Sami W. Asmar<sup>a</sup>, William M. Folkner<sup>a</sup>, Özgür Karatekin<sup>b</sup>, Daniel C. Nunes<sup>a</sup>, Suzanne E. Smrekar<sup>a</sup>, Charles F. Yoder<sup>a</sup>, Maria T. Zuber<sup>c</sup>

<sup>a</sup>Jet Propulsion Laboratory, California Institute of Technology, Pasadena, CA 91109, United States

<sup>b</sup>Royal Observatory of Belgium, Av. Circulaire, 3, B-1180 Brussels, Belgium

<sup>c</sup>Department of Earth, Atmospheric and Planetary Sciences, Massachusetts Institute of Technology, Cambridge, MA 02139, United States

### ARTICLE INFO

#### Article history:

Received 20 August 2009

Revised 6 October 2010

Accepted 12 October 2010

Available online 16 October 2010

#### Keywords:

Mars, Interior

Geophysics

Planetary dynamics

Asteroids

### ABSTRACT

With 2 years of tracking data collection from the MRO spacecraft, there is noticeable improvement in the high frequency portion of the spherical harmonic Mars gravity field. The new JPL Mars gravity fields, MRO110B and MRO110B2, show resolution near degree 90. Additional years of MGS and Mars Odyssey tracking data result in improvement for the seasonal  $\bar{J}_3$  gravity changes which compares well to global circulation models and Odyssey neutron data and Mars rotation and precession ( $\dot{\psi} = -7594 \pm 10$  mas/year). Once atmospheric dust is accounted for in the spacecraft solar pressure model, solutions for Mars solar tide are consistent between data sets and show slightly larger values ( $k_2 = 0.164 \pm 0.009$ , after correction for atmospheric tide) compared to previous results, further constraining core models. An additional 4 years of Mars range data improves the Mars ephemeris, determines 21 asteroid masses and bounds solar mass loss ( $dGM_{Sun}/dt < 1.6 \times 10^{-13} GM_{Sun} \text{ year}^{-1}$ ).

© 2010 Elsevier Inc. All rights reserved.

### 1. Introduction

At the end of August 2006, The Mars Reconnaissance Orbiter (MRO) mission began collecting tracking data for the radio science gravity investigation (Zuber et al., 2007), and has acquired more than 2 years of global gravity data. The lower altitude of the MRO spacecraft (255 km periapse) enables a higher resolution gravity field model determination than previous models (Smith et al., 1999a; Lemoine et al., 2001; Yuan et al., 2001; Konopliv et al., 2006; Marty et al., 2009) based upon the higher altitude MGS and Mars Odyssey orbits. These previous spherical harmonic solutions are determined to at most degree 95 (spatial resolution = 112 km), but the global resolution, defined as the degree where the average coefficient magnitude equals the uncertainty, is limited to about degree 70 (spatial resolution = 152 km) due to the approximate 400 km altitude of MGS and Odyssey.

Several new global gravity solutions have been determined at JPL using the MRO tracking data by building on the previous MGS and Odyssey gravity solution MGS95J (Konopliv et al., 2006). The first solution, MRO95A to degree and order 95, uses the first year of MRO tracking data through August 2007 in combination with the entire MGS data set through September 2006 (contact with MGS was lost in November 2006), and Mars Odyssey data

to the same end time as MRO. The second solution set, MRO110B and MRO110B2 to degree and order 110, uses more than an additional year of MRO and Mars Odyssey tracking data through October 2008. The newer MRO95A, MRO110B, MRO110B2 models have a resolution of near degree 85 and 90 (or 120 km at the surface), respectively. These JPL models are archived with the Planetary Data System (PDS) Geosciences Node ([www.pds.wustl.edu](http://www.pds.wustl.edu)) under the MRO gravity science archive.

The time variations of the zonal gravity coefficients due to the CO<sub>2</sub> seasonal mass exchange between the southern and northern caps has been modeled based upon Mars global circulation models (GCM) and Odyssey neutron data (Smith et al., 1999b; Karatekin et al., 2005; Sanchez et al., 2006), and measured with MGS and Mars Odyssey tracking data (Smith et al., 2001a, 2009; Yoder et al., 2003; Balmino et al., 2005; Konopliv et al., 2006; Marty et al., 2009). Here, we give an updated solution to the seasonal gravity variations for a combination of even zonals (as represented by  $J_2$ ) and odd zonals (as given by  $J_3$ ) based only upon the MGS and Mars Odyssey tracking data. The MGS and Odyssey odd zonal solution is compared extensively to GCM predictions and Odyssey neutron data. Reasonable recovery of seasonal gravity of any zonal coefficients from MRO tracking data has not been successful with current spacecraft modeling assumptions.

The measurement of the solar tide from the MGS tracking data indicates an outer liquid Mars core (Yoder et al., 2003,  $k_2 = 0.153$ ). Subsequent studies have indicated a slightly larger Love number

\* Corresponding author. Fax: +1 818 393 6388.

E-mail address: [Alex.Konopliv@jpl.nasa.gov](mailto:Alex.Konopliv@jpl.nasa.gov) (A.S. Konopliv).

(Lemoine et al., 2006), whereas others are slightly smaller (Balmino et al., 2005; Marty et al., 2009), but all supporting a liquid core interpretation. Our previous results from Odyssey were smaller and indicated perhaps problems from the spacecraft thrusters (Konopliv et al., 2006). Further analysis presented here shows previous values were too low due to Mars atmospheric dust. Solutions for MRO110B from all three spacecraft, MGS, Odyssey, and MRO, now show a consistent but slightly larger Love number.

An accurate Mars orientation model initially developed to process the Mars Pathfinder lander data (Folkner et al., 1997) significantly improved the Mars gravity field MGS95J (Konopliv et al., 2006). With the corrections for nutations and spin variations, the surface errors in the pole and prime meridian over a 20-year time span reduced from about 40 m for the IAU 2000 representation (Seidelmann et al., 2002) to about 2 m. The gravity solutions presented in this paper continue to improve the orientation of Mars (precession, spin rate, and seasonal spin) by estimating the orientation jointly with the gravity field.

The MGS and Mars Odyssey 1-m accurate range data were used previously to improve the planetary ephemeris and estimate several asteroid masses (Konopliv et al., 2006). The latest results include four additional years of Mars Odyssey and MRO range data. Once corrected for spacecraft position, the Mars–Earth range from the MRO range data are of comparable accuracy to that of Mars Odyssey and MGS range data.

## 2. Spacecraft data and calibrations

On September 11, 2006, the MRO spacecraft was placed in a polar ( $i = 92.5^\circ$ ) frozen orbit configuration similar to MGS and Mars Odyssey except with a lower periape altitude of 255 km over the south pole and apoapse altitude of 320 km over the north pole (see Fig. 1). Prior to the frozen orbit, MRO collected tracking data for 13 days during the transition orbit from August 30 to September 11, 2006. During a portion of this time, lower altitude ( $\sim 220$  km) tracking of MRO was collected while the spacecraft was tracked over the northern hemisphere.

The MRO tracking data consists of 2-way and 3-way coherent X-band Doppler data from the Deep Space Network (DSN), where 3-way indicates a different receive DSN station from the transmit DSN station. The MRO 1-way data is not included in the gravity solution, since the noise of the MRO 1-way data is about five times greater than the 2-way MRO data or 1-way MGS data due to the poorer MRO spacecraft oscillator stability ( $10^{-12}$ ) versus MGS ( $10^{-13}$ ). The MRO uplink frequency of about 7.18 GHz is coherently

multiplied in the transponder by 880/749, which gives the downlink frequency. The X-band MGS and Odyssey uplink frequencies are about 7.16 GHz and 7.15 GHz, respectively. All tracking of MRO in the gravity solution uses the 3-m diameter high gain antenna (HGA) attached to a gimbal. The MRO HGA was deployed on August 12, 2005, shortly after launch, whereas the 1.5-m diameter MGS and 1.3-m diameter Odyssey HGAs were deployed just before mapping on March 29, 1999 and February 7, 2002, respectively. The motion of all three spacecraft antennas are modeled using the time tabulated inner and outer gimbal angle values (Semenov et al., 1998, 2004; Semenov and Acton, 2007). The distance from the MRO HGA gimbal location (0.0,  $-3.15$ ,  $-1.52$  m in the spacecraft coordinate frame) to the center of the HGA rim is 1.4 m. The movement of this moment arm relative to the spacecraft center-of-mass (0.0,  $-1.11$ , 0.0 m) must be accounted for in the Doppler and range data. The HGA signature in the Doppler data is periodic (2 h) with amplitudes near 1 mm/s. The origin of the spacecraft frame is at the center of the main engine base-plate with +Y in the thrust direction, the X axis along the solar array locations, and +Z points toward nadir along with the instruments.

The typical X-band MRO accuracy is better than 0.1 mm/s for 10-s samples, and the data noise is comparable to that of MGS, but it is greater than the high quality Odyssey data. The superiority of the Odyssey data is shown in Fig. 2 where the RMS of the 2-way X-band data for each data arc for each spacecraft is shown versus the Sun–Earth–Mars angle. The average RMS data noise for Sun–Earth–Mars angles  $>60^\circ$  is 0.053, 0.056, 0.040 mm/s for 10-s samples for MRO, MGS, and Mars Odyssey, respectively. The noise of the Odyssey data is nearly one-half the noise of the other spacecraft for larger Sun angles ( $>120^\circ$ ). The MRO noise is increased by some unknown spacecraft or transponder periodic signature with periods near 4–5 s. Although the weighted residuals can be reduced by up to 25% using a more optimal sample time (4-s vs. 10-s, see Fig. 2), a test gravity solution with a portion of the data using 4-s samples is not noticeably improved, likely because the error source is of high frequency.

The summary of the tracking data included in the MRO110B and MRO110B2 gravity fields is given in Table 1. This data set includes all the data used for the MGS95J gravity field (Konopliv et al., 2006) with data from the MGS and Mars Odyssey orbiters as well as the Mars Pathfinder and Viking landers. The additional tracking data for MRO110B and MRO110B2 includes almost 2 years of extra MGS data to the end of mission, nearly four more years of Mars Odyssey data, and all the MRO data through October 2008. All the spacecraft orbit data are processed in time intervals (or data

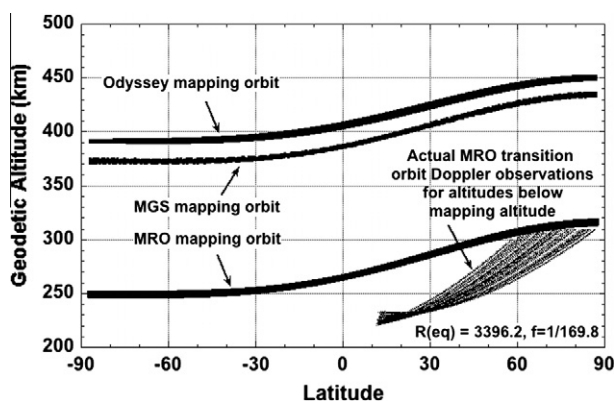


Fig. 1. The geodetic mapping altitude of all three Mars orbiters. As was the case with Mars Odyssey (see Konopliv et al., 2006), MRO was tracked for a brief period before mapping with an altitude below the mapping altitude. The actual observations occur in the northern hemisphere but with slightly larger data noise (0.1 mm/s) due to the small Sun–Earth–Mars angle.

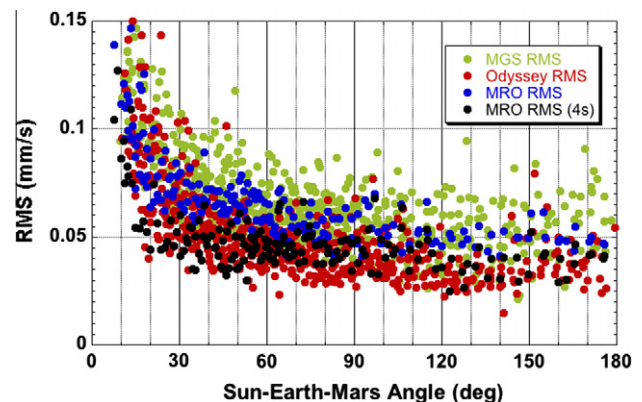


Fig. 2. DSN 2-way Doppler residual noise for each data arc for each spacecraft as a function of the Sun–Earth–Mars angle. The Doppler data RMS are shown for 10-s samples. An additional RMS is shown for mostly 4-s MRO Doppler data normalized to 10-s that removes the majority of the high frequency periodic signature. Mars Odyssey displays the highest quality Doppler data. The higher MGS data noise was in part caused by HGA jitter and the same may be true for MRO.

**Table 1**

Summary of the Doppler and range tracking data used in the MRO110B and MRO110B2 gravity solutions.

Spacecraft	Begin time, mm-dd-yy	End time, mm-dd-yy	Number of arcs	Number of 1-way Doppler	Number of 2-way Doppler	Number of 3-way Doppler	Number of range
MGS	03-28-98	09-23-06	611	3,844,863	4,139,924	329,404	170,657
Odyssey	01-11-02	10-28-08	553		6,048,298	1,161,887	303,648
MRO	08-30-06	10-31-08	188		2,617,596	227,678	13,741
Pathfinder	07-04-97	10-07-97	1		6928	635	167
Viking landers	07-21-76	11-13-82	2		14,450	0	1255

arcs) of 4–6 days in length. There is good DSN coverage for MRO with partial or full tracking for 75% of the orbits of a typical arc.

The range data from all three orbiters are included in the gravity solution, but they have a minimal contribution to gravity, orbit position, or Mars orientation. However, these range data measure the distance between the Earth and Mars centers to 1 or 2 m accuracy. These data significantly improve the planetary ephemeris and allow for estimation of asteroid masses and other parameters from their effect on the Mars orbit. The Mars Pathfinder and Viking Lander Doppler and range data dominate the determination of the Mars pole, precession, and spin. However, the spacecraft orbiting Doppler data also contribute to the Mars orientation solution.

The residual noise of the MRO range data after calibration is near 10–30 cm, and is comparable to the Odyssey range noise. The dominant error contribution to the range accuracy is the station specific range delay calibration or bias for the station electronics and is near 1–2 m. An important correction for the range data is the delay of the range due to the spacecraft electronics with almost all the delay due to the transponder and with small contributions due to the antenna. The range data use the following delay calibrations: MRO = 1414.9 ns, MGS = 779.7 ns, Odyssey = 1426.6 ns, and Mars Pathfinder = 420 ns. For the Viking landers, the transponder delay is unknown, but this delay may have been already applied in the range data. Since we are uncertain if this correction has been applied, we allow for a larger bias in the planetary ephemeris solutions.

All orbiting Doppler and range data are calibrated at each DSN complex for daily Earth dry and wet troposphere corrections and daily Earth ionosphere calibrations based upon GPS measurements. About 2 months of Doppler and range data are excluded from the global gravity solution near each Mars solar conjunction when the Doppler data noise is greater than about 0.2 mm/s. The solar conjunction dates are during July 2000, August 2002, September 2004, October 2006, and November 2008. The Doppler data are weighted individually for each spacecraft orbit based upon the RMS of the Doppler residuals.

### 3. Spacecraft force models

In order to recover the Mars gravity field and orientation, all the nonconservative forces acting on each spacecraft must be modeled accurately. The three major force models that limit long wavelength and temporal gravity recovery are atmospheric drag (e.g., Mazarico et al., 2007, 2009), solar radiation pressure, and spacecraft thrusting to despin or desaturate the angular momentum wheels (AMDs). Although not as large, a surface albedo model (Lemoine, 1992) is included but no parameters from the model such as scale factors are estimated. For MGS force comparisons, see Lemoine et al. (2006).

The solar pressure model consists of box-wing model with three plates representing the spacecraft bus and one (Odyssey) or two (MGS, MRO) for the solar panels, and a flat plate (MGS and Odyssey) or parabolic antenna model for the HGA (MRO). The orientation of each plate is determined from spacecraft telemetry and includes quaternions for spacecraft attitude in inertial space, qua-

ternions for each solar array attitude in the spacecraft frame, and HGA gimbal angles (e.g., Semenov and Acton, 2007 for MRO). The specular and diffuse coefficients for each plate are based upon combinations of surface types, and the solar panel reflectivity coefficients are estimated for MGS and Mars Odyssey. The solar pressure model from MRO was calibrated during cruise (You et al., 2007), and an energy balance calculation for the solar panel reflectivity coefficients accounts for thermal reradiation on the solar panel backside. For this reason, the MRO panel specular and diffuse coefficients are not estimated. An overall scaling factor for the solar pressure force (nominally 1.0) and two small (~2%) corrections for the directions normal to the Mars–Sun line are estimated for all three spacecraft for each data arc. As was done previously for MGS95J (Konopliv et al., 2006), Mars Odyssey and MRO solar pressure model adjustments are made to account for self-shadowing between spacecraft components (Mazarico et al., 2009). Areas of all spacecraft components are continuously adjusted during each orbit to account for shadows due to the solar panels and HGA on all other components. Shadowing on MGS is minimal.

Another aspect of the solar pressure model not previously understood appears to be the contribution of the atmospheric dust. The opacity due to Mars dust has significantly reduced the solar energy, for example, of the Mars Exploration Rovers, and also seems to significantly reduce the solar flux of Mars Odyssey as it passes near the limb of Mars. Due to the near face-on orbit as seen from the Sun, Mars Odyssey at times has an extended grazing occultation with the lower Mars atmosphere. The dust of Mars is known to extend at times to 80 km in the atmosphere (Clancy et al., 2008; Kahn et al., 1992), and dust is often collected in the equatorial band of Mars (Smith et al., 2001c; see also <http://tes.asu.edu/monitoringmars/index.html>). The inclination of the orbit relative to the plane-of-sky (or plane normal to the Sun or Earth directions) of all three spacecraft is shown in Fig. 3 (180° is face-on, 90° is edge-on). Only Mars Odyssey experiences the grazing occultation, and the effect is negligible for MGS and MRO. The minimum altitude of the ray path from the Sun and latitudes of the occultations, when they occur relative to an ellipsoid of the Mars surface, are shown for Mars Odyssey in Fig. 4.

The effect of the dust on Mars Odyssey is evident in the solution for periodic once per orbit accelerations in the orbit normal direction. In the MGS95J solution, these accelerations were used to absorb anomalous forces at a level of  $2 \times 10^{-12}$  km/s<sup>2</sup>, but are no longer used when corrections are made for dust (as for MRO110B). However, to show the effect of dust, the force solutions for each data arc are shown in Fig. 5 for two cases: the solutions with no correction for atmospheric dust, and solutions correcting for the dust by adjusting the solar pressure model with the spacecraft in shadow for the first 40 km above the Mars surface (i.e., increase the duration of solar occultation). Anomalous accelerations are evident for the times associated with grazing occultations near the Mars equator (10°N) on about March 1, 2004 and January 1, 2006, are small for the mid-latitude (25°N) occultation near November 1, 2007, and are not at all evident for the higher latitude occultations near 60°N. These times show moderate dust as displayed by the Mars Global Surveyor Thermal Emission Spectrometer (TES) dust

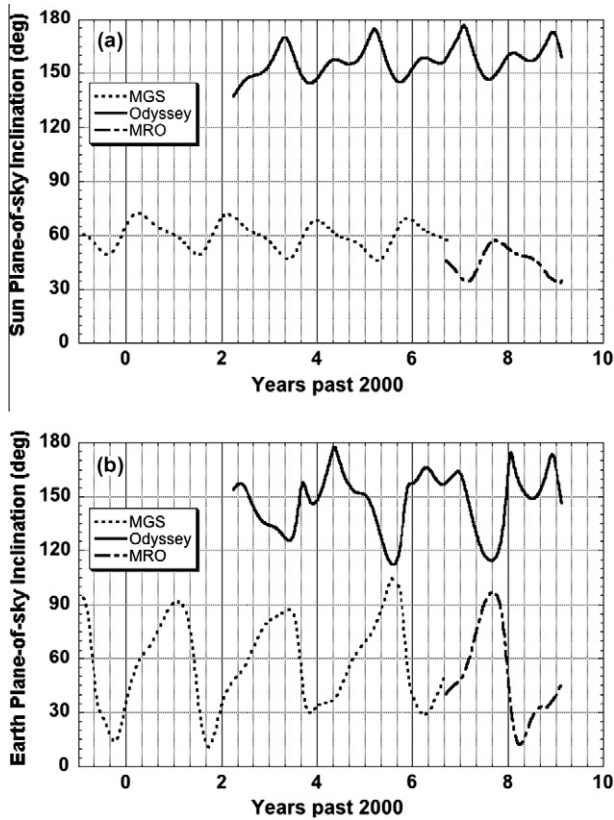


Fig. 3. The inclination of the Mars orbiters relative to the plane normal to the (a) Sun–Mars and (b) Earth–Mars directions (or plane-of-sky). The view of the orbit from the Sun or Earth is face-on for values of 0° and 180°, and the orbit is edge-on for 90°. Note the Odyssey orbit is the closest to being face-on as viewed from the Sun, resulting in its sensitivity to atmospheric dust shadowing for the solar pressure model.

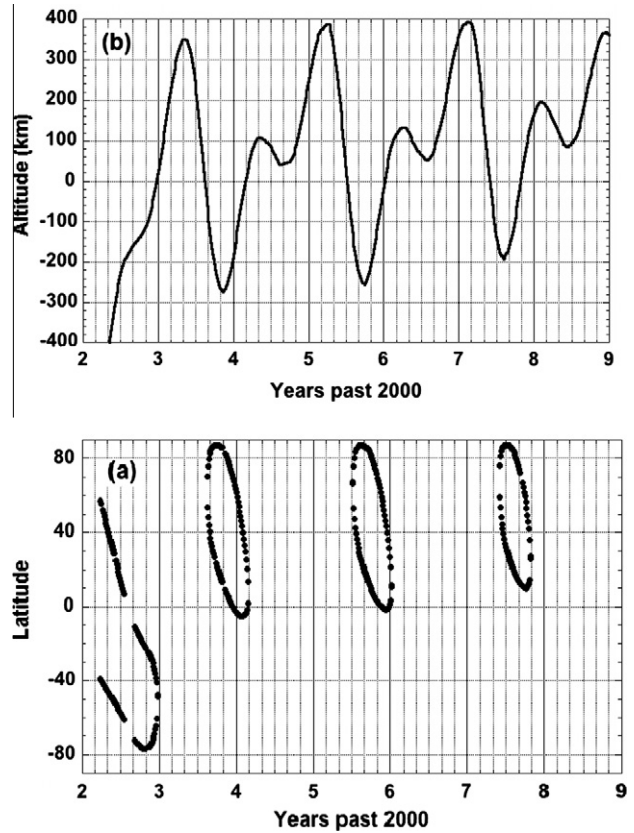


Fig. 4. The Mars Odyssey orbit geometry relative to the Sun displayed as (a) minimum ray path altitude and (b) occultation latitudes. For ray path altitudes of zero, Mars Odyssey has a grazing occultation as viewed from the Sun. For these times, the effect of shadowing on the spacecraft from atmospheric dust is potentially the greatest. For ray path altitudes less than zero, the spacecraft enters Mars shadow at the given latitudes.

movies (Christensen et al., 2001; see also <http://tes.asu.edu/monitoringmars/index.html>).

The atmospheric drag model has a dramatic effect on the Mars Odyssey Love number solution, which is driven by the secular change in orbit inclination (Yoder et al., 2003). The solar tide causes an orbit normal acceleration different from the periodic signatures of Fig. 5, and it is directly affected by the predominately orbit normal solar pressure force. Fig. 6 shows the Love number solutions for each arc for no shadowing due to dust and with shadowing from dust to 40 km altitudes. In both cases, a once per rev periodic normal acceleration is also estimated. The dramatic decrease in Love number values is evident at the same grazing occultation times and also a smaller effect near November 1, 2008. This accounts for previously low Mars Odyssey Love number solutions as discussed below.

The atmospheric drag model uses density values from the MarsGRAM 2000 model (Justus et al., 1996) with minor changes as in previous results (Konopliv et al., 2006). For the global gravity solution, an overall scale factor for the drag acceleration is estimated once per arc and variations in drag over the arc absorbed with a spacecraft drag coefficient that is estimated as white noise with 100% uncertainty four times per orbit. The later is essential for removing systematic signatures in the MRO Doppler data due to higher drag forces in the lower altitude orbit. As with the solar pressure model, the drag model includes shadowing of the solar panels and HGA on the bus for the MRO and Mars Odyssey spacecraft. The MRO effect is more significant (see Mazarico et al., 2009).

The time between momentum wheel desaturations for MGS occurred about four or five times per day until September 2001, and

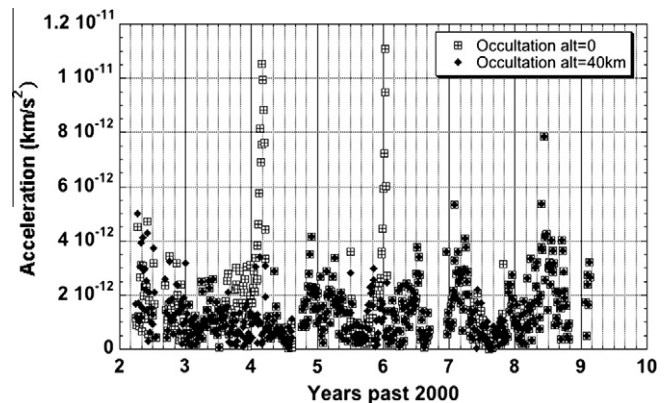


Fig. 5. The Mars Odyssey solutions of each data arc for the combined amplitude of cosine and sine orbit normal periodic (once per orbit) accelerations for two cases: (1) standard Mars shadow or “Occultation alt = 0” and (2) extending Mars shadow to 40 km altitudes to account for shadowing due to Mars dust or “Occultation alt = 40”. The a priori acceleration uncertainty is  $2 \times 10^{-12}$  km/s<sup>2</sup>. The large spikes in periodic accelerations at the grazing occultation times near the equator are removed by adding shadowing for dust.

afterwards they occurred once or twice per day. In the MGS95J model, the MGS AMDs were converted to model each thruster pulse similar to Mars Odyssey. However, an estimated impulsive burn at the midpoint of the AMD with a large a priori uncertainty (5 mm/s) was required to absorb errors in the AMD model.

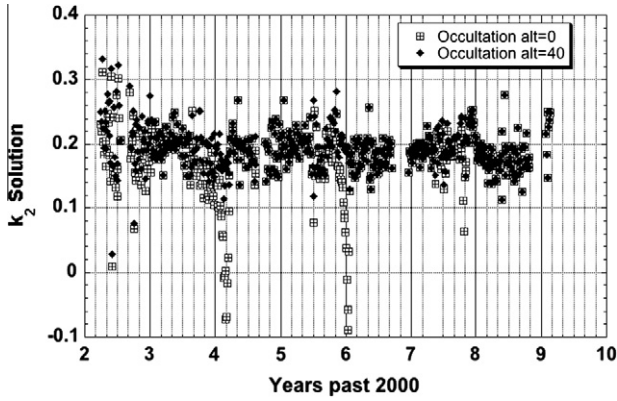


Fig. 6. The Mars Odyssey solutions for each data arc for the Mars  $k_2$  Love number for the same two cases as in Fig. 5. The periodic acceleration is also estimated together with the Love number. Thus the periodic acceleration model does not remove spurious solutions for  $k_2$ , but accounting for dust shadow does.

Since the development of MGS95J, the AMD model for MGS has been improved using adjustments for thruster number 2 and its impingement on the HGA. Fig. 7 shows the solutions for the AMD thrust direction for pulses involving thruster number 2 as a func-

tion of the elevation of the HGA and for azimuth angles less than  $100^\circ$ . These new directions and magnitudes were obtained by adding the reconstructed impulsive burn estimate to the a priori AMD thrust estimate. The AMD nominal thrust direction is along the spacecraft z-axis. For HGA elevation angles near  $-40^\circ$ , the thrust is significantly deflected from the nominal z-direction (mostly along the y-axis), and the magnitude is reduced by about 10%. Using a table lookup of thrust direction and magnitude based upon azimuth and elevation of the HGA, we can now use tighter a priori constraints on the MGS AMD impulsive burn model of 0.5 mm/s.

The Mars Odyssey AMDs occur once per day, except for a brief period during 2006 and most of 2008 when AMDs occurred every two days. Mars Odyssey reconstructed thruster magnitudes and directions also show dependence on the thruster pair used and variation over the mission, but the cause of the variation has not yet been determined. The Odyssey AMDs are uncoupled (i.e. thrust does not nominally sum to zero) and impart a delta-v to the spacecraft of about 2–4 mm/s. The a priori constraint applied to the impulsive burn correction for each AMD is 0.5 mm/s. The MRO AMDs happened every day for the first few months of the mission, and afterwards have occurred every two days. The nominal magnitude of the MRO AMDs is 1–2 mm/s, and the a priori constraint on the impulsive burn correction at the center of the AMD is 0.3 mm/s.

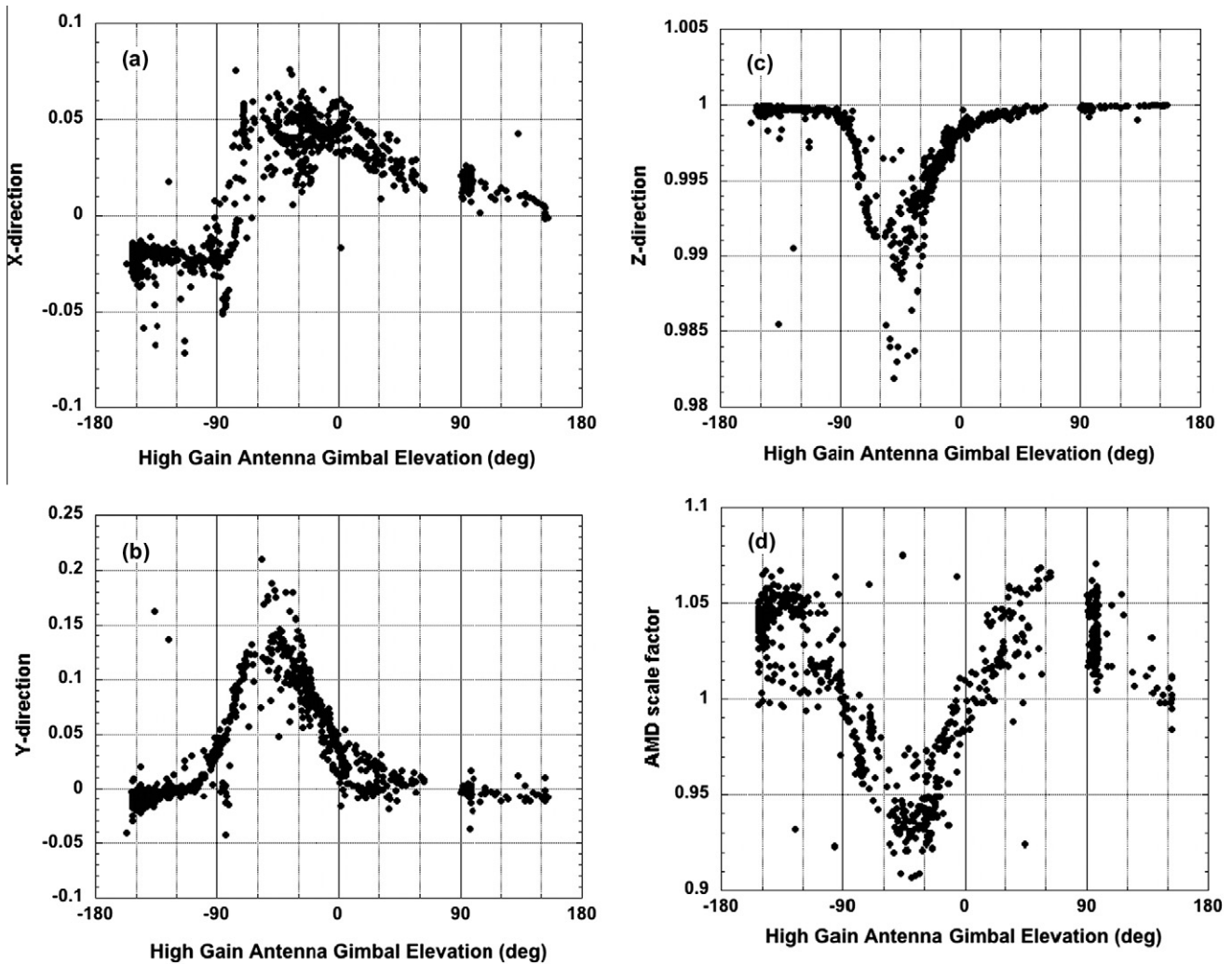


Fig. 7. The MGS thruster number 2 unit vector (a) x-direction, (b) y-direction, (c) z-direction and (d) scaling of a priori magnitude from the AMD velocity solutions, all versus the HGA elevation angle and for azimuths  $<100^\circ$ . This thruster impinges on the HGA resulting in significant thrust off the nominal z-axis direction and reduction in amplitude. Using this model, an a priori AMD model was developed that allowed us to tighten the constraint on the AMD estimate by about an order of magnitude.

#### 4. Method

The JPL Orbit Determination Program [ODP, see Moyer (1971)] was used to process the DSN tracking data (Moyer, 2000) and determine the Mars gravity field and related parameters using a square root information weighted least squares filter (Lawson and Hanson, 1995; Bierman, 1977). A parallelized version of the software processed over 18 million observations with a span of 32 years and estimated over 12,000 parameters using a 44-node linux cluster. The same ODP software, techniques and similar force and measurement models were used in previous Mars studies [for additional details see Yuan et al. (2001) and Konopliv et al. (2006)].

The tracking data of each spacecraft are divided into separate time intervals or data arcs of about 4–6 days in length and processed individually with the ODP. For each data arc, there are local parameters that are estimated only for that data arc such as spacecraft position and velocity, drag acceleration scale factor, coefficients of drag, solar pressure acceleration scale factor in three directions, periodic empirical accelerations, AMD instantaneous burn corrections, and range and 3-way Doppler (receive station is different from transmit) biases. The solution for the local parameters is iterated to convergence in a Mars centered International Celestial Reference Frame (ICRF) using the nominal gravity field and orientation. The nominal gravity field for MRO110B was MRO95A and the nominal field for MRO95A was MGS95J. Once the local parameters are converged, the local parameters are estimated with the global parameters and include the following: the static gravity field to degree and order 110, the seasonal gravity field changes in normalized  $\bar{J}_2$  and  $\bar{J}_3$ , the gravitational mass of Mars, Phobos, and Deimos, the tidal Love number  $k_2$ , the Mars orientation pole longitude, obliquity, and rates, Mars rotation rate, seasonal corrections to spin, and specular and diffuse corrections for spacecraft solar arrays. The global information arrays from all data sets are optimally merged to minimize the tracking residuals (Yuan, 1991).

The gravity field is represented as a spherical harmonic expansion with normalized coefficients ( $\bar{C}_{nm}$ ,  $\bar{S}_{nm}$ ), and is given by (e.g., Heiskanen and Moritz, 1967; Kaula, 1966)

$$U = \frac{GM}{r} + \frac{GM}{r} \sum_{n=2}^{\infty} \left( \frac{R_e}{r} \right)^n \bar{P}_{nm}(\sin \phi_{lat}) \left[ \bar{C}_{nm} \cos(m\lambda) + \bar{S}_{nm} \sin(m\lambda) \right],$$

where  $GM$  is the gravitational constant times the mass of Mars,  $n$  is the degree,  $m$  is the order,  $\bar{P}_{nm}$  are the fully normalized associated Legendre polynomials,  $R_e$  is the reference radius of Mars (3396.0 km for MRO110B, MRO110B2 and MRO95A),  $\phi_{lat}$  is the latitude, and  $\lambda$  is the longitude (east positive). The gravity coefficients are normalized and are related to the unnormalized coefficients as (Kaula, 1966)

$$\begin{pmatrix} C_{nm} \\ S_{nm} \end{pmatrix} = \left[ \frac{(n-m)!(2n+1)(2-\delta_{0m})}{(n+m)!} \right]^{1/2} \begin{pmatrix} \bar{C}_{nm} \\ \bar{S}_{nm} \end{pmatrix} = f_{nm} \begin{pmatrix} \bar{C}_{nm} \\ \bar{S}_{nm} \end{pmatrix}.$$

The corresponding normalized Legendre polynomials  $\bar{P}_{nm}$  are thus related to the unnormalized polynomials  $P_{nm}$  by  $P_{nm} = \bar{P}_{nm}/f_{nm}$ .

The gravitational potential also includes modifications due to tides caused by a perturbing body (i.e., the Sun for Mars). The tidal potential acting on a spacecraft with position  $\vec{r}$  (magnitude  $r$  and unit vector  $\hat{r}$ ) from the central body and perturbing body at position  $\vec{r}_p$  (magnitude  $r_p$  and unit vector  $\hat{r}_p$ ) relative to the central body is given by

$$U = k_2 \frac{GM_p}{R} \frac{R^6}{r^3 r_p^3} \left[ \frac{3}{2} (\hat{r} \cdot \hat{r}_p)^2 - \frac{1}{2} \right],$$

where  $M_p$  is the mass of the perturbing body causing the tide, and  $R$  is equatorial radius of the central body. With a tide lag angle introduced, the tide causes the second degree and second order coefficients to have time varying components as follows for normalized values (e.g., Eanes et al., 1983)

$$\Delta \bar{C}_{22} = k_{22} \sqrt{\frac{3}{20}} \frac{GM_p R^3}{GM r_p^3} \cos^2 \phi_p \cos[2\lambda_p + \delta_2],$$

$$\Delta \bar{S}_{22} = k_{22} \sqrt{\frac{3}{20}} \frac{GM_p R^3}{GM r_p^3} \cos^2 \phi_p \sin[2\lambda_p + \delta_2],$$

where  $\phi_p$  and  $\lambda_p$  are the latitude and longitude of the perturbing body on the surface of the central body. These coefficient expressions consist of a constant plus periodic part. The constant or permanent part of the tide is not included in the corresponding published values of the gravity coefficients for the JPL Mars gravity fields such as MRO110B. The tide is best determined by the secular inclination effect on  $k_{22}$  (Yoder et al., 2003), with a factor of 10 and 100 less sensitivity for  $k_{21}$  and  $k_{20}$ , respectively.

The estimated tide solution includes the effects from the solid-body tide and atmospheric tide. The  $k_{22}$  Love number is represented as a real and imaginary part as given by  $\text{Re}(k_{22}) = k_{22} \cos \delta_2 + k_a \cos(41^\circ)$  and  $\text{Im}(k_{22}) = -k_{22} \sin \delta_2 + k_a \sin(41^\circ)$ , where  $\text{Im}(k_{22})$  is negative for solid tidal lag ( $\delta_2 = 0.6^\circ$ , Jacobson, 2010) and positive for the atmospheric tide but is dominated by the atmospheric tide ( $\text{Im}(k_{22}) \approx 0.01$ , see Konopliv et al., 2006). The S2 component of the atmospheric tide has maximum surface pressure near 10:30 in the morning, and is accounted for here by the phase of  $41^\circ$ .

The JPL ephemeris DE421 (Folkner et al., 2009) was used for planetary positions required for third-body perturbations and Doppler and range processing. This ephemeris contains several meter-level Earth–Mars ranging from MRO, MGS, Mars Odyssey, and Mars Express through the end of 2007. In addition, Mars VLBI data ( $\sim 200$  m) in support of the Mars Science Laboratory (MSL) mission is included (Folker et al., 2008). JPL satellite ephemeris MAR063 was used for the Phobos and Deimos positions (Jacobson, 2007; Jacobson and Rush, 2006), and it shows significant improvement versus the previous MAR033 ephemeris used for MGS95J. The Mars system  $GM$  (Mars plus Phobos and Deimos) for MRO110B is  $42828.37453 \pm 0.00053 \text{ km}^3/\text{s}^2$  ( $10\times$  formal uncertainty). The Phobos and Deimos mass estimates are  $7.17 \times 10^{-4}$  and  $9.43 \times 10^{-5} \text{ km}^3/\text{s}^2$ , respectively. In future models, we will use the improved mass estimates and satellite orbits MAR085 from Jacobson (2010), which uses a much broader data set including tracking from the Phobos 2 Soviet mission and Viking, Earth based astrometry, MGS MOLA derived satellite positions, MRO images, and Mars Express images.

Using the MRO110B gravity field, the MRO local parameter orbit solutions were regenerated and archived with the NAIF PDS node. The orbit overlap errors associated with these orbits are displayed in Fig. 8. Although these errors represent the relative orbit error, the range of values gives an indication of the absolute orbit error. The typical total orbit overlap error is about 1 m with radial accuracies below 10-cm. These orbit errors are comparable to those of MGS or Odyssey (Konopliv et al., 2006; 15-cm, 1.5-m, 1.6-m average radial, along the velocity vector, and orbit normal overlap errors using MGS95J). The improved MGS spacecraft models and MRO110B gravity model reduce MGS average overlap errors to 12-cm, 0.9-m, and 0.9 m. Since the DSN Doppler measures the line-of-sight velocity direction from Earth to Mars, the dependency of the MRO orbit error on orbit geometry as viewed from Earth is

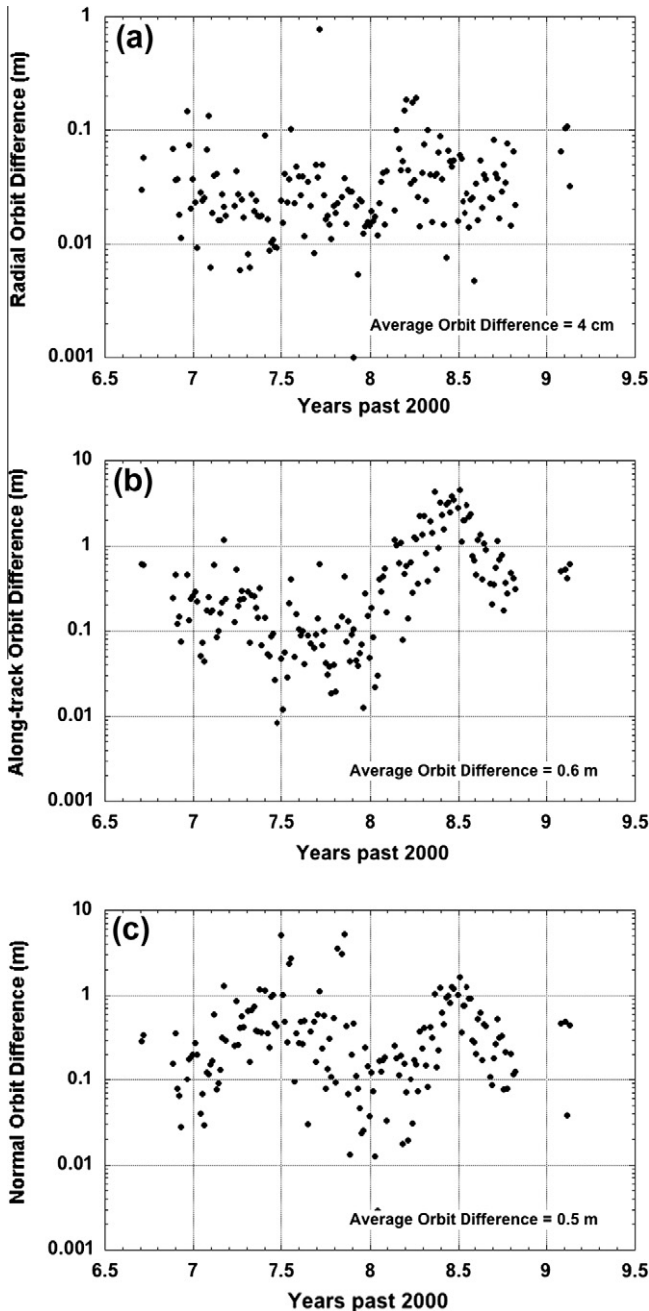


Fig. 8. MRO orbit overlap accuracy for the (a) radial, (b) along-track, and (c) normal to the orbit plane directions. The orbit overlap error is the RMS difference for a one orbit overlap (2 h) for each data arc (typically 4 days in length).

evident in Fig. 8 in the along-track (along spacecraft velocity) for more face-on geometry as viewed from Earth (~year 8.0–8.5). This along-track orbit error increases to 3–5 m at year 8.5 and may have additional causes other than geometry. The orbit normal also shows small spike increases near orbit edge-on geometries at year 7.5 and 7.8 (Earth POS inclination is 90° at these times in Fig. 3b).

5. Static gravity solution

After processing all the tracking data for the MRO110B gravity field, a constraint is applied to the higher degree harmonics to adjust the power spectrum so it approximately follows a power law ( $\bar{C}_{nm}, \bar{S}_{nm} \propto 1/n^2$ , Kaula, 1966). The constraint is similar to that used

for MGS95J but begins at a higher degree of 70 for MRO110B. However, we feel MRO110B may be over constrained with suppressed admittance in some cases (e.g. Fig. 14b). So, an alternate solution MRO110B2 is available and it is identical to MRO110B except uses a constraint beginning at degree 80 and about 35% looser. The RMS magnitude spectrum of MRO110B, MRO110B2 and MRO95A and the associated unconstrained solution and corresponding uncertainties are shown in Fig. 9. The MRO solutions are compared to MGS95J (Konopliv et al., 2006) and to two power laws, a Kaula rule ( $8.5 \times 10^{-5}/n^2$ ) and uncompensated topography ( $7.8 \times 10^{-4}/n^{2.5}$ ; Smith et al., 2001b). A fit to the MRO110B and MRO110B2 coefficients of the well determined higher end of the spectrum ( $n = 50-80$ ) gives  $7.28 \times 10^{-4}/n^{2.50}$  and  $5.00 \times 10^{-4}/n^{2.40}$ , respectively, and is a closer match to uncompensated topography. The MRO gravity solutions are similar and mostly improve the higher degree terms of the Mars gravity field versus the previous solutions. The resolution with the MRO data has improved from about degree 70 with the MGS95J solution to degree 90 with the MRO110B solution. Since all the Mars orbiters are polar, the near sectoral coefficients are better determined. With the higher order coefficients ( $n-m < 10$ ), the gravity field resolution is degree 110 (the crossing of the Kaula power law and coefficient uncertainty), but aliasing of the coefficients is evident for the last five degrees. The differences between the MGS95J and MRO110B gravity coefficients show that the uncertainties are approximately correct except for the lowest degree harmonics. The higher differences at this level are attributable to long term spacecraft force model errors such as solar pressure (and dust effects) and atmospheric drag. Although the coefficients are well determined to degree 70 for MGS95J or 90 for MRO110B, high correlations (0.4–0.6) occur between coefficients with the same order and degrees  $n$  and  $n + 2$

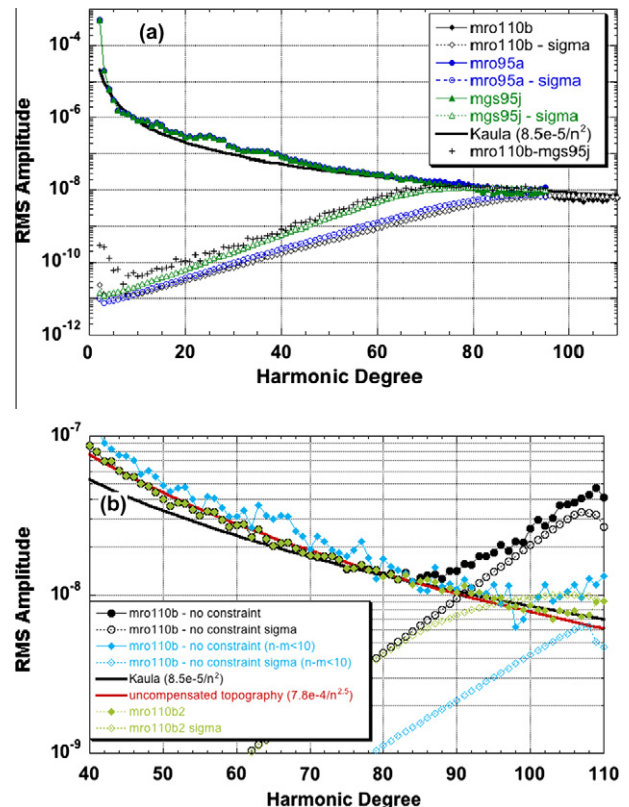


Fig. 9. Gravity RMS magnitude spectrum of the (a) MRO110B, MRO95A and MGS95J fields and (b) the higher degree spectrum of the unconstrained MRO110B solution, and looser constrained MRO110B2. The gravity spectrum closely matched the spectrum of gravity from uncompensated topography (Smith et al., 2001b).

(i.e., even or odd degrees), as shown by the Kaula linearized solution (Kaula, 1966). All other correlations between coefficients are  $\sim < 0.1$ . The peak correlations reduce by 10–20% for the MRO110B solution versus MGS95J, showing that the MRO orbit helps some with separability of the coefficients.

Although the global resolution of MRO110B in Fig. 9 is degree 90 or 120 km at the surface, the local resolution can vary due to the tracking quality, amount of data and altitude variations of the spacecraft. The local resolution is determined by the intersection of the expected gravity acceleration magnitude (or signal) and localized gravity acceleration error (or noise) as plotted versus harmonic degree (Konopliv et al., 1999). Using the  $8.5 \times 10^{-5}/n^2$  power law of Fig. 9, the corresponding acceleration at the surface versus harmonic degree is  $44.6/n^{1/2}$  mGals. The unconstrained covariance of MRO110B is then used to map the contribution of each harmonic degree to the acceleration uncertainty at the surface. Fig. 10 shows the surface resolution (or degree strength of Konopliv et al., 1999) as a function of surface location. The minimum resolution is degree 86 for the northern mid-latitude region. The polar regions are slightly better determined due to the higher density of data, and the near degree 110 resolution at the south pole is due to the lower spacecraft altitude (see Fig. 1) dictated by the global topographic shape (cf. Smith et al., 1999c). However, part of the increase of the polar resolution may be improperly inflated due to over sampling. The formal covariance surface acceleration uncertainty for all degrees up to the corresponding local degree strength is a uniform  $10 \pm 1$  mGals except for within  $10^\circ$  of the south pole where it drops to 6 mGals.

Since most of the higher frequency gravity is driven by the topography, high correlations of about 0.8–0.9 exist between the corresponding harmonic coefficients for degrees greater than about 30, when the gravity is well determined. This allows for an evaluation of the improvement and resolution of the gravity models and the assumptions in modeling such as the a priori coefficient constraint. The correlation of gravity with topography (Smith et al., 2001b) has shown substantial increases with the MRO gravity models (Fig. 11). The largest improvement comes from the first year of MRO data (MRO95A) due to the initial inclusion into the gravity model of this low altitude tracking, but there is also significant improvement with the second year of MRO data (MRO110B) with correlations  $> 0.6$  to degree 90. As shown with the gravity error spectrum (Fig. 9b), the near sectoral coefficients are much better determined and show correlations  $> 0.6$  to the solution degree 110. The increasingly high correlation of gravity with topography with improved spatial resolution is indicative of the support of short wavelength loads by lithospheric strength.

The superiority of the near sectoral versus near zonal coefficients is also reflected in the signal-to noise ratio (here defined as  $SNR_{nm} = \sqrt{(C_{nm}/\sigma_{C_{nm}})^2 + (S_{nm}/\sigma_{S_{nm}})^2}$ ) as shown in Fig. 12. We

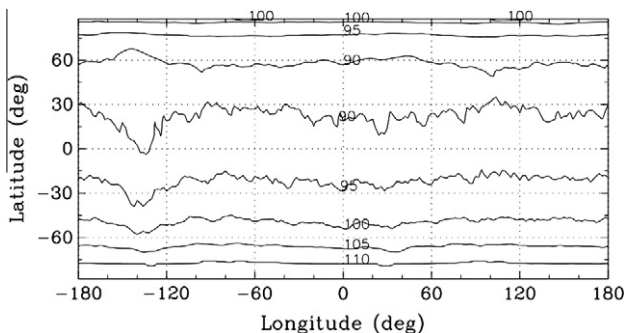


Fig. 10. The surface resolution or degree strength of the MRO110B gravity field in harmonic degree for each location of the Mars surface.

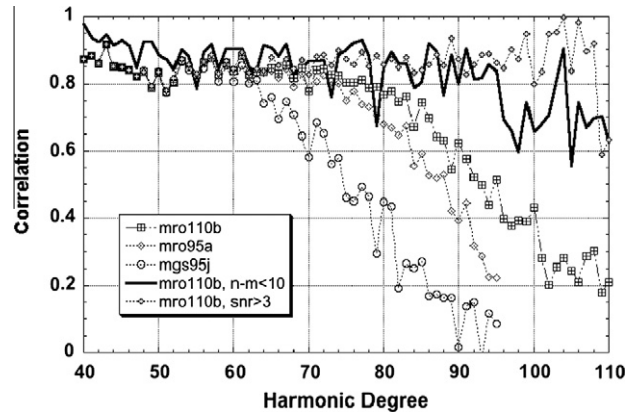


Fig. 11. The correlation of the gravity coefficients with spherical harmonic topography for the recent MRO gravity fields and the previous MGS95J solution. Correlation for two subsets, where  $n-m < 10$  or coefficient value/ $\sigma > 3$ , of the MRO110B gravity field are shown as well.

see that there are significant numbers of  $SNR_{nm}$  coefficients (with values greater than 2.50) for  $m$  near  $n$  all the way to  $n = 110$ . The correlation for the collection of higher SNR coefficients is shown in Fig. 11, and could be used in admittance analysis as well as an alternative to  $n-m < 10$ . The cause of this sectoral bias is not spacecraft geometry or near resonance, or that the sectorals are larger than the zonals (rather it is that  $\sigma_{n0} \approx 10\sigma_{nm}$ ), but the method by which the spacecraft orbit is affected by gravity. The purely zonal coefficient is detected from terms in the expansion of the gravity field with frequency  $(n - 2p + q)\dot{M}$ , where  $q$  and  $p$  are integers and  $\dot{M}$  is the spacecraft orbit mean motion (Kaula, 1966), and the gravity coefficient is proportional to  $e^{|q|}$ . There is one term that is secular that is shared by all degree  $n$ . However, if we were to truncate the field at  $n = N$ , then the  $N$  component is uniquely determined by the perturbation with frequency  $N\dot{M}$ , and so on down the line. The size of the perturbation is dependent on the inverse frequency. Most of the Doppler signal is sensitive to this amplitude of the periodic change, except for an along-track component.

The purely sectoral components with  $m = n$  are perturbed by coefficients with frequency  $(n - 2p + q)\dot{M} - n\omega$ . We can choose  $p$  and  $q$  such that the remaining term is dependent on planetary rotation  $\omega$ . The  $n = N$  coefficient is then uniquely determined by the term with frequency  $N\omega$ . Again, the amplitude of this term again depends on the inverse frequency. Since  $\omega/\dot{M} \approx 12.6$ , we should expect, all other factors being equal, that the sectorals are

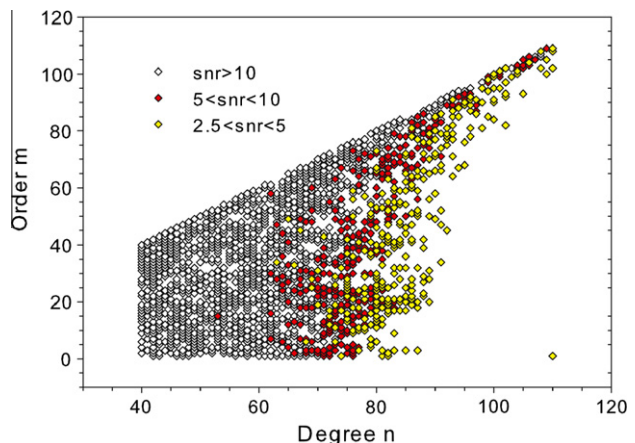


Fig. 12. The ratio (or SNR) of the combined coefficient magnitude to uncertainty for each degree and order. The SNR of the near sectoral coefficients is mostly higher.



more accurately determined than the zonal coefficients by roughly a factor of 10. These larger amplitudes for the near sectoral terms are apparent in mapping the gravity orbit perturbations from Kaula (1966) into the radial component.

The latest gravity field (Fig. 13) lacks “striping” correlated with spacecraft groundtracks, which underscores the global, high-resolution coverage. It is notable that the current model well resolves not only major structures such as volcanoes (McGovern et al., 2002, 2004) and the Valles Marineris (cf. Anderson and Grimm, 1998), but also adjacent anomalies indicative of flexural effects such as volcanic moats and rift flank uplift. The improved resolution now enables gravitational exploration of loading histories of isolated tectonic provinces, as has been accomplished with Arabia

Terra (Evans et al., 2010). In addition, it greatly improves the ability to identify possible impact basins buried beneath the northern plains (cf. Frey et al., 1999, Frey, 2006).

To explore how the reduction in uncertainties of the global spectrum, seen in Figs. 9b and 11, translates to specific features on the surface of Mars through the use of only the near sectoral terms, we employed the spatio-spectral localization method of Simons et al. (1997) with the  $(n-m) < 10$  coefficients. This method utilizes a spherical harmonics transform to convolve the windowed spatial data into the spectral domain while obeying the sampling theorem, and it allows for the spectral analysis of a discrete region on a sphere. As such, we calculate the transfer function (admittance) and correlation between the localized gravity and

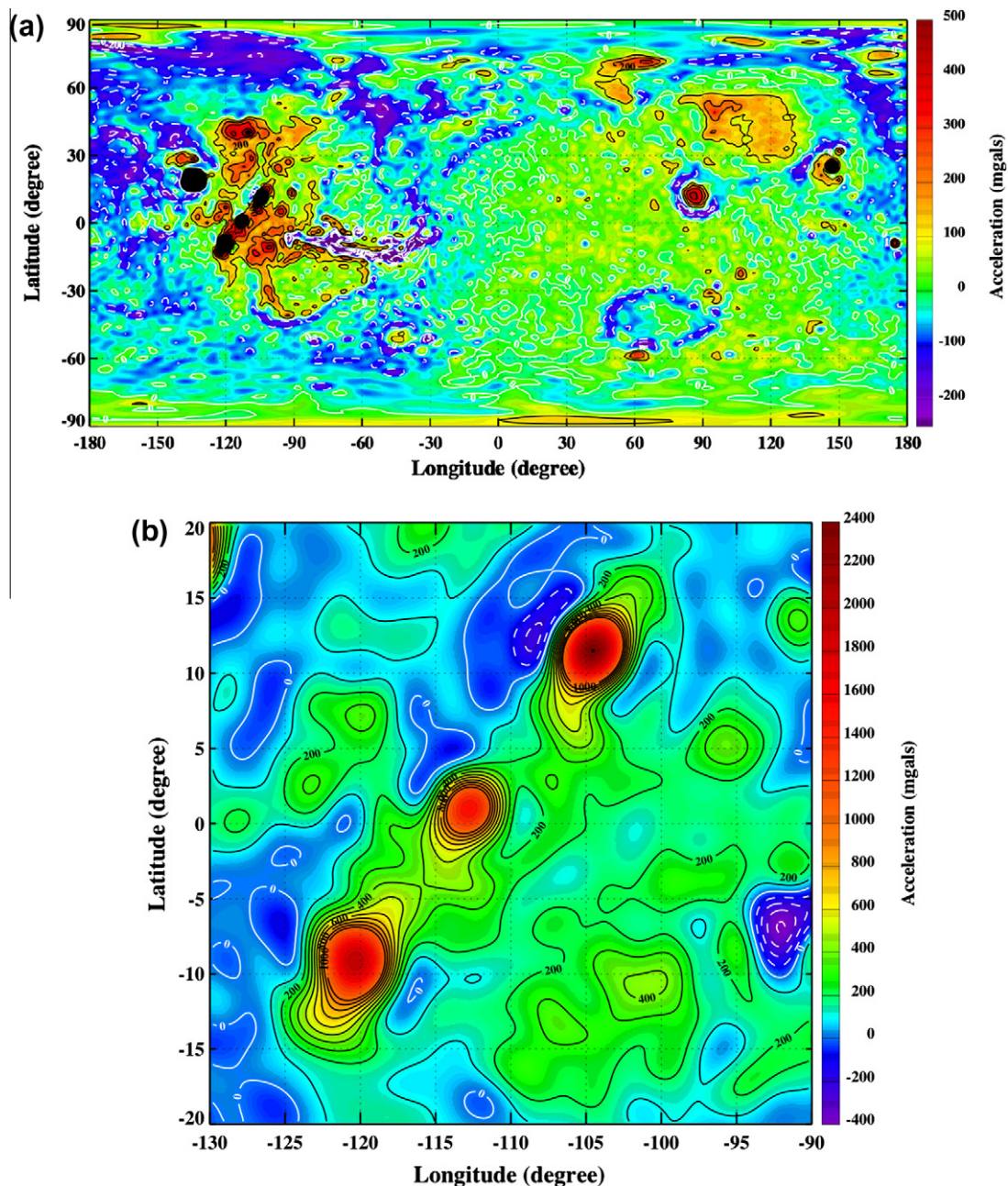


**Fig. 13.** Surface gravity anomalies complete to degree and order 90 with respect to the reference ellipsoid ( $f = 1/196.9$ ,  $R_e = 3397$  km) for (a) all of Mars with MRO110B and (b) the Tharsis volcanoes Arsia, Pavonis, and Ascraeus Mons (left to right) with MRO110B2. The dynamic range of the Mars gravity extends from the maximum of 3068 mGals over Olympus Mons to a minimum of  $-658$  mGals in Valles Marineris; an increase of 256 mGals versus the dynamic range given by the 70th degree MGS95J model. The peaks values for Arsia, Pavonis, and Ascraeus Mons for MRO110B2 ( $n = 90$ ) are 1968, 1529, and 2389 mGals, respectively, an increase of 176, 264, and 443 mGals over MGS95J ( $n = 70$ ). For MRO110B, the volcano amplitudes are suppressed by 10–30 mGals versus MRO110B2.

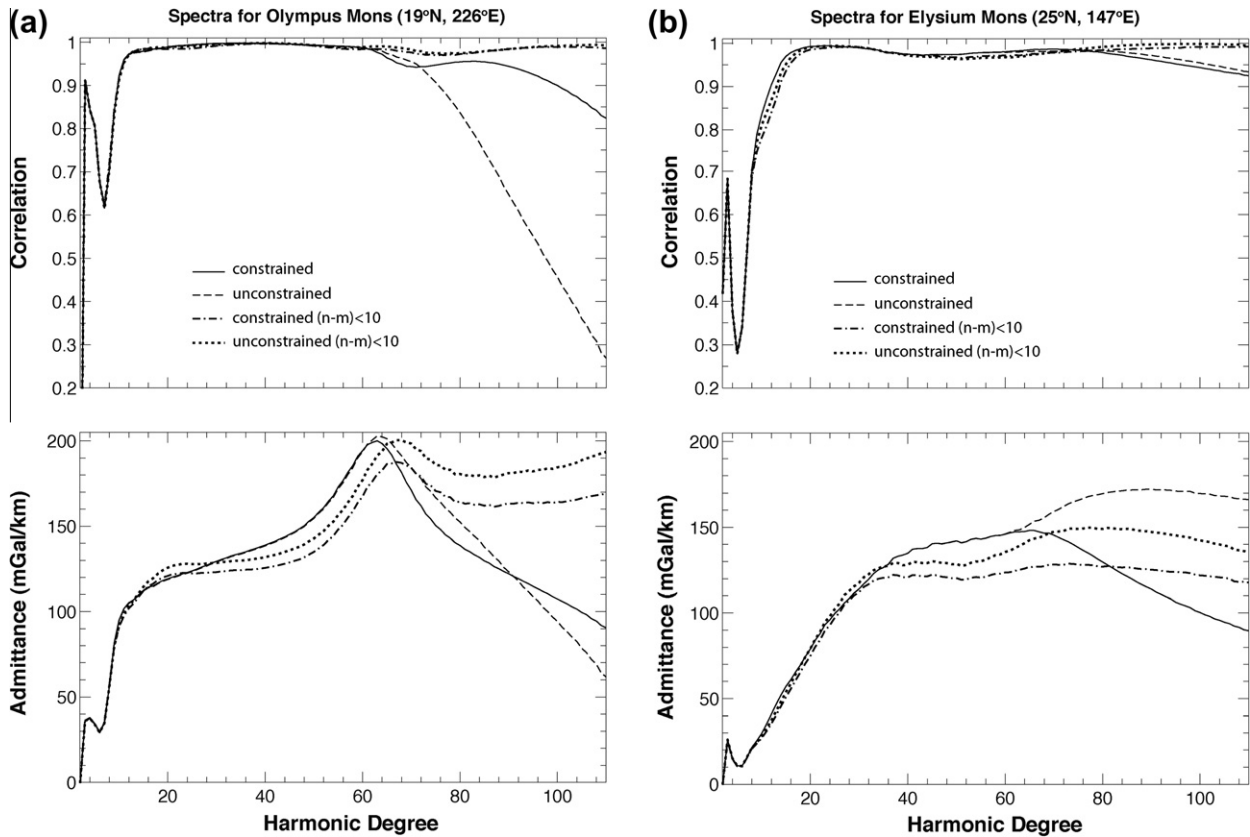


**Fig. 14.** Correlation and admittance (transfer function) spectra between gravity and topography for (a) Olympus Mons ( $19^{\circ}\text{N}$ ,  $226^{\circ}\text{E}$ ) and (b) Elysium Mons ( $25^{\circ}\text{N}$ ,  $147^{\circ}\text{E}$ ), using both the Kaula power-law constrained and unconstrained coefficients and  $J_2$  terms removed. Also shown are the spectra obtained with only the 10 nearest sectoral coefficients for both constrained and unconstrained cases. The spectra are obtained via the localization approach of Simons et al. (1997).

topography. These quantities are commonly used to discern the type of mechanical loading to which a planetary lithosphere is submitted and to imply the interior structure of a planet (e.g., Dorman and Lewis, 1970; Forsyth, 1985; Smrekar, 1994).

Fig. 14a shows the admittance spectrum obtained for Olympus Mons ( $19^{\circ}\text{N}$ ,  $226^{\circ}\text{E}$ ) for different sets of coefficients. In the case of the constrained coefficients (i.e., MRO110B, which has a Kaula power law constraint  $\propto 1/n^2$  beginning at degree 70), admittance values are below 150 mGal/km except for a peak around harmonic degree 65. These admittance spectral amplitude and shape are very similar to those found by McGovern et al. (2002, 2004) and especially Belleguic et al. (2005), but now extend to degree and order of 87 (the local degree strength value,  $\sim 122$  km) from less than 60 previously. Likewise, the correlation spectrum for the constrained coefficients matches those of found in McGovern et al. (2002, 2004) and Belleguic et al. (2005). The spectral dip that occurs beyond degree 60 in both admittance and correlation extends to degree 110 and cannot be matched by any simple flexural model (e.g., Nunes et al., 2009). This dip cannot either be explained by a loss in signal power due to constraining the coefficients to the Kaula power-law rule, as the admittance and correlation spectra obtained from the unconstrained gravity coefficients (no power law applied) are still depressed over the high harmonics. We note that the Nyquist degree imposed by the localization window (Simons et al., 1997) is  $\sim 60$  for this location as well as Elysium Mons (Fig. 14b), and that care must be taken when interpreting spectral features between the Nyquist degree and the degree strength of the field. Hence, it is questionable whether or not these spectral dips at high harmonic degrees reflect the nature of the volcanoes, and not surprising that they cannot be matched by simple flexural models. With that said, the spectral dips seen in both admittance

and coherence are not seen in some other volcanic locations and that for the common bandwidths the solutions from Belleguic et al. (2005) and McGovern et al. (2004), are similar to ours despite different input data and windowing technique. Considering only the ten nearest sectoral coefficients ( $n-m < 10$ ) for both the constrained gravity field and the spherical harmonic expansion of the topography significantly alters the Olympus spectra at the high harmonics by eliminating the spectral dips. Notably, correlation values are pushed close to one for all degrees beyond 12, which is expected for support of surface topography by a strong elastic lithosphere and matches the behavior seen similarly in the global spectral correlation with ( $n-m < 10$ ). For the sake of completeness, we also examined the ( $n-m < 10$ ) terms of the unconstrained coefficients. This produced only small variations in spectral amplitude and minimal alteration of the spectral behavior in admittance and correlation from the constrain ( $n-m < 10$ ) case.

Fig. 14b shows the admittance and correlation spectra from the same coefficient sets for Elysium Mons ( $25^{\circ}\text{N}$ ,  $147^{\circ}\text{E}$ ). Although smaller in magnitude with respect to Olympus, the Elysium spectra produced from the constrained coefficients possess a dip in the high harmonics. Such dips again wither from the spectra when only the near sectoral ( $n-m < 10$ ) coefficients are considered, and correlations values beyond degree 12 are pushed close to one.

Our analyses show that the near sectoral terms contain much of the signal in the high harmonics not only in the global sense (Figs. 9 and 11), but also at distinct features on the surface (such as Olympus and Elysium Montes); the substantial improvement in signal-to-noise ratio deriving, at least in part, from the near-polar orbit of the spacecraft. We therefore believe that spectral shapes produced by ( $n-m < 10$ ), with correlations  $\sim 1$  and without the spectral dips at the high harmonic degrees, might be a better measure of

the nature of these volcanoes. The  $(n-m) < 10$  data could also be valuable with other windowing schemes with higher Nyquist degrees and at other locations, perhaps even when examining small features without the aid of spectral admittance. However, the use of the near sectoral terms for regional analysis is limited to a band around the equator and for analysis of features in the east–west direction. It is less effective for Valles Marineris (only partly visible in Fig. 15a and b) because it is stretched in the east–west direction and for high latitude features such as craters. The cause for the drop in effectiveness is that the near sectoral terms lose power quickly at high latitudes (see Fig. 15c). The  $(n-m) < 10$  terms are most effective for latitudes  $|\phi| < 40^\circ$ . For a slightly larger range of sectoral terms  $(n-m) < 20$  for which the coefficients are still better determined (e.g. Fig. 2 in Yuan et al. (2001)), the latitude range is  $|\phi| < 50^\circ$ .

Finally, the effect of incorporating unconstrained gravity coefficients, which contain greater power beyond degree 70 over the constrained coefficients, is harder to predict. The field becomes much rougher in these scales, and the net effect of summing the contributions from the different degrees is likely deterministic – they may add constructively or destructively and lead to either an increase or decrease in admittance values at different locations, as it is seen in Fig. 14.

## 6. Seasonal zonal gravity

The largest signature in the seasonal mass exchange between the Mars polar caps is given by variations in the zonal coefficients (e.g., Sanchez et al., 2006), with the odd degree zonal amplitudes  $\sim 20\%$  larger than the even degree. For gravity studies, the odd degree amplitudes begin at degree 3, since first order variations in  $\bar{J}_1$  are undetectable with Doppler tracking only and the origin being at the center-of-mass. The largest seasonal signature best observed in the Mars gravity field is the variation in the odd zonal, normalized gravity coefficient  $\bar{J}_3$  that is primarily proportional to  $\sin M$  ( $M$  is Mars orbit mean anomaly), and is the focus of this study. The observed  $\bar{J}_2$  signature is about an order of magnitude less accurate than  $\bar{J}_3$  since it has much smaller contributions to the secular argument of pericenter rates (see Konopliv et al., 2006). The major contribution to  $\bar{J}_2$  comes from changes to the nodal longitude of the spacecraft orbit, which in turn is sensitive to spacecraft geometry. Also, there are challenges in coefficient separability (cf. Smith et al., 2009; see SOM of Yoder et al. (2003)). Thus, the observed  $\bar{J}_3$  gravity from the MGS spacecraft represents a collection of odd zonal coefficients from the secular changes in eccentricity  $e$  and argument of pericenter  $\omega$ . The zonal factors are functions of spacecraft orbit inclination  $i$ , semi-major axis  $a$  and eccentricity (Yoder et al., 2003). For MGS,  $a = 3775.6$  km and  $i = 92.93^\circ$ , we get  $\bar{J}_3 + 1.238\bar{J}_5 + 1.235\bar{J}_7 + 1.126\bar{J}_9 + \dots$ . The equivalent sum for Odyssey is  $\bar{J}_3 + 1.221\bar{J}_5 + 1.199\bar{J}_7 + 1.074\bar{J}_9 + \dots$  (evaluated using  $a = 3794.5$  km and  $i = 93.14^\circ$ ) and is about 1% smaller than the MGS sum. Note there are other second order effects ( $< 1\%$ ) in the odd zonal sum such as mantle center-of-figure offset from center-of-mass caused by loading from the ice cap variations ( $\propto \bar{J}_2 \delta \bar{J}_{1ice}$ ). Variations in other coefficients, in particular  $\bar{C}_{21}$  and  $\bar{S}_{21}$ , are detectable (Konopliv et al., 2006), but are left for future study.

There are still questions concerning the total mass involved in this exchange of mass from one pole to the opposite, whether this process is highly regular or contains evidence of more irregular climate changes (Malin et al., 2001). Constraints on the martian ice-cap seasonal histories are provided by visual imaging (e.g. Piqueux and Christensen, 2008), thermal imaging (TES, Kieffer et al., 2000; Kieffer and Titus, 2001), the high energy neutron detection (HEND, Litvak et al., 2004, 2006) and Neutron Spectrometer (NS, Prettyman et al., 2004, 2009) instruments aboard the Odyssey spacecraft, and

2 years of laser altimetry ranging (MOLA) (Smith et al., 2001b; Aharonson et al., 2004) and tracking data from orbiting spacecraft. Our analysis investigates inter-annual changes and compares seasonal gravity changes to that observed by the GCM AMES (Haberle et al., 1999, 2008) and Laboratoire de Météorologie Dynamique (LMD, Forget et al., 1999) models and Odyssey HEND and NS data sets.

The observed MGS and Odyssey  $\bar{J}_3$  seasonal gravity solutions (see Fig. 16) are determined using the same method of Konopliv et al. (2006), but with the seasonal solution showing much less scatter (in part due to improved AMD constraints). The  $\bar{J}_3$  solution for each data arc is determined by estimating the local parameters (e.g., spacecraft orbit, drag, AMDs) together with seasonal  $\bar{J}_2$  and  $\bar{J}_3$  corrections, while holding fixed the MRO110B static gravity field. The best estimate for Mars seasonal  $\bar{J}_3$  comes from MGS tracking obtained after September 2001 when AMD frequency was reduced from about 4 a day to one a day. The corresponding drop in the RMS standard error from a fit to a periodic series drops by a factor of 2 or more. Still, there appears to be a significant long-term variation from year to year that may be spacecraft dependent and not necessarily imply a real inter-annual change in ice cap mass (see Fig. 17). This periodic signature is best seen by comparing aphelion to aphelion martian years ( $-180^\circ \leq M \leq 180^\circ$ ) or cycles, since it happens that each cycle agrees best near aphelion. The usual choice is to display seasonal data in terms of Mars aerocentric true solar longitude,  $L_s$  ( $L_s = 251.01^\circ + \dot{\alpha}\Delta t_{J2000}$  at  $M = 0^\circ$ ). This solar true longitude  $L_s = 0^\circ$  at northern spring equinox, and  $\dot{\alpha}\Delta t_{J2000}$  is a very small correction related to precession; Allison, 1997).

The difference between cycle 1 (February 4, 1999–October 31, 2000) and 3 (September 21, 2002–August 3, 2004) is essentially flat with no discernable signature. However, the differenced cycle 4–cycle 3 shows a distinct long-term bow that has been fit to the function  $a(1 + \cos M)$  with  $a = 2.8 \times 10^{-10}$  or about 10% of the overall seasonal signature. A fit to the function  $1 + \cos f$ , where  $f$  is the true anomaly, results in a slightly better fit, but not enough to justify using this function. The differenced cycle 2–cycle 3 displays a similar bow but with the opposite sign, suggesting a quadrennial signature. If we restrict the fit to just the higher accuracy data ( $M > 10^\circ$ ), we find the solution for cycle 2 is:  $a = -2.9 \times 10^{-10}$ .

After we apply a balanced correction to cycle 2 ( $a = -2.8 \times 10^{-10}$ ) and cycle 4 ( $a = +2.8 \times 10^{-10}$ ), the residuals are then fit to a periodic series in  $\sin jM$  and  $\cos jM$  (see Table 2), where we obtain a significant solution for periodic components out to  $j = 6$ . Fig. 18 shows the post-fit seasonal changes versus an aphelion year. The standard mean deviation is  $2.3 \times 10^{-10}$ , or about as good as the best formal uncertainty attached to an individual arc. The 6-frequency solution changes by less than two standard deviations if cycle 1 data are added to the solution. However, it happens that this signature is almost captured by a fit to just the first 3 harmonics to cycle 3.

The next step is to examine the residuals to each cycle to see if we can detect an inter-annual signature (e.g., Matsuo and Heki, 2009). Fig. 19 shows the MGS seasonal short arc solutions together with the global 6-frequency fit of Table 2. The most obvious signature is that the short cycle 5 (June 27, 2006 to end of mission) seems to be high relative to the others by about  $2 \times 10^{-10}$ . Otherwise the long wavelength deviations seem to be of order  $\pm 1 \times 10^{-10}$ . The remaining data from cycle 1 and cycle 2 ( $-180^\circ \leq M \leq -10^\circ$ ) are not shown, but are much noisier due to more AMDs. Cycle 1 has a slightly smaller peak during southern winter. However, the cycle 2 southern winter peak is by far the largest feature suggesting that amplitude is  $\sim 5 \times 10^{-10}$  above the norm (see Fig. 16). The magnitude is accentuated by the correction we made to the data, but remains even if it is not applied. Without corroborating evidence (Odyssey neutron spectrometers did not cover this event), we tend to discount this feature as due to errors introduced by the multiple AMD events prior to September 2001 or other

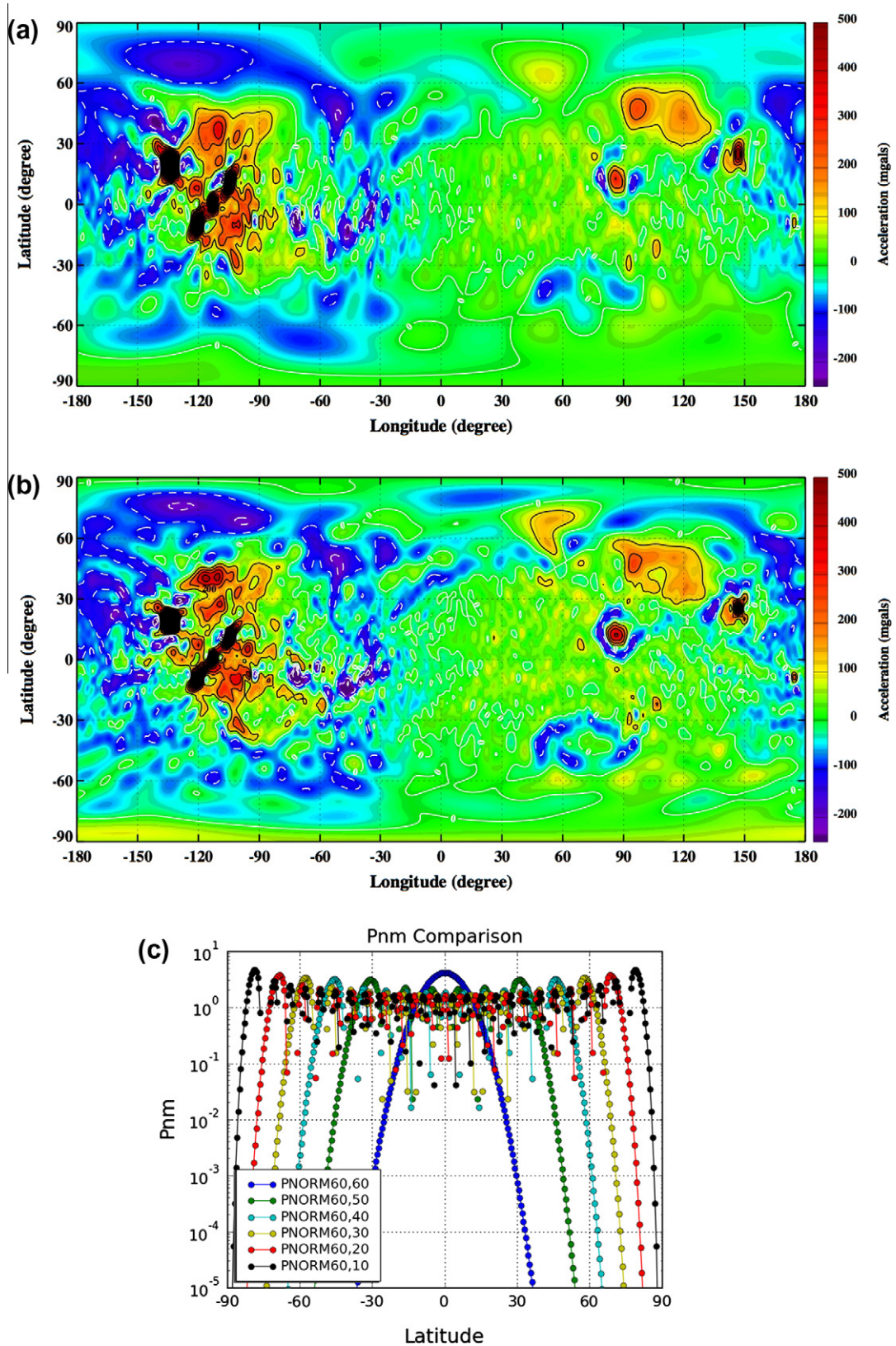
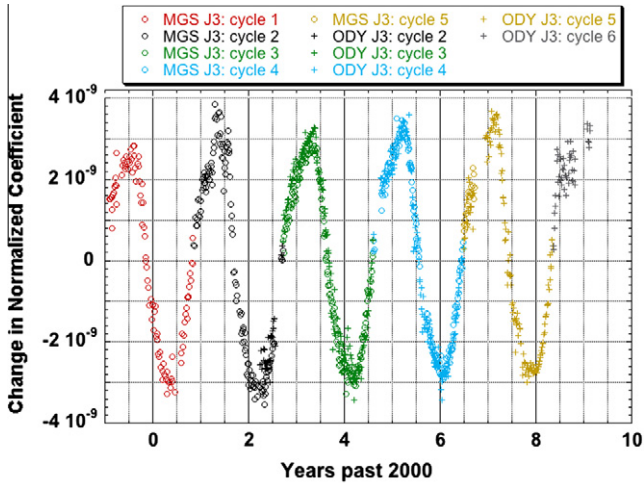


Fig. 15. These figures demonstrate the coverage of the near sectoral terms with the global gravity anomaly map for (a)  $n-m < 10$  and (b)  $n-m < 20$ , and (c) amplitudes of the normalized associated Legendre polynomials along the prime meridian for degree 60 and increments of 10 for the order. In (c) the sectoral terms (PNORM60, 60 – blue) only provide near equatorial information whereas the near zonals (PNORM60, 10 – black) contain information for all latitudes.

unidentified forces acting on the spacecraft. A further tightening of the a priori AMD velocity correction noticeably reduces this cycle 2 peak above the norm. Systematic changes in the ‘good’ data repre-

sented by Fig. 18 are well bounded by  $\pm 2 \times 10^{-10}$  or about 3% of the total change. So it appears that there is no clear inter-annual signature in the MGS data aside from the  $\cos M$  bow.



**Fig. 16.** Time history of the MGS and Odyssey short arc solutions for the zonal gravity coefficient  $\bar{J}_3$  where the typical arc length is 4 days. These arcs are delineated by the appropriate aphelion year ( $-180^\circ \leq M \leq 180^\circ$ ). The MGS data quality is best after September 2001 when the number of AMDs is reduced. The Odyssey data quality is best during the third cycle and is poorest in the last cycle 6, partly due to a decrease in frequency of tracking.

Our MGS gravity  $\bar{J}_3$  history depends to some extent on certain choices made with regard to the AMD modeling and the drag model. To demonstrate how these changes could alter our results, we shall discuss 3 plausible choices for the drag parameters and show how the resulting  $\bar{J}_3$  solutions differ from the nominally derived  $\bar{J}_3$ . Our drag model includes a global scale factor on the drag force for the entire arc, which is very loosely constrained. In addition to this, a drag coefficient ( $C_d$ ) is estimated for every 2-h orbit. Nominally, each  $C_d$  is estimated using an uncertainty of 2.0 and an initial value of 2.0 and constrained to an a priori value of 2.0. When we use a  $4\times$  tighter constraint on  $C_d$ , the scatter in the seasonal solution increases by  $\pm 5 \times 10^{-10}$  ( $\sim 2\times$  the scatter in Fig. 18). This indicates that there is some drag variability over the data arc that must be modeled. A drag model with the nominal uncertainty of 2.0 but with no a priori constraint, results in an increased seasonal signature of about  $0.7 \times 10^{-10} \cos(M + 5^\circ)$  and a secular change in  $\bar{J}_3$  of  $-0.57 \pm 0.14 \times 10^{-11}/\text{year}$  (formal

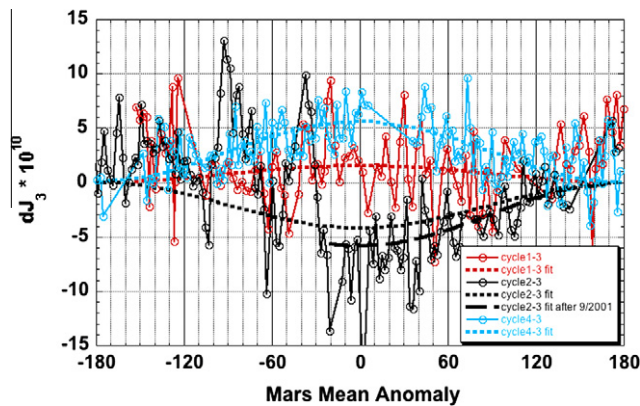


**Fig. 17.** Differenced zonal  $\bar{J}_3$  data, where we have matched each individual observation in cycle  $N$  with the corresponding nearest member in cycle 3. In each comparative cycle difference, we solve in a weighted least square sense for the function  $a(1 + \cos M)$ . The coefficient for cycle 1–cycle 3 is  $a = 0.76 \pm 0.28 \times 10^{-10}$ , and is small. The solution for cycle 4–cycle 3 is  $a = 2.79 \pm 0.15 \times 10^{-10}$ . The fit of cycle 2–cycle 3 depends on which set of data is included in the solution. If all data are included, then  $a = -2.10 \pm 0.32 \times 10^{-10}$ . However, if only data obtained after September 2001 ( $M > -10^\circ$ ) is included, then  $a = -2.91 \pm 0.18 \times 10^{-10}$ .

**Table 2**

Periodic solutions to the seasonal MGS 4-day  $\bar{J}_3$  solutions: (A) MGS  $\bar{J}_3$  3-frequency solution, and (B1, B2) MGS  $\bar{J}_3$  6-frequency solutions. Units are  $10^{-10}$ . The 3-frequency solution is a fit to just MGS cycle 3 and has a post-fit mean standard error of 2.8 for the residuals. Solution B1 is a fit to the adjusted MGS short arc solution for data after September 2002, excluding cycle 5. Here we have removed some outliers to improve the quality of fit, represented by the post-fit mean standard error of 2.3. B2 includes cycle 1 data, where about 10% of this data set (outliers) was removed to improve fit.

Coeff.	Soln. A		Soln. B1		Soln. B2	
	Solution	Error	Solution	Error	Solution	Error
Bias	-0.89	0.13	-0.75	0.08	-0.56	0.08
sin $M$	-28.90	0.18	-28.83	0.11	-28.90	0.11
cos $M$	-0.20	0.17	-0.31	0.11	-0.36	0.11
sin $2M$	-2.08	0.18	-2.01	0.11	-2.05	0.11
cos $2M$	0.54	0.18	0.73	0.11	0.88	0.11
sin $3M$	-1.35	0.18	-1.26	0.11	-1.22	0.11
cos $3M$	-2.42	0.18	-2.37	0.11	-2.34	0.11
sin $4M$			0.14	0.11	0.10	0.12
cos $4M$			-0.38	0.11	-0.38	0.11
sin $5M$			0.42	0.11	0.41	0.11
cos $5M$			-0.67	0.11	-0.59	0.11
sin $6M$			0.55	0.11	0.42	0.11
cos $6M$			-0.36	0.11	-0.48	0.11

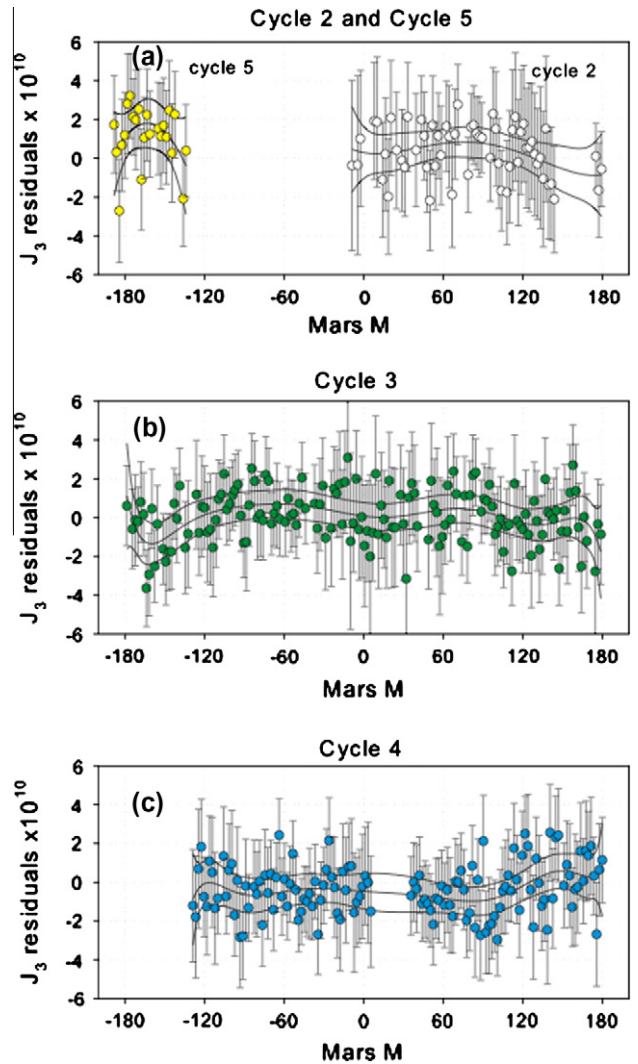


**Fig. 18.** Post-fit MGS  $\bar{J}_3$  residuals for cycles (a) 2 and 5, (b) 3 and (c) 4, after subtraction of the 6-frequency solution. Post-fit MGS  $\bar{J}_3$  residuals for cycles 1 and 2, prior to Sept. 2001 are not displayed, but have residuals  $\sim 2\times$  larger because of more AMDs. Each figure shows a polynomial regression fit and 99% confidence limits (based on data scatter).

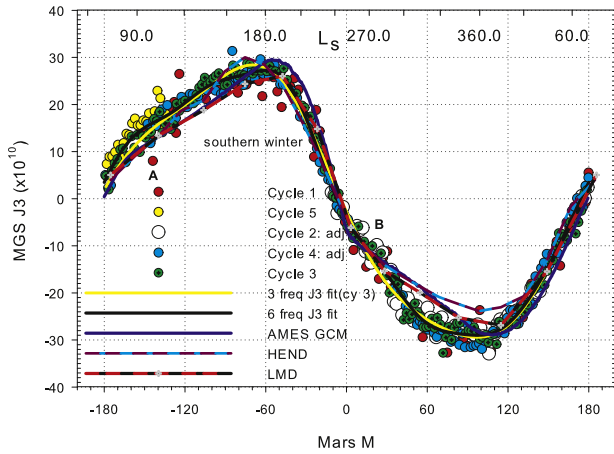


**Fig. 19.** The MGS  $\bar{J}_3$  history versus  $M$  and  $L_s$  after adjustment with  $a = \pm 2.8 \times 10^{-10}$  where only data after September 2001 is shown. Since the observed  $\bar{J}_3$  seasonal gravity is a sum of odd zonal coefficients, the sum of odd zonal history through degree 25 ( $W_{12}(\theta)$ ) of two zonal GCM models (AMES and LMD) and HEND model are graphed (Karatekin et al., 2005). Points A and B correspond to the end of north and south cap melting, respectively. The fits are good except at the extremes and the break at point B (end of south cap melting), especially for the AMES model.

error). This most likely indicates that some seasonal gravity signature can be absorbed in the drag model if the constraint is too loose.

The Odyssey  $\bar{J}_3$  solution happens to overlap part of the MGS  $\bar{J}_3$  history (see Fig. 16), and so we can examine the Odyssey residuals against the MGS  $\bar{J}_3$  model as a test of our analysis so far. The Odyssey data are considerably noisier, comparable to the first half of MGS cycle 2, which is mostly due to the geometry of the orbit being more face-on as viewed from Earth. Also, during northern winter ( $L_s \sim 330^\circ$ ), the  $\bar{J}_3$  Odyssey data require atmospheric dust corrections to the solar pressure model (same times as Fig. 5 and 6), otherwise large systematic trends appear. The Odyssey  $\bar{J}_3$  data appear to have higher maxima during southern winter ( $L_s \sim 180^\circ$ ). However, these peak discrepancies are less apparent if we examine the residuals relative to the MGS  $\bar{J}_3$  fit. The residuals (Fig. 20) do have a  $\cos M$  bow, but here it applies to the whole data set. However, there is no large bow of cycle 3 relative to cycle 4 in Odyssey data as seen in MGS data. Therefore, this MGS quadrennial signature is possibly caused by AMD modeling errors or other poorly modeled or unmodeled forces acting on the spacecraft - or some feature of our analysis. In fact, a similar analysis by Smith et al. (2009) of MGS tracking data does not seem to detect a  $\cos M$  bow, nor do they detect a significant reduction in arc sigma's after September 2002. A 3-frequency fit of the Odyssey gravity relative to the MGS B1 6-frequency model of Table 2 is obtained from the residual curve and is given by

$$\delta\bar{J}_3 = (1.2 \cos M - 1.1 \sin M + 0.05 \cos 2M - 0.06 \sin 2M + -0.39 \times \cos 3M - 1.2 \sin 3M) \times 10^{-10},$$

and the secular drift in the Odyssey  $\bar{J}_3$  data is limited to  $0.9 \pm 0.9 \times 10^{-11}$ /year. The Odyssey data seem to be in better agreement with the HEND and AMES (Haberle et al., 2008) and LMD (climate data base version 4.2) GCM models near the southern winter peak.

The GCM models include the effect of global changes in both ice and atmosphere, just as our gravity data includes both. However, the HEND and NS models infer just ice mass. An estimate of the correction can be obtained from both the AMES and LMD GCM models. The 3-frequency fit for each are

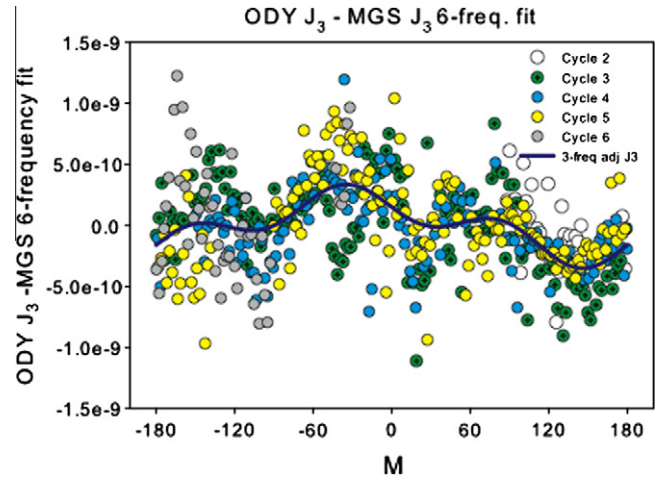


**Fig. 20.** Odyssey  $\bar{J}_3$  cycle residuals (minus MGS 6-frequency solution) and a 3-frequency fit of the Odyssey residuals relative to the 6-frequency MGS solution.

$$\delta\bar{J}_3(\text{AMES, air}) = (0.61 \sin M + 1.29 \cos M + 0.24 \sin 2M + 0.23 \times \cos 2M + -0.18 \sin 3M + 0.14 \cos 3M) \times 10^{-10},$$

$$\delta\bar{J}_3(\text{LMD, air}) = (0.21 \sin M + 0.76 \cos M + 0.20 \sin 2M + 0.10 \times \cos 2M + -0.05 \sin 3M + 0.10 \cos 3M) \times 10^{-10}.$$

LMD  $\delta\bar{J}_3$  is about 50% the amplitude of the AMES result, so there is the question (unanswered here) of which result is more valid. We shall adopt the LMD model in the following analysis, based on the fact that LMD model is a better fit to the MGS data than is the AMES GCM.

In addition, each  $\bar{J}_n$  must be multiplied by  $1 + k'_n$  to correct for deformation of the mantle by the overlying mass load (see Tables 3a and 3b; Metivier et al., 2008). The Love load number is  $k'_n = k_n - h_n$ , where  $k_n$  and  $h_n$  are the potential and radial surface displacement Love numbers generally associated with tides. For  $\bar{J}_3$ , this correction is about 7% for a tidal model with  $k_2 = 0.158$ , while for  $\bar{J}_2$ , this correction is about 14%. The model estimates for  $\bar{J}_n$  should also include at least a modest correction for elevation that takes into account that the poles are low relative to the mean radius. The zonally averaged surface radius relative to the center-of-mass is represented by the series

$$r(\theta) = 3390.00 \left( 1 + \sum c_{n0} \bar{P}_n(\theta) \right) \text{ km},$$

where  $\bar{P}_n(\theta)$  is a normalized Legendre function dependent on colatitude  $\theta$ . The first three terms are

$$r(\theta) = 3389.5 - 3.0 \cos \theta - 13.4(1.5 \cos^2 \theta - 0.5).$$

The net effect of this correction is to reduce the estimated  $\bar{J}_n$  at the north pole by about 6% and the south pole by 4%. The explicit integral for each  $\bar{J}_n$  is

$$\bar{J}_n = -\frac{2\pi R_e^2}{M_{\text{Mars}}} (1 + k'_n) \int d\theta \left( \frac{r(\theta)}{R_e} \right)^{n+2} \sigma(\theta) \bar{P}_n(\theta),$$

where  $\sigma(\theta) = \sigma_{\text{ice}} + \sigma_{\text{air}}$  is the zonally averaged, combined column density of ice and air mass. A more accurate estimate includes the longitudinal variations in column density and topography, but this is a second order effect that changes results by less than 1%. For comparison purposes, the resultant seasonal curve should be adjusted such that the area under the curve vanishes (i.e. is a purely periodic signature).

**Table 3a**

Tidal Love numbers:  $k_n, h_n, l_n$ .

$n$	Model A			Model B			Model C*		
	$k_n$	$h_n$	$l_n$	$k_n$	$h_n$	$l_n$	$k_n$	$h_n$	$l_n$
2	0.1636	0.3021	0.0510	0.1622	0.3016	0.0517	0.1529	0.2863	0.0512
3	0.0504	0.1372	0.0086	0.0503	0.1368	0.0094	0.0483	0.1309	0.0107
4	0.0230	0.0818	0.0038	0.0223	0.0831	0.0042	0.0234	0.0829	0.0049
5	0.0135	0.0592	0.0022	0.0140	0.0611	0.0025	0.0144	0.0638	0.0028
6	0.0092	0.0475	0.0014	0.0096	0.0497	0.0016	0.0100	0.0523	0.0017
7	0.0068	0.0405	0.0009	0.0071	0.0426	0.0010	0.0075	0.0450	0.0010
8	0.0052	0.0356	0.0006	0.0054	0.0374	0.0007	0.0058	0.0404	0.0008
9	0.0042	0.0319	0.0004	0.0044	0.0334	0.0004	0.0044	0.0373	0.0004

Model A corresponds to  $R_f = 1800$  km,  $\chi_M = 85\%$ ,  $\Delta T = -200$  K and  $h_{cr} = 50$  km. Model B has  $R_f = 1750$  km,  $\chi_M = 81\%$ ,  $\Delta T = 0$  K and  $h_{cr} = 75$  km. Model C\* has  $R_f = 1650$  km,  $\chi_M = 76\%$ ,  $\Delta T = 200$  K and  $h_{cr} = 100$  km. The load  $k'_n = k_n - h_n$ .

**Table 3b**

Model structure parameters.

Parameter	Model A	Model B	Model C*
$C/MR^2$	0.3647	0.3642	0.3647
$C_f/MR^2$	0.0271	0.0241	0.0187
$R_f$	1800 km	1750 km	1650 km
$k_{2M}$	0.1350	0.1397	0.1356
Wobble period (d)	203.5	204.9	206.9
FCN period (d)	279.3	296.7	309.6
Nutation $F$ factor	0.0545	0.0474	0.0360
$e_f$	$4.333 \times 10^{-3}$	$4.268 \times 10^{-3}$	$4.165 \times 10^{-3}$
$\beta m_R$	$1.015 \times 10^{-3}$	$1.034 \times 10^{-3}$	$1.017 \times 10^{-3}$
$\gamma m_R$	$1.392 \times 10^{-3}$	$1.417 \times 10^{-3}$	$1.393 \times 10^{-3}$

Wobble frequency is  $\sigma_W = \omega MR^2 \left[ \sqrt{j^2 - C_{22}^2} / (C - C_f) \right] (1 - k_{2M}/k_0)$ . The secular Love  $k_0 = 3/2 m_R \approx 1.30$ , where  $m_R = g/\omega^2 R$ . The wobble frequency probably should be reduced by 1% to account for anelastic softening with frequency. The core nutation frequency (FCN) is  $\sigma_{FCN} = \omega(C/(C - C_f))(e_f - \beta m_R)$ , where  $e_f$  is the core ellipticity (taken to be its hydrostatic value) and  $\beta$  is an elastic correction. The nutation factor  $F = [C_f/(C - C_f)](1 - \gamma m_R/e_f)$  determines the scale of the mantle response to forced nutations of the fluid core. Also, the load  $k'_{2M} = -k_{2M}$ .

There is the question of just how many  $\bar{J}_n$  should be included for the sum to converge to an acceptable accuracy level. As a first cut, we first considered limiting the spherical harmonic decomposition to degree 3 through 9 with the observed gravity sum of odd zonals, and then compared it to results as more terms are added. It turns out that rate of convergence depended of the model. An NS data set with  $2^\circ$  spacing in latitude changed by about 1% (decrease) in going from 4 to 8 coefficients (i.e. to degree 17). On the other hand, the LMD model with  $3.75^\circ$  latitude spacing, this change is 5% and for AMES with  $5^\circ$  spacing the change is 7%. The HEND data (Litvak et al., 2005) consist of 4 overlapping bands down to  $\pm 60^\circ$  latitude. We obtained three discrete bands and interpolate in order to construct ice cap history.

An alternative approach is to replace the explicit calculation of each  $\bar{J}_n$  with a weighting function  $W_j(\theta)$  that sums the first  $j$  odd zonal terms. Thus  $W_1(\theta)$  includes just the  $\bar{J}_3$  term and is proportional to  $P_3(\theta)$  while  $W_4(\theta)$  includes the  $\bar{J}_3, \bar{J}_5, \bar{J}_7$  and  $\bar{J}_9$  contributions and is therefore a combination of the corresponding Legendre functions. The odd zonal sum to compare to gravity is then

$$\bar{J}_3 + 1.238\bar{J}_5 + \dots = -\frac{2\pi R_e^2}{\sqrt{7}M_{Mars}} \int_{180}^0 d\theta \sigma(\theta) W_j(\theta) \sin \theta.$$

Thus  $W_j(\theta)$  includes corrections for load Love number (Model B of Table 3a) and shape corrections  $R(\theta)$  as above. The disadvantage of this approach is that the weighting function depends on spacecraft orbit.

Fig. 21 illustrates just how slowly the resulting  $W_j(\theta)$  appears to converge and just where this function is most sensitive. The first peak moves inward towards the pole as more terms are added and reaches a limit of about  $8^\circ$  colatitude. The peak for  $W_4(\theta)$  is

at  $12^\circ$ . The change in position of the peak and the latitude spacing for each model combine to affect the resultant accuracy. The four component model works as well as it does partly due to the fact that the ice cap column density monotonically decrease in amplitude from the poles, and the overall integral changes modestly as more terms are added. Two models are obtained at discrete intervals in aerocentric solar longitude  $L_s$  (HEND,  $15^\circ$ ; LMD,  $30^\circ$ ; NS, about  $11^\circ$ ), and construction of each map may involve some temporal and spatial averaging.

The HEND and NS data are possibly the more interesting in that they depend on global data of thermal neutron counts that are indicative of subsurface ice. The basic premise is that high-energy neutrons are reduced in energy by collisions with hydrogen atoms, which happen to concentrate in water ice. Estimates for  $CO_2$  ice mass results from its effect in changing this buried water ice signature by simply covering the rocky surface. Neutrons are slowed by both hydrogen and  $CO_2$ , except that it takes many more collisions in a  $CO_2$  rich layer for neutrons to attain a thermal-like status. The spacecraft instruments measure neutrons in three energy bands: thermal, epithermal (0.5 eV to 0.7 MeV) and ‘fast’ or high energy. Prettyman et al. (2009) concentrate on the epithermal band for the  $CO_2$  cap column density and employ the other two bands to either calibrate the epithermal signal or detect other features such as the enrichment of  $N_2$  and Ar during the buildup phase of the southern cap from the thermal band. The effect of adding a  $CO_2$  layer is to increase the backscattered, epithermal signal observed at the spacecraft instrument.

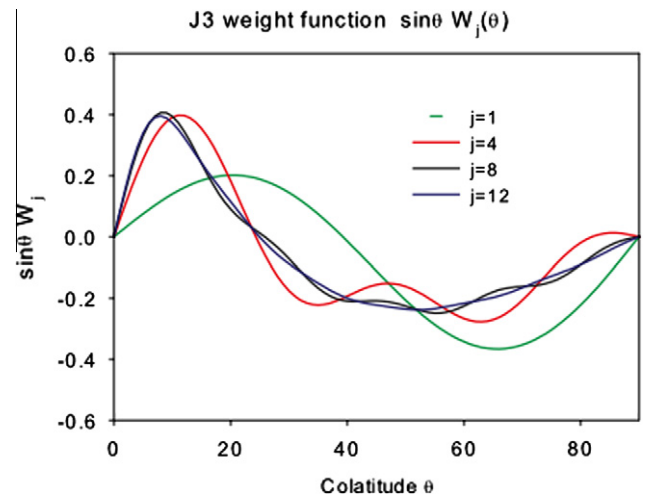


**Fig. 21.** The function  $\sin \theta W_j(\theta)$  for the northern hemisphere for the MGS mean orbit. This includes loading corrections using model B (Table 3a). The southern  $W_j(\theta)$  has opposite sign, and the peak near  $8^\circ$  is about 2% larger because this pole is about 6 km higher than the north pole.

There is also the question of whether there exists scaling errors in any of these data sets. In the analysis of NS data, they use a semi-infinite single layer ice rich medium in modeling the neutron backscatter signal, and two layer models generally result in larger amplitudes. The NS north cap peak amplitude in the 80–85° band is  $65 \pm 5 \text{ gm/cm}^2$ , while the statistical uncertainty (i.e. data noise) is less than  $\pm 2 \text{ gm/cm}^2$ . Clearly, the major uncertainty is related to appropriate ‘model’ (e. g. uniform or layered subsurface, soil water content, etc.). So a 10% scaling error is within the realm of plausibility.

Recently, we obtained 2 years of NS ice cap data binned at  $2^\circ$  in latitude (Prettyman et al., 2009). The bin size in longitude varies from eight segments for the  $\pm 89\text{--}87^\circ$  latitude band to 60 for the  $\pm 59\text{--}61^\circ$  band. Prettyman also supplied data extending to latitudes below  $\pm 60^\circ$  that is outside the region of validity of the analysis (see Table 1 for a summary of error sources in Prettyman et al. (2009)). We have retained two additional bands down to  $\pm 35^\circ$ . Although this low latitude binned data is less accurate, it happens that this extra data changes the model (decreases)  $\bar{J}_3$  near cap maximum by only 2–3%.

The temporal spacing is about  $11^\circ$  in aerocentric true solar longitude  $L_s$ . The 2 years of NS data (Mars year 26 and 27) roughly coincide with cycle 3 and 4, except that the range is  $0^\circ \leq L_s \leq 360^\circ$ . Since one of the issues that concerns us is the  $\cos M$  change from cycle to cycle that is seen in the MGS data, we have obtained the equivalent cycle 3 data from the 2 years of data and then constructed the cycle 4 data by combing the last  $\frac{3}{4}$  of year 27 and the first  $\frac{1}{4}$  of year 26 (covering  $106^\circ \leq M \leq 180^\circ$ ).

In order to determine a potential scale error, we have compared the mean amplitude of the primary  $\sin M$  term in both NS ice data and MGS and find that NS is about 8.6% smaller than MGS. We have decided to rescale this data a factor of 1.09 so that the  $\sin M$  amplitudes match in order more fully study other features of the data.

For cycle 3, both the derived NS model  $\bar{J}_3$  and the MGS data agree to within 5% everywhere except near the winter peaks where it increases to about 10%. Note this north pole anomaly is apparent in the other data sets. Prettyman uses two methods to reduce the NS data. One is to simply bin the observed signal without regard for signal spill-over from nearby regions (smoothed). The second approach is to employ image sharpening techniques (deconvolved). The deconvolved map obtains significantly larger column densities (up to 5–10%) inside  $\pm 5^\circ$  colatitude and near the cap edge. However, since the differences fall off as colatitude increases, the end result is relatively minor in the observed  $\bar{J}_3$ . The largest observable effect is a 2–3% increase near the south pole maximum (see Fig. 22a and b) for the deconvolved NS  $\bar{J}_3$  relative to the smoothed NS  $\bar{J}_3$ . The smoothed NS agrees slightly better with MGS  $\bar{J}_3$ , although we shall concentrate the remainder of the discussion on the deconvolved NS data set. By the way, the reference radius for this NS data set is 3389.5 km.

Prettyman et al. (2009) obtains a larger south pole maxima for cycle 4 compared to cycle 3 that, unfortunately, is not confirmed by comparison with the MGS data (see Fig. 22a and b). The south pole maximum is about 6% larger in cycle 4 than cycle 3. There is also a  $\cos M$  bow in the NS cycle 4 data relative to cycle 3 that is about  $\frac{1}{2}$  as large as seen in the un-adjusted MGS cycle 4 data (about  $\alpha = 1.3(1 + \cos M) \times 10^{-10}$ ). Thus, in Fig. 22a, we have adjusted the MGS cycle 4 data such that it has a bow of similar magnitude relative to MGS cycle 3. There is a large discrepancy in the southern buildup for cycle 3 that is about  $\frac{1}{3}$  weaker in cycle 4. This feature may be partly related to the fact the NS ice cap model does not include the effect of changing  $N_2$  and Ar atmospheric concentrations from year to year in their estimate of  $CO_2$  column densities (Prettyman, private communication). Increased concentration of  $N_2$  and Ar might depress the  $CO_2$  estimate by perhaps as much as 5–10%. These gas concentrations are especially large in year 26

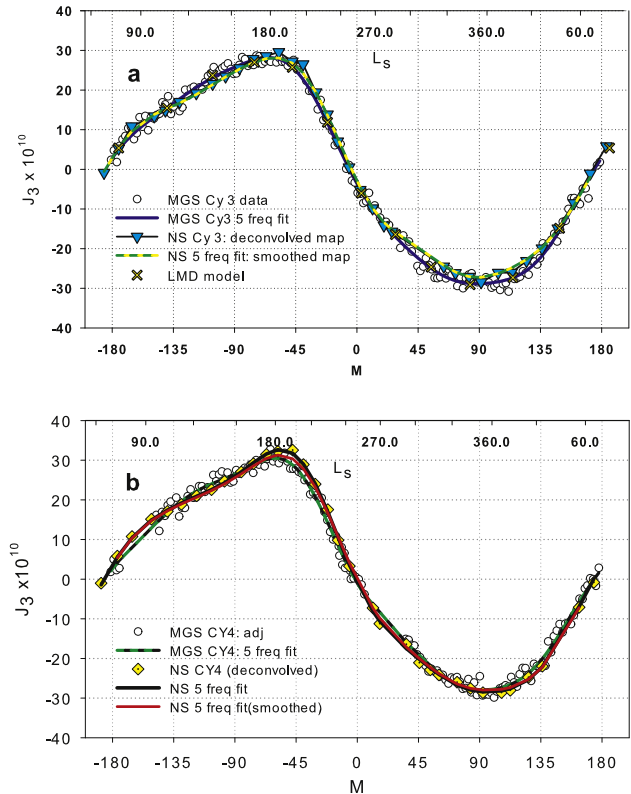


**Fig. 22.** Comparison of  $\bar{J}_3$  from MGS 5-frequency fit and NS data for (a) cycle 3 and (b) cycle 4. The NS data use a deconvolved model and similar fit derived using the  $W_{12}(\theta)$  weighting function. The NS data has been rescaled by a factor of 1.09 so that the  $\sin M$  terms match. The red line represents the NS  $\bar{J}_3$  that was derived from the smoothed mapping technique. LMD GCM model (without pressure correction) is obtained using  $W_{12}(\theta)$  and is shown for comparison in (a). The solutions are limited to five frequencies because of gaps in cycle 4.

compared to year 27 during the south cap buildup. However, the center of this broad feature is near  $L_s = 100^\circ$  ( $M = -140^\circ$ ), while that seen in  $\bar{J}_3$  (Fig. 22a) covers  $-130^\circ \leq M \leq -100^\circ$ . Another remarkable feature of the NS and MGS data is that the north pole minimum agree in cycle 4 just where they differed in cycle 3 and, for this, we have no ready explanation.

There are other model deficiencies that might account for some of the differences that are common to both years of data. Prettyman et al. (2009) employ a standard atmosphere at each pole and do not include the seasonal changes air column density. This should affect the north pole more than the south, given that it is about 6 km lower. As mentioned earlier, we could have adopted a solution with different drag model constraints, one that had a slightly larger  $\cos M$  term. Finally, some of the discrepancies that occur either figure occur in data gaps in one of the two data sets and so might be discounted.

We can difference the periodic fit of cycles 3 and 4 and examine if the changes seen in NS data agree with MGS results (Fig. 23a). Differencing should cancel any common modeling errors. The only coherent difference is the  $\cos M$  bow we altered in cycle 4. There is about a 6% change in the  $\sin M$  amplitude for NS that is not seen in the MGS cycle 4–cycle 3 difference. This same signature is also present in the ‘smoothed’ NS data. Except for the  $\cos M$  bow, the MGS solution appears to be more flat, given that the second largest term is a  $0.7 \times 10^{-10} \cos 4 M$  term. Still, we cannot discount that the NS yearly change could be real. Also, a  $\cos M$  bow might represent a phase shift in the timing of the accretion and melting of the  $CO_2$  ice caps that could reflect a change in overall temperature or dust content. Dust storms might contribute to such a process,



although it should be said that the dust storm activity in year 26 and 27 were both very similar and mild (McDunn et al., 2010). The doubly differenced residuals should be flat (and possibly noisy) if MGS and NS captured the same change. Instead, we find a step-like function that is remarkably smooth during southern winter. This runs counter to the idea that atmospheric N<sub>2</sub> and Ar changes seen in NS thermal neutron data are an important influence on ice cap estimates. The gross feature seen in the doubly differenced

data is apparently related to the relative change in NS northern winter from cycle 3 to 4.

Comparisons of the means solutions for cycles 3 and 4 for each data set reveal some curious results (see Fig. 23b). So far, we have neglected the pressure correction to ice cap models and the possibility that the Odyssey solution might be more valid. First of all, the AMES GCM model and HEND data are both much poorer fits to the mean MGS solution than is either the LMD GCM or NS data. Possibly, the grid size may play a role. The 3-frequency Odyssey corrections appear to be correlated with these residuals. If we subtract this correction from the NS residuals, we find a modest reduction in overall RMS residuals from  $\pm 1.7 \times 10^{-10}$  to  $\pm 1.3 \times 10^{-10}$ . However, over the last  $\frac{3}{4}$  of the season the reduction is significantly better. There is still a significant first harmonic component in the  $\delta\bar{J}_3(NS - ODY)$  residual:  $\delta\bar{J}_3 = 1.2 \sin M + 0.7 \cos M$ . If we had used the AMES model correction for air pressure  $\bar{J}_3$ , these residuals would have been even larger.

The NS ice cap maps are obviously a much richer source of information than is the gravity signal in  $\bar{J}_3$ . This gravity  $\bar{J}_3$  is just a one-dimensional mapping in time of a weighted global average of the ice cap mass, whose magnitude is especially sensitive to mass contributions near polar colatitude  $\pm 8^\circ$ . The NS maps beyond  $\pm 30^\circ$  colatitude are much less reliable, mainly because of low concentration of subsurface water ice. Another important point is that the southern maximum as seen in our gravity  $\bar{J}_3$  occurs near  $L_s = 184^\circ$  while a similar change in say the  $\bar{J}_1$  ice component occurs about  $20^\circ$  earlier. Thus the CO<sub>2</sub> ice sheet sublimates at the cap perimeter while still accumulating near the pole (Prettyman et al., 2009). This means that the timing of maximum mass growth as inferred from the  $\bar{J}_1$  component and the maximum attained near the pole (as inferred from gravity  $\bar{J}_3$ ) differ in time by about 40 days. Therefore, extending cap ice mass contributions to lower latitudes (which peak earlier) can distort the shape of  $\bar{J}_3$  near the top as well as change the amplitude of  $\bar{J}_3$ . In fact, distortion in the southern peak seems to be the major factor based on maps supplied by Prettyman.

The  $\bar{J}_3$  signature is not the only source of ice cap temporal history. However, the observed  $\bar{J}_2$  history from gravity is much less precise than the  $\bar{J}_3$  history. Part of the reason is that this signature is somewhat erratic is that the spacecraft signal is caused by out-of-plane perturbations for spacecraft nodal longitude, much like the case involving the detection of Mars  $k_2$  Love number (see next section), and so the resultant signature shows a dependence on spacecraft plane orientation relative to Earth. It happens that the Odyssey spacecraft provides a more reliable signature than MGS.

The expression for the observed  $\bar{J}_2$  for the Odyssey spacecraft is

$$\bar{J}_2 = (1 + k'_2)\bar{J}_2 + 2.00(1 + k'_4)\bar{J}_4 + 2.78(1 + k'_6)\bar{J}_6 + 3.30(1 + k'_8)\bar{J}_8 + \dots$$

Again, we should also correct for atmospheric pressure and expand the number of gravity coefficients, but is obviously not necessary since the HEND  $\bar{J}_2$  signature is much more irregular than earlier, displaying the effects of subtraction of the north and south histories inherent in this even degree sum, and spacecraft orientation sensitivity. It happens that the shape of the equivalent weighting function for  $\bar{J}_2$  is just as sensitive to the number of coefficients included in the sum as was  $\bar{J}_3$ . However, the overall integral changes by less than 5% ingoing from 4 to 16 terms. The 2-frequency fit to the Odyssey data is

$$\bar{J}_2 = [1.4 \sin(M - 40^\circ) + 1.8 \sin(2M + 57^\circ)] \times 10^{-9},$$

and agrees reasonably well with HEND, except near perihelion in the range  $-90^\circ < M < 30^\circ$  (see Fig. 24). Thus we can confirm the signal, but it is clear that it cannot provide a useful test of either

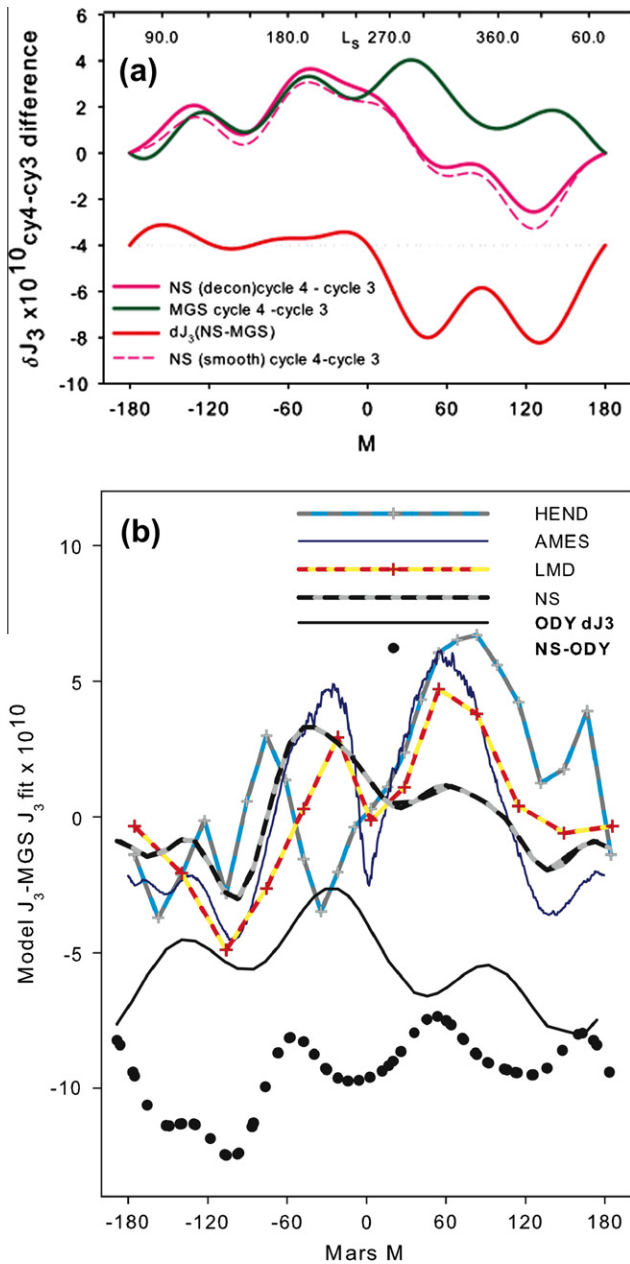


**Fig. 23.** (a) Search for inter-annual signature in NS and MGS cycles 3 and 4 by comparing the cycle 4 minus cycle 3 residuals. Also included is the differenced residual using the smoothed NS data. This graph includes a doubly differenced residual:  $\delta\bar{J}_3(NS) - \delta\bar{J}_3(MGS)$ . Again, the NS data has been rescaled by a factor of 1.09. Note that the  $\cos M$  component of cycle 4  $\delta\bar{J}_3(MGS)$  has been adjusted such that this term vanishes in the doubly differenced residual. Also, we have forced the start point of cycle 4 to match the end point of cycle 3. (b) Comparison of the GCM'S, HEND AND NS modeled  $\bar{J}_3$  seasonal history with MGS mean solution B1. (Table 2) The models are obtained using the weighting function  $W_{12}$ , and the neutron determined ice maps are corrected with the LMD  $\delta\bar{J}_3(LMD, air)$ . The Odyssey 3-frequency correction to MGS is displayed as well, as is the difference between the mean NS residuals and Odyssey (curves are shifted down for clarity).

the ice map accuracy or the corresponding atmospheric mass change.

The even zonal gravitational harmonic coefficients involve the sum of the mass change in the north and south hemispheres. Changes in these gravity coefficients should reflect the change in ice mass or atmospheric mass (or mean pressure). The global average of ice mass and air pressure should balance out (air mass + ice mass = 0). The global average of NS ice cap data can be compared to GMC model data (which enforce mass conservation) or air pressure maps. The only ground-based data constraining air pressure are the local pressure measurements taken by the Viking landers. Fig. 25 shows changes in ice mass for the 2 NS cycles, the LMD GCM model and a scaled estimate of the mean pressure using Viking 1 data (Yoder and Standish, 1997). The NS data has not been rescaled here or in the previous figure, in part to show the good agreement between LMD and NS data. NS cycle 3 (year 26) and LMD model agree well nearly everywhere, except near  $M = 0$  and during north ice cap growth, one of the same regions of disagreement for  $\bar{J}_3$ . On the other hand, NS cycle 4 differs substantially with LMD during the decay of both north and south caps. Inflating NS data by 9% would substantially reduce the difference between NS and Viking air pressure.

In summary, the seasonal changes in the gravity match to 5–20% with the GCM models and Odyssey NS and HEND data. The best agreement, by far, is with the Odyssey NS data (after it has been rescaled) and LMD GCM, especially if we compare the average of the 2 years of NS data with an MGS data set corrected with a 3-frequency fit to all Odyssey data. The HEND model is a slightly poorer match with gravity results versus the AMES GCM. However, if HEND data set were rescaled, one could improve the fit. Inter-annual signatures observed in the NS between martian year 26 and 27 are *not* seen in MGS. Unfortunately, Odyssey results are too noisy to provide an additional test. Odyssey may provide a better long-term average than MGS, at least based on a 3-frequency fit to the global data. It may be that inter-annual detection is limited first by AMDs and then other error sources (primarily drag). The MRO tracking data is not expected to help extend the seasonal gravity monitoring due to the large drag errors. Future missions would need to reduce nongravitational forces to improve seasonal gravity detection. This most likely implies a mission with a high quality accelerometer ( $\sim 10^{-10}$  m/s<sup>2</sup>) and Ka-band Doppler tracking (<0.01 mm/s).

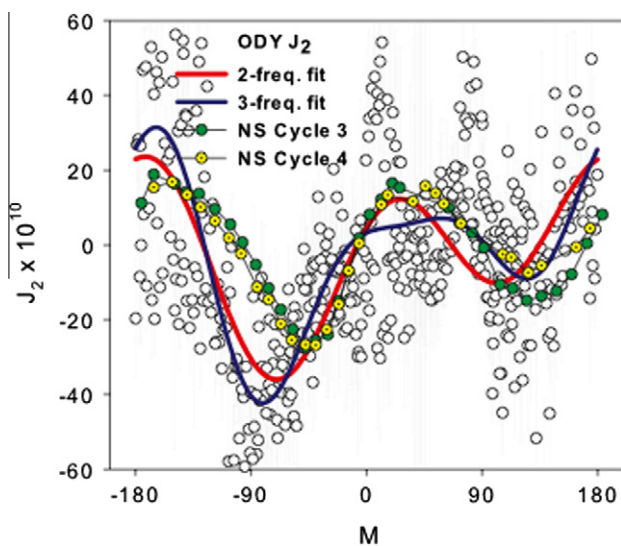


Fig. 24. Odyssey short arc solutions for  $\bar{J}_2$  gravity plotted versus mean anomaly  $M$ . The HEND load compensated  $\bar{J}_2$  is also shown, together with 2 and 3-frequency fits to the gravity data.

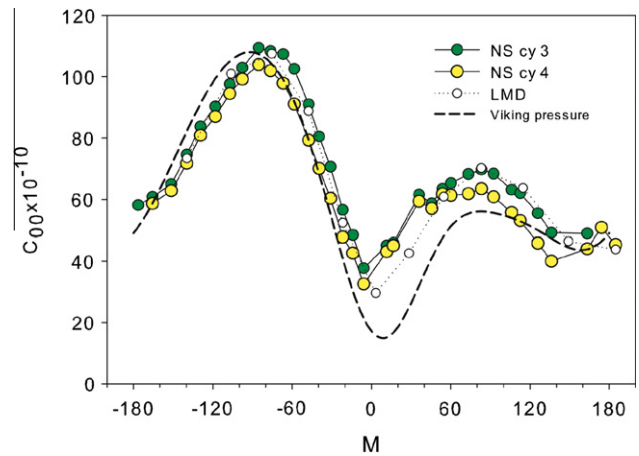


Fig. 25. Change in ice cap mass from of  $C_{00}$  ( $C_{00} = -J_0$ ) for ice caps (excess ice mass =  $C_{00} M_{Mars}$ ). Models include NS ice caps, the LMD GCM and Viking 1 scaled pressure:  $\delta P_r(t)/g_{Mars} = -\delta C_{00}(ice)M_{Mars}/4\pi R_0^2(5.3/7.4)$ . Local Viking 1 mean pressure is 7.4 mbar while global mean pressure is 5.4 mbar.

## 7. Mars Love number and fluid core size

The Mars  $k_2$  solar tide is determined from the secular drift in orbit inclination amounting to about a 1-m/day change (Yoder et al., 2003), and consequently, it is best determined when the orbit plane is face-on when viewed from the Earth. The  $k_2$  solutions for each spacecraft are presented in Table 4 along with other published values (Lemoine et al., 2006; Balmino et al., 2005; Marty et al., 2009). The best MGS  $k_2$  solution is

$$K_2 = 0.173 \pm 0.009$$

and is the most accurate solution of the three spacecraft. It is comparable to our previous result (Konopliv et al., 2006) and is slightly larger than Yoder et al., 2003. The MGS solution is less sensitive to atmospheric drag assumptions than Odyssey, and MGS solutions are consistent between data sets with different AMD frequency. Because of the favorable Sun angle and smaller orbit normal force component, it is less sensitive to solar radiation pressure errors than Odyssey. However,  $k_2$  accuracy is still limited by assumptions on the solar array and bus solar pressure reflection properties as well as uncertainties in the Mars pole. The MGS uncertainty presented in Table 4 is five times the formal uncertainty. The range of solutions observed for MGS based upon different assumptions fit within the uncertainty. In our nominal solution  $\text{Im}(k_{22})$  is not estimated, but when estimated,  $\text{Im}(k_{22}) = 0.02 \pm 0.03$ . The uncertainties are five times the formal uncertainty. This more realistic uncertainty is about five times larger than what one would need to detect the atmospheric tide.

In previous results (Konopliv et al., 2006), we postulated that Mars Odyssey Love number solutions were dependent on which thruster pair was used for AMDs, with suspect  $k_2$  solutions for thrusters 1 and 2. As mentioned above, it is now believed that this anomalously low value was caused by not modeling atmospheric dust in the solar radiation pressure force. Almost all of the arcs in Fig. 5 and 6 that are affected by dust use thrusters 1 and 2 for AMDs. Once a dust correction to a 30–40 km altitude or higher is applied, Odyssey  $k_2$  solutions are consistent ( $k_2 = 0.104$  becomes 0.164–0.172). Solutions using only arcs without suspect atmospheric dust contributions give the most reliable Odyssey solution ( $k_2 = 0.172 \pm 0.014$ ). Since Odyssey is more sensitive to atmospheric drag and solar pressure errors, uncertainties in Table 4 are 10 times the formal uncertainty. The ten times formal

**Table 4**  
Mars  $k_2$  Love number solutions.

Spacecraft	Re( $k_2$ ), Im( $k_2$ ) = 0	Re( $k_2$ ), Im( $k_2$ ) = 0.01	Re( $k_2$ ), Im( $k_2$ ) est.	Notes
MGS	0.173 ± 0.009	0.168 ± 0.009	0.159 ± 0.016 0.023 ± 0.025	Best overall solution this paper Im( $k_2$ ) = 0, 5× formal $\sigma$
MGS	0.153 ± 0.017			Data to April 14, 2002, Yoder et al. (2003)
MGS	0.166 ± 0.011			Data to December 5, 2004, Konopliv et al. (2006)
ODY	0.172 ± 0.014	0.185 ± 0.014	0.167 ± 0.025 −0.004 ± 0.016	Without arcs affected by dust, best Odyssey solution Im( $k_2$ ) = 0, 10× formal $\sigma$
ODY	0.104 ± 0.013		0.015 ± 0.021 −0.076 ± 0.014	All arcs but with no dust model
ODY	0.161 ± 0.013	0.173 ± 0.013	0.131 ± 0.022 −0.025 ± 0.014	All arcs but with dust model to 30–40 km
ODY	0.172 ± 0.013	0.184 ± 0.013	0.154 ± 0.022 −0.015 ± 0.014	All arcs but with dust model to 30–50 km
MRO	0.175 ± 0.010	0.175 ± 0.010	0.176 ± 0.010 0.036 ± 0.040	10× formal $\sigma$
<i>Other determinations</i>				
MGS	0.201 ± 0.059 0.163 ± 0.056			Bills et al. (2005)
MGS	0.176 ± 0.041			Lemoine et al. (2006)
MGS	0.130 ± 0.030			Balmino et al. (2005) (see Marty et al., 2009)
MGS + ODY	0.120 ± 0.003			Marty et al. (2009)

**Table 5**  
Mars orientation parameters used in the MRO110B gravity solution. For the estimated parameters, the uncertainties are 15 times the formal statistics (see Fig. 18, Konopliv et al., 2006).

Orientation parameter	Value	Uncertainty	Units
$N$	3.37919183	Fixed	Degrees
$J$	24.67682669	Fixed	Degrees
$\Omega$	49.6167	Fixed	Degrees
$\varepsilon$	23.4392811	Fixed	Degrees
$\chi$	46.5307	Fixed	Degrees
$i$	1.85137	Fixed	Degrees
$\psi_o$	81.9683722358	0.000016	Degrees
$\dot{\psi}_o$	−0.000005772	0.000000007	Degrees/day
	−7590	10	Milliarcsec/year
$l_o$	25.1893792424	0.000010	Degrees
$\dot{l}_o$	−0.000000003	0.000000005	Degrees/day
$\phi_o$	133.38462	Fixed	Degrees
$\dot{\phi}_o$	350.891985303	0.000000012	Degrees/day
$F$	0.07	Fixed	Unitless
$\sigma_o$	−1.5	Fixed	Degrees/day

uncertainty for the Odyssey Im( $k_{22}$ ) for the arcs unaffected by dust is about 0.02.

The Love number solutions from MRO tracking only ( $k_2 = 0.175$ ) agree fairly well with that of MGS and Mars Odyssey as shown in Table 4, giving a consistent and independent verification of the Mars love number from all three spacecraft. Like MGS, MRO  $k_2$  solutions are not as sensitive to solar pressure model errors such as dust. However, MRO may have other remaining model errors perhaps due to HGA motion or atmospheric drag. For this reason, uncertainties in Table 4 are 10 times the formal uncertainty. The MRO Im( $k_{22}$ ) uncertainty is 0.04 (10 times formal).

The observed  $k_2$  must be corrected for solid tidal friction, atmospheric tide, and anelastic softening before it can be employed, together with an interior structure model, to constrain fluid core size. An estimate of the atmospheric parameter  $k_{22}^a \cong 0.008$  is obtained from Pathfinder observations of local pressure changes and simple models that scale this to a global pressure wave. The Pathfinder pressure wave (J.T. Schofield, private communication; Yoder et al., 2003 in SOM) that includes four frequencies is

$$P/P_0 = (0.021 \cos(\alpha - 85^\circ) + 0.011 \cos(2\alpha + 41^\circ) + 0.002 \cos(3\alpha + 42^\circ) + 0.001 \cos(4\alpha - 81^\circ)).$$

The diurnally changing angle is  $\alpha = 0^\circ$  at midnight. The resulting model estimate for tidally changing ( $C_{22}/S_{22}$ ) is accurate to about

10%, while contributions from other atmospheric semi-diurnal (e.g.  $C_{42}/S_{42}$ ) and  $1/4$  day tidal constituents ( $C_{44}/S_{44}$ ) are also no more than 10%.

The solid friction phase shift is deduced from the tidal change in Phobos' orbit and is about  $0.53^\circ$ . Jacobson (2010) obtains for the mean motion

$$\frac{d}{dt} n_{\text{Phobos}} = 25.12 \pm 0.08^\circ / \text{Cyr}^2,$$

and is close to his earlier determination (Jacobson et al., 1989). Bills et al. (2005) have also reported a new value that is about 10% larger. This positive rate means that the orbit is contracting. If we relate this to the tide distortion of Mars by Phobos, we find (Yoder, 1982, 1995)

$$\frac{d}{dt} n = \frac{9}{8} \frac{M}{M'} \left( \frac{R'}{a} \right)^5 n^2 \times \left( 4k_2 \sin \delta_{2200} + \frac{R^2}{a^2} k_3 (5 \sin \delta_{3300} + \sin \delta_{3110}) + \frac{5}{6} \frac{R^4}{a^4} k_4 (7 \sin \delta_{4400} + 2 \sin \delta_{4410}) \right),$$

and includes all terms which could contribute 1% to the rate, and where the primed variables refer to Mars, and the unprimed to Phobos. The curious result is that higher harmonic tidal distortions contribute (Redman and Fish, 1964), because Phobos is relatively close to Mars ( $a = 9378.5$  km and  $M = 1.073 \pm 0.0074 \times 10^{16}$  kg). The phase shift  $\delta_{jmp0}$  corresponds to the tidal frequency ( $j - 2p$ )  $n - m\Omega' = m(n - \Omega')$ . Since Phobos' mean motion is  $1128.8^\circ/\text{day}$ , the solar semi-diurnal period is larger than any of the tidal periods associated with Phobos' orbit contraction. Only for Earth and Moon do we have some information that constrains the phase shift with tidal frequency (e.g. Lambeck, 1980; Williams and Boggs, 2009), from which we deduce that the dependence on frequency is weak. For simplicity, we shall adopt that the phase shifts are all equal. The higher harmonic Love numbers can be estimated from the approximation  $k_3 \approx 0.31k_2$  and  $k_4 \approx 0.14k_2$ , and these terms augment the tidal rate by 6.1%. We then find  $k_2 \sin \delta_{22} = (1.73 \pm 0.01) \times 10^{-3}$ . From Table 4, we can estimate that the true Love number at semi-diurnal tidal frequency is

$$k_2 = 0.164 \pm 0.009$$

if we adopt the observed MGS  $k_2$  estimate and correct for solid friction and atmospheric tides. The  $Q$  factor is

$$Q = 1 / \sin \delta_{22} = 109 \pm 6$$

for this  $k_2$  value.

Our knowledge of internal structure of Earth comes from seismic waves and normal modes with frequencies ranging from 10 Hz to 54 min. There is an anelastic softening of the Earth as perturbing frequency reduces, and a reasonable correction for  $k_2$  is  $3k_2/Q \approx 0.005$ . Thus, the ‘seismic’ Love number that should be compared with model estimates is  $k_2 = 0.159 \pm 0.009$ .

The precession rate is related to polar moment of  $C$  by

$$\frac{d\psi}{dt} = \dot{\psi}_o (0.3650 MR_e^2 / C) \text{ mas/year} + \dot{\psi}_g + \dot{\psi}_p,$$

$$\dot{\psi}_o = -\frac{3}{2} \frac{n_o^2}{0.365\Omega} (1 - e_{Mars}^2)^{-3/2} J_2 \cos \varepsilon_{Mars} = -7587.4 \text{ mas/year}.$$

The first term is caused by the solar torque on Mars oblate shape (represented by the unnormalized gravitational coefficient  $J_2 = 0.001956683$ ). In calculating  $\dot{\psi}_o$ , we use Mars orbit eccentricity  $e_{Mars} = 0.09341$ , obliquity  $\varepsilon_{Mars} = 25.189^\circ$ , mean motion  $n_o = \sqrt{GM_{Sun}/a_{Mars}^3} = 191.408^\circ/\text{day}$  and spin rate  $\Omega = 350.892^\circ/\text{day}$ . The above  $\dot{\psi}_o$  value differs from Yoder and Standish (1997) because of a change in the adopted  $R_e$  and also other numerical errors. The contribution  $\dot{\psi}_g = +6.7$  mas/year is a relativistic effect called geodetic precession (e.g. Reasenberg and King, 1979a), while  $\dot{\psi}_p = -0.2$  mas/year is caused by other planets (primarily Jupiter). Our best estimate for precession  $\dot{\psi} = -7594 \pm 10$  mas/year (see next section and Table 6) is very close to the value obtained by Yoder et al. (2003), except that the uncertainty is reduced by a factor of 2.5. The inferred moment is

$$C/MR_e^2 = 0.3644 \pm 0.0005$$

and is smaller than in Yoder et al. (2003) because of the changes in  $R_e$  and  $\dot{\psi}_o$ . The mean moment of inertia  $I = (A + B + C)/3$  can be related to  $J_2$ , the adopted reference radius  $R_e = 3396$  km and the mean radius  $R_0 = 3389.5$  km as

$$I/MR_0^2 = \left( C/MR_e^2 - \frac{2}{3} J_2 \right) \frac{R_e^2}{R_0^2} \cong C/MR_e^2 + 0.00009.$$

Thus, for these particular parameters, they are almost identical.

It is also plausible that the above mean moment should be reduced still further to account for the ‘Tharsis volcanic construct’ (Sohl et al., 2005). Based on Reasenberg’s argument (1977) (also see Yoder and Standish, 1997), the non-hydrostatic contributions to both moment  $C$  and  $B$  can be estimated assuming  $\Delta C = \Delta B$  while  $\Delta A = 0$  since Tharsis lies near the equator and is nearly aligned with the  $x$ -axis in the principle axis frame of reference. Now

$$(\Delta B - \Delta A)/MR^2 = 4\sqrt{C_{22}^2 + S_{22}^2} = 2.52 \times 10^{-4},$$

and the above estimate for the mean moment should be reduced by 2/3 of this amount or 0.00017. We can use the same argument to derive an equivalent hydrostatic  $J_2 = 0.001831$ , and from the Clair

**Table 6**  
Mars precession solutions.

Spacecraft	Precession solution (mas/year)	Notes
All data	$-7594 \pm 10$	Best solution this paper
MGS + MPF + VK	$-7584 \pm 25$	
ODY + MPF + VK	$-7599 \pm 15$	
MRO + MPF + VK	$-7606 \pm 24$	
<i>Previous determinations</i>		
MPF + VK	$-7576 \pm 35$	Folkner et al. (1997)
ODY + MPF + VK	$-7582 \pm 17$	Konopliv et al. (2006)
MGS + MPF + VK	$-7597 \pm 25$	Yoder et al. (2003)

raut formula derive the moment of inertia  $C/MR_e^2 = 0.3652$ , accurate to  $O(J_2)$ . This value agrees with our result within errors.

The mass and mean moment are two constraints employed when constructing interior structure models when no seismic profiles are available. We shall consider simple models in which just three parameters constrain Mars structure: (1) crustal thickness  $h_{cr}$  (with fixed density  $2.90 \text{ gm/cm}^3$ ), (2) mantle composition by the molar fraction  $\chi_M = \text{Mg}/(\text{Mg} + \text{Fe})$ , and (3) temperature profile offset (represented by  $\Delta T$ ) relative to an Earth-like profile (Yoder and Standish, 1997). The core is constructed assuming a Fe, FeS mixture defined by molar fraction  $\chi_c = \text{FeS}/(\text{FeS} + \text{Fe})$ . The Love number is particularly valuable in that it depends primarily on core size and mantle mean rigidity. An exploration of a variety of plausible structural models that satisfy  $k_2 = 0.159 \pm 0.009$  infer that core radius bounds are about  $1630 \text{ km} \leq R_f \leq 1830 \text{ km}$  (see Figs. 26 and 27). The new moment of inertia estimate restricts core radius for any given model to less than about 100 km, but is less useful in limiting the allowed models and the mean core radius. The mean core densities for these three models are displayed in Fig. 26c. The overall limit imposed on core density is about  $6.3\text{--}6.8 \text{ gm/cm}^3$ , where the lower density corresponds to the larger core. The corresponding constraint of core composition is  $0.28 \leq \chi_c \leq 0.60$  where the smaller number corresponds to the smaller, denser core. Clearly the core is substantially diluted with some light element if our  $k_2$  estimate is reliable.

Models that fix thermal profile and crustal thickness and then let  $\chi_M$  vary, predict that the moment of inertia is about 14 times more sensitive to core radius than is Love number. For example, if we fix  $\Delta T = -200\text{K}$  and crustal thickness to 50 km (cf. Zuber et al., 2000; Nimmo, 2002; Wicczorek and Zuber, 2004), then the allowed range in  $\chi_M$  which satisfies both constraints is only about 84–86%. The bounds on core size can be deduced from the intersection of the bounds separately imposed by  $k_2$  and moment of inertia constraints. For example, the allowed range for core radius from the moment constraint for  $\chi_M = 84\%$  is  $1582 \text{ km} < R_f < 1692 \text{ km}$  while the constraint imposed from the  $k_2$  bound is  $1680 \text{ km} < R_f < 1774 \text{ km}$ . Thus the allowed range from the combined constraints is  $1680 \text{ km} < R_f < 1692 \text{ km}$ , assuming the above fixed mantle density and temperature and crustal thickness values. We can map the allowed radius versus  $\chi_M$  for three different groups of models with distinct values of crustal thickness and thermal profile, as illustrated in Fig. 27. It happens that decreasing  $\chi_M$  by 1% increases  $C/MR^2$  by 0.001, if we fix core radius and the other parameters. This can be countered by increasing either crustal thickness or thermal profile or both. Increasing  $h_{cr}$  by 25 km changes  $C/MR^2$  by  $-0.0017$ . Increasing thermal  $\Delta T$  by 200 K changes  $C/MR^2$  by  $-0.0033$ . Clearly, phase-space in  $\{R_f, \chi_M\}$  that is available with each group is quite narrow (about 100 km in  $R_f$  core radius and 2% in  $\chi_M$ ). Still, the uncertainty in crustal thickness and thermal profile results in a much wider uncertainty in these two parameters. Turcotte et al. (2002) estimates crustal thickness of  $92 \pm 5$  km, Konopliv et al. (2006) find the mean thickness of  $72 \pm 18$  km while Neumann et al. (2004) estimate it to be  $45 \pm 5$  km.

Incidentally, Khan and Connolly (2008) find that the preferred core size is about 1680 km (core density of 6.7 gm and 22–25% sulfur) for a mean moment of 0.3635 and crustal thickness of 50 km (crustal density of  $3.0 \text{ gm/cm}^3$ ) The corresponding  $k_2$  Love number is about  $k_2 = 0.145$ . The core fraction of sulfur is 20–22%.

## 8. Mars orientation

The orientation model of Mars (Konopliv et al., 2006) for the gravity field development includes precession, nutation, and seasonal spin variations. Since the gravity solution is a joint solution

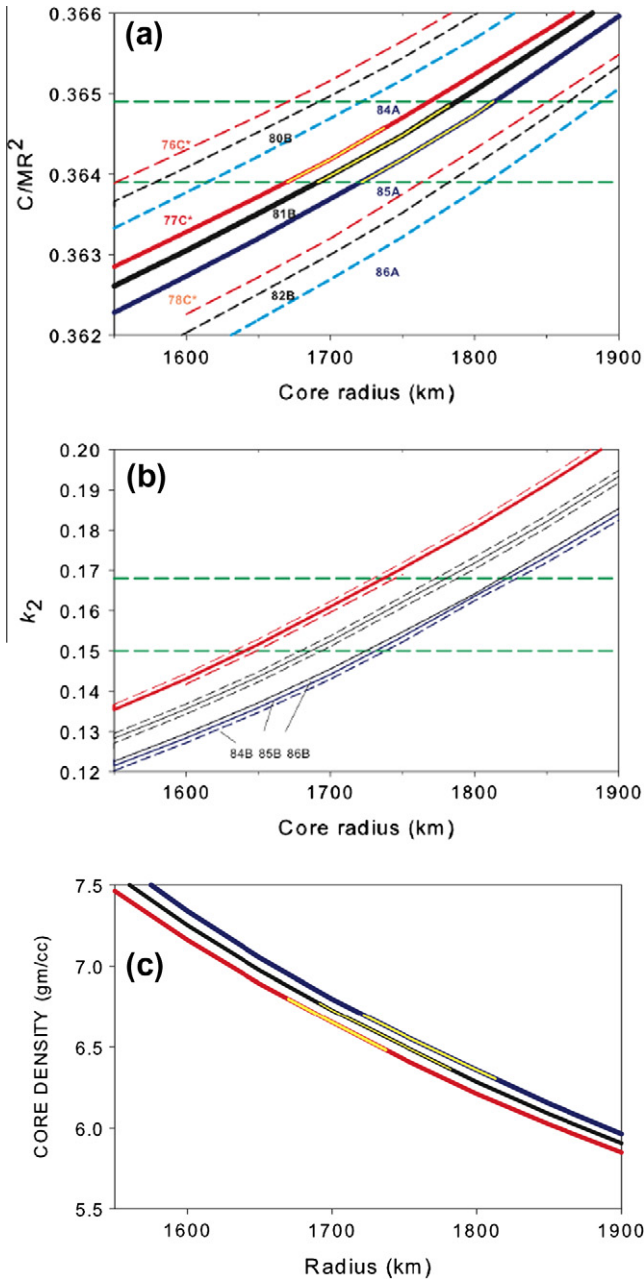


**Fig. 26.** Moment of inertia (a) and Love number  $k_2$  (b) shown together with several constructed interior model to infer core radius (Yoder and Standish, 1997). Three different model groups are shown which fix crustal thickness and thermal profile to A)  $h_{cr} = 50$  km,  $\Delta T = -200$  K (blue, e.g. 84A, 85A, 86A), B)  $h_{cr} = 75$  km,  $\Delta T = 0$  K (black) and C)  $h_{cr} = 100$  km,  $\Delta T = 200$  K (red). The allowed molar  $\chi_M$  for each case is limited to a band of 2% with midpoint 85%, 81% and 77%, respectively. The yellow insert for these midpoint  $\chi_M$  indicate the range in core radius that satisfy both moment and  $k_2$  constraints. Panel (c) displays the mean core density for the central line in each model, together with constraints on core density.

of gravity, Mars orientation and other parameters, a new set of orientation parameters should be used when the gravity field is used for dynamical propagation of spacecraft orbits. The orientation parameter values for the MRO110B gravity field are given in Table 5 where uncertainties are 15 times the formal error. The changes in parameter values versus the MGS95J solution are within the uncertainties, and uncertainties in the pole, precession, and spin rate have improved by 25–50%. The surface location of the spin pole and prime meridian changes by only a few meters versus previous results (see Fig. 28).

The Mars precession solution is predominately determined by the Mars Pathfinder (MPF) and Viking lander Doppler data. Although not as sensitive to the Mars orientation parameters as the lander data, the sheer volume of Mars orbiter tracking data has improved the Mars spin and pole orientation, mostly by extending the time span for which precession can be observed (1976–1997 to 1976–2008). Using MRO110B as the nominal gravity field, multiple precession solutions were determined under various assumptions and data sets. The best solution is given by the combination of all data sets as given in Table 6. The uncertainties are 15 times the formal error. Since the Mars Odyssey precession solution is not sensitive to atmospheric dust effects on the solar pressure model, Mars Odyssey data can be included in the solution without introducing systematic errors.

The solutions for the seasonal spin for each spacecraft data set alone and the combined solution of all data sets are given in Table 7. The seasonal spin solutions show better consistency as compared to previous results (Konopliv et al., 2006), and an improved uncertainty of about 30%.

Seasonal changes in solid body rotation are primarily driven by surface climate and involve an exchange of mass and/or momentum between the atmosphere and the solid body. These processes conserve total angular momentum  $C\omega$  such that  $\delta C/C = -\delta\omega/\omega$ . Differential changes in cap mass at the north and south hemispheres result in changes polar moment. If there is a fluid core, then only the mass of the mantle moment and atmosphere participate in this exchange. Since total mass is conserved, we can relate the change of the unnormalized second harmonic  $J_2$  to the change in polar moment  $C$ :  $\delta C = (2/3)\delta J_2 MR^2$ . This mass redistribution involves a second harmonic load, so we have to add a load factor  $1 + k'_{2M}$  when estimating this mass contribution from the models. The mantle load Love number  $k'_{2M}$  accounts for just mantle deformation, not fluid core deformation (see Table 3b). If we calculate the individual contributions to  $J_2$ , we find that the ice component dominates, while the pressure component depends on surface topography. Solar tides cause similar changes in rotation but are considerably smaller than the cap effect (Yoder and Standish, 1997). The zonal component of the surface wind velocity (east (+)-west (-) winds having constant latitude)  $v_{air}(h, \theta, \phi, t)$  depend locally on height  $h$  above the surface, colatitude  $\theta$ , and longitude  $\phi$ ,

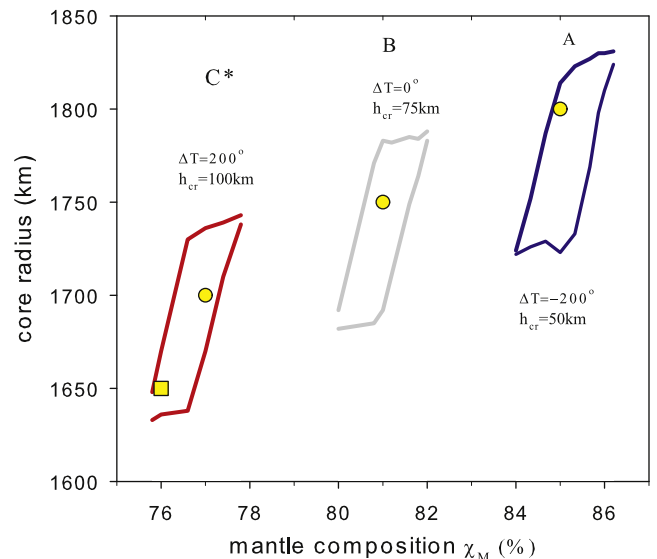


**Fig. 27.** Ranges in mantle composition  $\chi_M$  and core radius consistent with the three model groups described in Fig. 26. Yellow dots show solutions that have nearly the same Love number (A: 0.1636, B: 0.1622 and C: 0.1610) and Moment of inertia (A: 0.3642, B: 0.3645 and C: 0.3642), but very different core radii and mantle  $\chi_M$ .

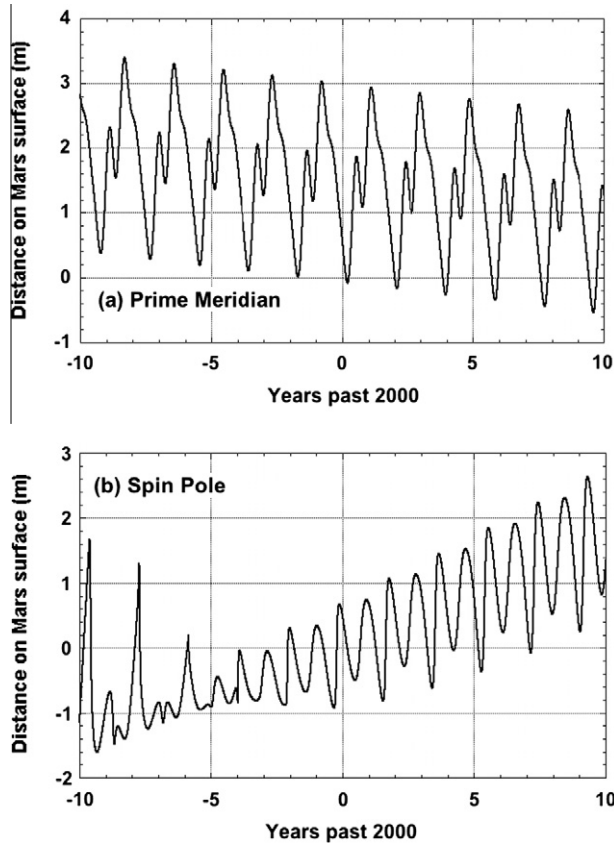


Fig. 28. Difference of the Mars (a) prime meridian and (b) spin pole for the MGS95J and MRO110B gravity solutions.

and may vary with time. Although driven by solar heating, this global average conserves angular momentum. Thus the response of the mantle is

$$C\delta\omega = - \int R^3 dh \int \sin^2 \theta d\theta d\phi \rho_{\text{air}}(h, \theta, \phi, t) v_{\text{air}}(h, \theta, \phi, t).$$

Variations in spin can be converted to changes in length-of-day (LOD) using:  $\delta\text{LOD}/\text{LOD} = -\delta\omega/\omega$ . GCM's (Sanchez et al., 2003) can be employed to calculate the separate contributions from ice caps, air pressure and winds to total angular momentum budget. The wind contribution from the LMD and AMES GCM are (unit is milli-second (ms) of time)

$$\delta\text{LOD}_{\text{AMES}} = 0.0565 \sin M + 0.1093 \cos M - 0.1265 \sin 2M - 0.0732 \cos 2M,$$

$$\delta\text{LOD}_{\text{LMD}} = 0.0277 \sin M + 0.0762 \cos M - 0.0784 \sin 2M - 0.0772 \times \cos 2M.$$

The wind component is about 30% of the total signature. The annual and semi-annual signatures have about the same amplitude. This is contrary to an earlier study that found that the wind component is primarily semi-annual (Van den Acher et al., 2002). Also, AMES GCM predicts zonal winds that are about 30% larger than the LMD GCM. This also holds true for the mass component and total amplitude.

Total  $\delta\text{LOD}$  deduced from AMES and LMD GCM are in good agreement with the previous studies that used earlier versions of the same GCM. The  $\delta\text{LOD}$  annual and semi-annual amplitudes of Sanchez et al. (2003) based on sum of axial atmospheric angular momentum and cap's inertia (see Fig. 14 of Sanchez et al. (2003))

Table 7

Mars seasonal spin amplitudes from the MRO110B gravity solution in mas for  $\cos j\ell'$ ,  $\sin j\ell'$ , and relativistic corrections on  $\sin j\ell'$ , where  $\ell'$  is the Mars mean anomaly. The uncertainties given are 10 times the formal error. Note that the orbiter only solutions (MGS, Odyssey, and MRO) do not include any lander data.

Data set	$j$	$\phi_{cj}$	$\phi_{sj}$	$\phi_{rj}$
All (MRO110B)	1	$435 \pm 23$	$-168 \pm 26$	$-176$
	2	$-97 \pm 22$	$-119 \pm 21$	$-8$
	3	$-17 \pm 18$	$-17 \pm 19$	$-1$
	4	$-9 \pm 16$	$-4 \pm 16$	
MGS only	1	$454 \pm 60$	$-194 \pm 67$	$-176$
	2	$-145 \pm 55$	$-170 \pm 56$	$-8$
	3	$2 \pm 57$	$1 \pm 49$	$-1$
	4	$-18 \pm 50$	$-2 \pm 53$	
Odyssey only	1	$486 \pm 40$	$-170 \pm 43$	$-176$
	2	$-134 \pm 37$	$-154 \pm 36$	$-8$
	3	$4 \pm 36$	$-15 \pm 36$	$-1$
	4	$4 \pm 32$	$-47 \pm 32$	
MRO only	1	$466 \pm 173$	$-191 \pm 149$	$-176$
	2	$-124 \pm 136$	$-3 \pm 140$	$-8$
	3	$-128 \pm 123$	$-66 \pm 123$	$-1$
	4	$-36 \pm 96$	$-65 \pm 101$	
MPF + Viking lander	1	$425 \pm 66$	$-171 \pm 96$	$-176$
	2	$-66 \pm 61$	$-92 \pm 68$	$-8$
	3	$-63 \pm 68$	$25 \pm 59$	$-1$
	4	$-31 \pm 43$	$-25 \pm 46$	

are very close to those deduced from the current AMES GCM run which simulates more closely the Viking lander pressure variations (Haberle et al., 2008). The load factor and the liquid core neglected in Sanchez et al. (2003) have a combined effect of less than few percent (Karatekin et al., 2006). Similarly the  $\delta\text{LOD}$  amplitudes reported by Defraigne et al. (2000) and Van den Acher et al., 2002 using earlier LMD GCM simulations, are in line with the present LMD GCM solutions except the large semi-annual component given by Defraigne et al. (2000).

Although we can detect seasonal  $J_2$  changes (see Fig. 24) from spacecraft, their accuracy is limited. Tracking of surface landers and orbiting spacecraft have detected changes in rotation angle (Table 7) and these can be converted to angular rate by taking the time derivative:  $d\delta\phi/dt = \delta\omega$ . The best global Doppler is supposedly accurate to about 5%. One year of X-band Doppler tracking of a lander (say, from MER Spirit once it cannot move) should improve the Viking plus Pathfinder solution for LOD by a factor of 10 or more. We can compare the observed rate with model calculations to see how well each match as shown in Fig. 29. The LMD model appears to be a slightly better match for the observed signal. Different assumptions for the dust content of the atmosphere changes the LMD solution by about 15% for  $0 < L_s < 250^\circ$  and up to 30–50% for  $L_s > 250^\circ$ .

## 9. Mars ephemeris and dynamical parameters

Range measurements to spacecraft orbiting Mars and to landers on Mars are a key component in the estimation of current planetary ephemerides. The Mars ranging data provide meter-level measurements relating the orbits of Earth and Mars. The orbits of the other planets and the Moon are primarily determined by other measurements. For the purposes of this paper, the Mars ranging data were used to estimate the orbital elements of Mars and the Earth–Moon barycenter along with other dynamical parameters affecting those elements and best determined by the Mars ranging data. These include the mass parameter of the Sun, the Earth/Moon mass ratio, and the mass parameters of a selected set of asteroids. Additional parameters were estimated to test for possible departure from the standard theory of general relativity. The orbital

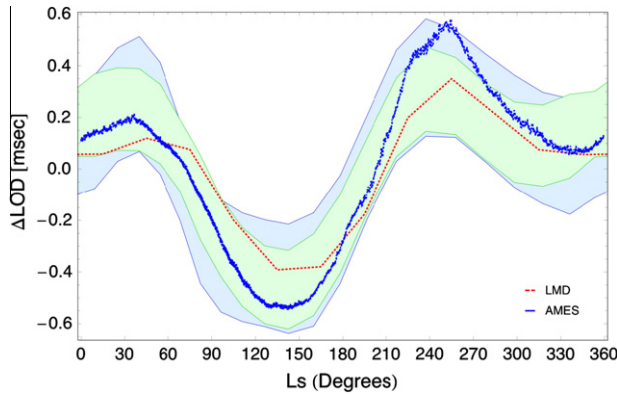


**Fig. 29.** LOD estimates from both LMD and AMES GCM maps are shown with a range of estimates derived from observed rotation signal as shown in Table 7 (blue region) as well as the previous estimate of Konopliv et al., 2006 (green region). The short period changes seen in the AMES model are due to the diurnal and semi-diurnal solar tide.

elements of the Moon and other planets were fixed at values estimated previously for the planetary ephemeris DE421 (Folkner et al., 2009). The data used include the Viking lander ranging from 1976 to 1983, Mars Pathfinder ranging data from 1997, and ranging to the MGS, Odyssey, and MRO orbiters through July, 2009, which is about 18 months more data than in the DE421 fit. Post-fit residuals for the Mars orbiter range data are shown in Fig. 30, and this set of data was used to generate planetary ephemerides DE422 and DE423.

In fitting the Mars range data to the planetary ephemerides, the positions of the planets and Moon were numerically integrated using the Einstein–Infeld–Hoffman equations of motion (Einstein et al., 1938; Moyer, 2000). The coordinate time used agrees with the recently adopted definition for TDB coordinate time and all dimensioned results below are compatible with that time scale (Standish, 1998; IAU resolution 3, General Assembly 24, 2006). The mass parameters for the planets other than Earth are determined by spacecraft encounters. The sum of the mass parameters for the Earth and Moon are determined from lunar laser ranging data. The range from Earth tracking stations to Mars orbiters and landers was measured based on the round-trip light-time and compared to the values calculated according to the formalism by Moyer (2000). In addition the locations of Viking lander 1, Viking lander 2, and Mars Pathfinder on Mars, an instrumental bias and a correction to the solar plasma delay model (Standish, 1990) for each lander and orbiter were estimated, the latter correction accounting for the different radio frequency channels used for each spacecraft. The complete parameter list is given in Table 8.

## 10. Asteroid perturbations on the Mars orbit

The orbit of Mars is affected at the meter-level by several hundred asteroids (Williams, 1984, private communication, 2005; Kuchynka et al., 2009). With the increased time span of Mars ranging data, the mass parameters of more asteroids, which affect the Mars orbit, can be usefully estimated. However, the range data are not accurate and extensive enough to estimate the mass parameters for all asteroids that cause meter-level perturbations on the Mars orbit. So the estimated asteroid mass parameters and other parameters of the planetary ephemerides, and their uncertainties, depend on the selection of which asteroid GMs to estimate and the treatment of the uncertainties of the asteroid mass parameters that cannot be accurately estimated from the range data.

For this paper we used Mars ranging data to estimate the mass parameters of the 19 asteroids which cause short-term perturba-

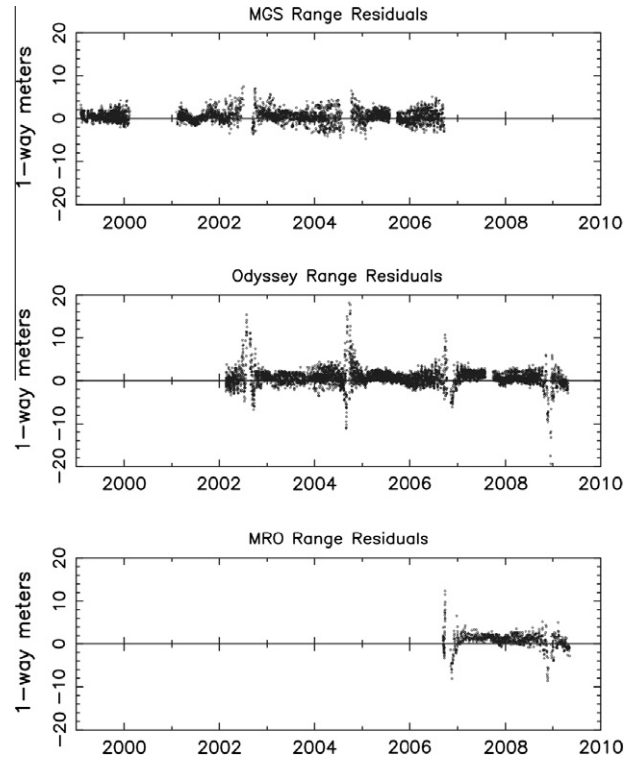


**Fig. 30.** Earth–Mars ranging data residuals from MGS, Mars Odyssey, and MRO.

tions of the Earth–Mars range in excess of 5-m root-mean-square amplitude over the time span of the modern Mars spacecraft range data (1999–2010). The short-term signature was computed by comparing the orbits of the planets with the individual asteroid mass parameter at its nominal value with integration with individual asteroid mass parameters set to zero. From this difference a long-term signature was removed by estimating a correction to the Earth and Mars orbital elements, after which the root-mean-square amplitude was computed to give the amplitude of the short-term signature. Mass parameters for two other asteroids with the largest correlations with the 19 most significant asteroids were also estimated. A different set of 34 perturbing asteroids was selected by Fiennga et al. (2009a) based on overall amplitude of effect on the Mars orbit rather than the short-term signature used here. The long-term signatures are subject to higher correlations, which can cause negative or near-zero densities for some asteroids to appear in the estimated values.

The effects of the 46 asteroids with effects on the Mars orbit of more than 1 m and less than 5 m root-mean-square amplitude over 1999–2010 were included with nominal orbits and mass parameters held fixed, but with uncertainties in their mass parameters included in the uncertainties of estimated parameters through the use of consider analysis (Bierman, 1977). The uncertainties in this set of asteroid mass parameters was assumed to be 50% of the nominal value, and folded into the final uncertainty estimates. The 67 estimated and considered asteroids are the same as those estimated by Konopliv et al. (2006). Finally, the 276 next most significant asteroids, in terms of influence on the orbit of Mars, were divided into three classes and the densities of each class estimated based on nominal diameters from IRAS observations (Matson et al., 1986). Our uncertainties are larger than the formal uncertainties in which asteroid mass parameters that are not estimated are essentially treated as perfectly known (e.g. Fiennga et al., 2009a; Pitjeva, 2005). We have found that the parameter uncertainties computed using this consider analysis approach

**Table 8**  
Solar System parameters fit to Mars range data, including the initial position and velocity of Mars and the Earth–Moon barycenter (equivalent to orbital elements), the mass parameter of the Sun and its rate of change, the first solar zonal gravity harmonic, the ratio of the mass of the Earth to the mass of the Moon, the density of three asteroid classes (carbonaceous, silicate, metallic), PPN parameters  $\gamma_{PPN}$  and  $\beta_{PPN}$ , constant radial accelerations of the Mars and the Earth–Moon barycenter, the magnitude  $\alpha$  of the Yukawa potential as a function of length scale  $\lambda$ , the mass parameters of 67 individual asteroids, the locations of Viking lander 1, Viking lander 2, and Mars Pathfinder on Mars, an instrumental bias and a correction to the solar plasma delay model for each lander and orbiter.

Orbital elements	Gravity parameters	Estimated asteroid GMs	Considered asteroid GMs	Considered asteroid GMs	Other parameters
$x(t_0)_{emb}$	$GM_{Sun}$	1 Ceres	5 Astraea (S)	98 Ianche (C)	XYZ <sub>Vik1</sub>
$y(t_0)_{emb}$	$d(GM_{Sun})/dt$	2 Pallas	11 Parthenope (S)	105 Artemis (C)	bia <sub>S<sub>Vik1</sub></sub>
$z(t_0)_{emb}$	$J_{2Sun}$	3 Juno	13 Egeria (C)	111 Ate (C)	cor <sub>Vik1</sub>
$\dot{x}(t_0)_{emb}$	$M_{Earth}/M_{Moon}$	4 Vesta	18 Melpomene (S)	135 Hertha (M)	XYZ <sub>Vik2</sub>
$\dot{y}(t_0)_{emb}$	$\rho(c)$	6 Hebe	20 Massalia (S)	139 Juewa (C)	bia <sub>S<sub>Vik2</sub></sub>
$\dot{z}(t_0)_{emb}$	$\rho(s)$	7 Iris	21 Lutetia (M)	145 Adeona (C)	cor <sub>Vik2</sub>
$x(t_0)_{Mars}$	$\rho(m)$	8 Flora	22 Kalliope (M)	187 Lambertia (C)	XYZ <sub>MPF</sub>
$y(t_0)_{Mars}$	$\gamma_{PPN}$	9 Metis	24 Themis (C)	192 Nausikaa (S)	bia <sub>S<sub>MPF</sub></sub>
$z(t_0)_{Mars}$	$\beta_{PPN}$	10 Hygiea	25 Phocaea (S)	194 Prokne (C)	cor <sub>MPF</sub>
$\dot{x}(t_0)_{Mars}$	$a_{r,emb}$	14 Irene	27 Euterpe (S)	216 Kleopatra (M)	bia <sub>S<sub>MGS</sub></sub>
$y(t_0)_{Mars}$	$a_{r,Mars}$	15 Eunomia	28 Bellona (S)	230 Athamantis (S)	cor <sub>MGS</sub>
$z(t_0)_{Mars}$	$\alpha(\lambda)$	16 Psyche	30 Urania (S)	337 Devosa (M)	bia <sub>S<sub>ODY</sub></sub>
		19 Fortuna	31 Euphrosyne (C)	344 Desiderata (C)	cor <sub>ODY</sub>
		23 Thalia	42 Isis (S)	354 Eleonora (S)	bia <sub>S<sub>MRO</sub></sub>
		29 Amphitrite	45 Eugenia (C)	372 Palma (C)	cor <sub>MRO</sub>
		41 Daphne	51 Nemausa (C)	405 Thia (C)	
		52 Europa	60 Echo (S)	409 Aspasia (C)	
		324 Bamberga	63 Ausonia (S)	419 Aurelia (C)	
		511 Davida	65 Cybele (C)	451 Patientia (C)	
		532 Herculina	69 Hesperia (M)	488 Kreusa (C)	
		704 Interamnia	78 Diana (C)	554 Peraga (C)	
			94 Aurora (C)	654 Zelinda (C)	

compare reasonably well to differences in estimated values under a variety of different modeling assumptions.

The estimated mass parameters and uncertainties for the 21 asteroids selected as described above are given in Table 9. For comparison, independent estimates from analysis of astrometric observations of asteroid mutual encounters from Baer et al. (2008) are also shown for 16 of the 21 asteroids. Our estimates and those from Baer et al. agree within uncertainties with the exception of 08 Flora, 14 Irene, 19 Fortuna, and 511 Davida. The densities based on our estimated mass parameters for these four asteroids, and for 23 Thalia, 41 Daphne, and 532 Herculina not estimated by Baer et al. (2008), are plausible for the given asteroid class. Our uncertainties are generally much higher than those of Baer et al. (2008) and those of other estimates based on Mars ranging data

(e.g. Fienga et al., 2009a; Pitjeva, 2005) due to our use of consider analysis to account for the uncertainty in 46 individual asteroids mass parameters. (The Baer et al. (2008) uncertainties quoted are formal uncertainties not accounting for possible systematic effects.) Of the 21 asteroid mass parameters, the highest correlation is 0.7 between Vesta and Thalia.

The determination of the mass of Vesta from another independent data set also benefits from the Mars range data. From the perturbation due to Vesta on the orbit of Eros and using range data to the NEAR spacecraft, the mass of Vesta was previously determined to be  $18.2 \pm 0.2 \text{ km}^3/\text{s}^2$  (Konopliv et al., 2002). However, errors are introduced in the Vesta mass estimate through mismodeling of any other perturbers on the Eros orbit such as Mars. The previous NEAR study used the older planetary ephemeris DE403, which did not

**Table 9**  
Asteroid mass estimates from the Mars ranging data. The independent astrometry estimates are from Baer et al. (2008). The Vesta NEAR mass estimate uses an improved Mars ephemeris and is an update of Konopliv et al. (2002).

Asteroid	Type	Estimated GM ( $\text{km}^3/\text{s}^2$ )	Estimated GM ( $10^{-12}M_{\odot}$ )	Est. $\rho$ ( $\text{g}/\text{cm}^3$ )	Astrometry GM ( $10^{-12}M_{\odot}$ )	Ast. $\rho$ ( $\text{g}/\text{cm}^3$ )	Amp (m)
1 Ceres	G	$62.10 \pm 0.43$	$467.90 \pm 3.25$	2.06	$475.50 \pm 0.80$	2.09	279.1
2 Pallas	B	$13.73 \pm 0.34$	$103.44 \pm 2.55$	2.62	$106.00 \pm 4.00$	2.69	94.9
3 Juno	S	$1.61 \pm 0.12$	$12.10 \pm 0.91$	2.69	$13.40 \pm 2.30$	2.98	26.2
4 Vesta	V	$17.38 \pm 0.27$	$130.97 \pm 2.06$	3.36	$131.90 \pm 0.30$	3.38	210.4
NEAR est.		$17.66 \pm 0.2$	$133.07 \pm 1.51$	3.41			
6 Hebe	S	$0.89 \pm 0.22$	$6.73 \pm 1.64$	3.97	$6.46 \pm 0.32$	3.81	9.1
7 Iris	S	$0.73 \pm 0.18$	$5.53 \pm 1.32$	2.19	$6.86 \pm 0.50$	2.72	36.2
8 Flora	S	$0.27 \pm 0.06$	$2.01 \pm 0.42$	1.84	$4.26 \pm 0.45$	3.89	8.6
9 Metis	S	$0.44 \pm 0.14$	$3.28 \pm 1.08$	2.37	$5.70 \pm 1.40$	4.12	9.4
10 Hygiea	C	$5.97 \pm 1.03$	$44.97 \pm 7.76$	2.14	$44.50 \pm 0.70$	2.12	16.6
14 Irene	S	$0.25 \pm 0.11$	$1.91 \pm 0.81$	2.04	$4.13 \pm 0.73$	4.42	8.2
15 Eunomia	S	$1.88 \pm 0.20$	$14.18 \pm 1.49$	2.79	$15.70 \pm 0.20$	3.09	10.3
16 Psyche	M	$1.65 \pm 0.46$	$12.41 \pm 3.44$	7.32	$11.00 \pm 0.40$	6.49	6.6
19 Fortuna	G	$0.42 \pm 0.07$	$3.20 \pm 0.53$	1.35	$6.38 \pm 0.25$	2.70	12.9
23 Thalia	S	$0.15 \pm 0.09$	$1.11 \pm 0.71$	3.38			4.3
29 Amphitrite	S	$0.98 \pm 0.20$	$7.42 \pm 1.49$	2.96	$5.92 \pm 0.03$	2.36	11.9
41 Daphne	C	$0.56 \pm 0.23$	$4.24 \pm 1.77$	3.05			9.7
52 Europa	CF	$1.48 \pm 1.11$	$11.17 \pm 8.40$	1.54	$8.29 \pm 0.81$	1.14	6.4
324 Bamberga	CP	$0.71 \pm 0.13$	$5.34 \pm 0.99$	1.69			44.4
511 Davida	C	$1.14 \pm 0.79$	$8.58 \pm 5.93$	1.35	$22.00 \pm 1.00$	3.45	3.7
532 Herculina	S	$0.66 \pm 0.37$	$4.97 \pm 2.81$	1.72			10.8
704 Interamnia	F	$2.65 \pm 0.87$	$19.97 \pm 6.57$	2.38	$18.60 \pm 1.10$	2.22	8.5



include any Mars spacecraft range data except from the Viking landers. With the inclusion of Mars spacecraft data since 1997, the uncertainty of the Mars orbit has been improved by more than one order of magnitude. An updated estimate for the mass parameter of Vesta, with the only change being the new Mars ephemeris, is  $17.82 \pm 0.2 \text{ km}^3/\text{s}^2$ . With a new Vesta ephemeris that includes more observations and adds Ceres and Pallas as perturbers, and the addition of 67 asteroid perturbers to the Eros orbit (same asteroids as above and in Konopliv et al., 2006), the new Vesta mass is  $17.66 \pm 0.2 \text{ km}^3/\text{s}^2$ . The largest remaining error contribution is the uncertainty in the NEAR range transponder delay calibration. The current uncertainty represents a 4-m calibration error.

## 11. Solar System tests of gravity

Traditionally the solar mass parameter has a fixed value in units of  $(\text{AU})^3/(\text{day})^2$  and the value of the astronomical unit estimated. Here we have used the Mars spacecraft range data to explicitly determine the mass parameter of the Sun to be

$$GM_{\text{Sun}} = 132712440042 \pm 10 \text{ km}^3/\text{s}^2.$$

This corresponds to an *AU* estimate of

$$AU = 149597870700 \pm 3 \text{ m}.$$

The value is consistent with estimates reported by Fienga et al. (2009a) and by Pitjeva (2008) using much of the same data, though the former's uncertainty is 20 times smaller, possibly because effects of asteroids whose mass parameters were not estimated were not taken into account. The ratio of the mass of the Earth to the mass of the Moon was estimated to be

$$M_{\text{Earth}}/M_{\text{Moon}} = 81.3005694 \pm 0.0000015.$$

This is compatible with the estimate by Pitjeva (2008) though our uncertainty is smaller possibly because more Mars range data were included in our estimate. The estimate of Fienga et al. differs from ours by twice their uncertainty. A previous estimate with independent range data from the NEAR spacecraft in orbit about Eros (Konopliv et al., 2002,  $M_{\text{Earth}}/M_{\text{Moon}} = 81.300570 \pm 0.0000050$ ) is consistent with our estimate but not as accurate ( $\sim 3\times$  larger). Using the Earth *GM* values derived from satellite data (Ries et al., 1992), Lunar Laser Ranging values of  $M_{\text{Earth}} + M_{\text{Moon}}$  give  $81.300566 \pm 0.0000200$  (Konopliv et al., 1998) and the slightly improved  $81.300569 \pm 0.0000140$  (Williams et al., 2009). The solar first zonal gravity harmonic  $J_2$  was estimated also mainly to include its correlation with the parameter  $\beta$  discussed below. However the  $J_2$  is better estimated with Venus Express range data (Fienga et al., 2009a) so we use that value and uncertainty here.

Using the Mars ranging data to estimate a rate of change of the mass parameter of the Sun, we obtain

$$d(GM_{\text{Sun}})/dt * 1/GM_{\text{Sun}} = 0.1 \times 10^{-13}/\text{year} \pm 1.6 \times 10^{-13}/\text{year}.$$

Light emission from the Sun corresponds to a fractional rate of change of solar mass parameter of about  $0.7 \times 10^{-13}/\text{year}$ , while the fractional rate of change due to solar wind has been estimated as  $0.2 \times 10^{-13}/\text{year}$  (Withbroe and Noyes, 1977). Assuming mass loss due to other terms is smaller, our estimated of rate of change of solar mass parameter gives an upper bound on the rate of change on the gravitation constant *G*. A more accurate determination of rate of change of *G* would require modeling the known effects on rate of change of solar mass loss and their uncertainties. Our inferred rate of change of *G* is consistent with zero, as is an independent estimate with less accuracy from lunar laser ranging of  $4 \times 10^{-13}/\text{year} \pm 9 \times 10^{-13}/\text{year}$  (Williams et al., 2004).

To illustrate the effects of data and asteroid modeling on uncertainty in estimated parameters, we used three alternative strate-

gies for estimating the uncertainty to the fractional rate of change of the solar mass parameter. First, simply ignoring the effect of the uncertainties in the mass parameters for the 46 next most significant asteroids, our uncertainty in the fractional rate of change of the solar mass parameter would be  $3.7 \times 10^{-14}/\text{year}$ . Next, if we estimated only three asteroid mass parameters and densities for three classes for all other asteroids, our uncertainty would be  $8.8 \times 10^{-15}/\text{year}$ . Note that this uncertainty is comparable with the uncertainty reported by Pitjeva (2005), which implies that the actual mass loss terms for the Sun should have been detected if not taken into account. Finally, if we estimated only three asteroid mass parameters and densities for three classes for the remaining asteroids and treated each range measurement as independent rather than sharing a common calibration for each station tracking pass our uncertainty in the fractional rate of change of the solar mass parameter would be  $1.8 \times 10^{-15}/\text{year}$ . Our chosen strategy for estimating the uncertainty in the solar mass loss is thus more conservative than other strategies but gives agreement with our lack of ability to confidently see the actual solar mass loss terms.

Deviations of Solar System gravity can be explored using the parameterized post-Newtonian parameters  $\gamma_{\text{PPN}}$  and  $\beta_{\text{PPN}}$ . The largest observable effect on  $\gamma_{\text{PPN}}$  is the light-time delay for radio waves passing near the Sun (Shapiro, 1964). Because radio signal delay due to solar plasma is similar, estimation of the relativistic time delay is more accurate when multiple radio frequencies can be used calibrate the solar plasma effect. Multiple frequencies were also used on the Cassini spacecraft to estimate  $\gamma_{\text{PPN}}$  (Bertotti et al., 2003). Multiple radio frequencies from the Viking orbiter spacecraft were used to calibrate the range measurements to the Viking landers for solar conjunctions in 1976 and 1979. (Range measurements from Viking lander 1 were also acquired during a solar conjunction in 1982, however those data were calibrated for solar plasma which can no longer be assessed and so are not used here for estimation of the  $\gamma_{\text{PPN}}$ .) For the first Viking Lander conjunction the relativistic delay was used to estimate  $\gamma_{\text{PPN}}$  with uncertainty  $2 \times 10^{-3}$  (Reasenberg et al., 1979b). The modern spacecraft range data have better intrinsic measurement accuracy but lack multiple frequencies to calibrate solar plasma. This restricts useful measurements to larger angular separation from the Sun than for Viking but still improves the overall estimate. Using Viking lander data from conjunctions in both 1976 and 1979, Mars Odyssey data from conjunctions in 2002, 2004, 2006, and 2008, and MRO data from conjunction in 2008 we obtain

$$\gamma_{\text{PPN}} - 1 = 1.8 \times 10^{-4} \pm 2.6 \times 10^{-4}.$$

This uncertainty is based on our nominal treatment of the asteroid mass parameters described above. The accuracy of this determination is comparable with that determined by VLBI observations (Robertson and Carter, 1984; Robertson et al., 1991; Lebach et al., 1995; Shapiro et al., 2004; Lambert and Le Poncin-Lafitte, 2009) but not as accurate as the Cassini experiment that obtained an accuracy of  $2 \times 10^{-5}$  (Bertotti et al., 2003).

An estimate of the  $\beta_{\text{PPN}}$  can be derived from estimation of the precession of the perihelion of Mars, which is given by

$$\Delta\phi/\text{orbit} = (2 - \beta_{\text{PPN}} + 2\gamma_{\text{PPN}})6\pi M_{\text{Sun}}/[3a(1 - e^2)],$$

where *a* is the semi-major axis and *e* the eccentricity of the orbit of Mars. This term results in approximately  $1.35''/\text{century}$  in the precession of the perihelion which is observable with the Mars ranging data. Using the Mars ranging data and holding  $\gamma_{\text{PPN}}$  fixed to its value in general relativity based on the Cassini result, we estimate

$$\beta_{\text{PPN}} - 1 = 0.4 \times 10^{-4} \pm 2.4 \times 10^{-4}.$$

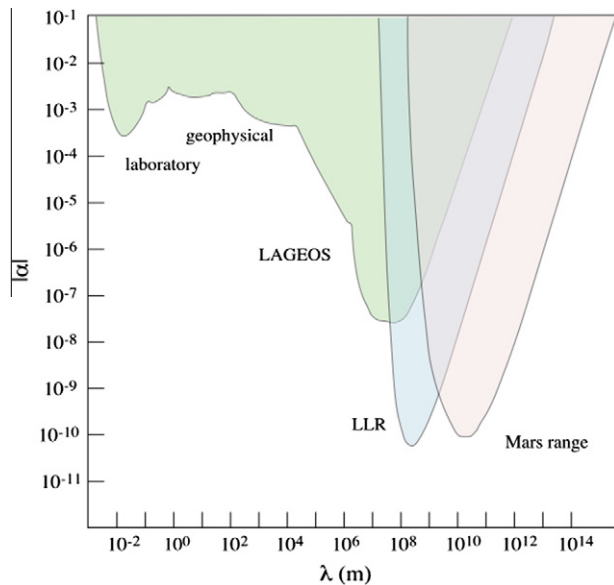


**Fig. 31.** Upper bounds on the Yukawa gravitational potential magnitude as a function of length scale. The shaded regions are excluded by various experiments, including this analysis for Mars spacecraft range data shaded in orange.

This is comparable with the estimate using Venus Express and Mars Express range data by [Fienga et al. \(2009b\)](#). From estimation of the ratio of inertial to gravitational mass of the Moon using lunar laser ranging data, [Williams et al. \(2004\)](#) get an estimate of  $\beta_{\text{PPN}}$  more accurate by a factor of 2.

The Mars range data can be used to set limits on the deviation of gravity from the Newtonian inverse-square law at Solar-System length scales. From the Mars ranging data we estimate an upper bound for an anomalous radial acceleration from the Sun as  $<3 \times 10^{-14} \text{ m/s}^2$  for the Earth–Moon barycenter and  $<8 \times 10^{-14} \text{ m/s}^2$  for Mars. These levels are several orders of magnitude lower than the anomalous acceleration on spacecraft reported by [Anderson et al. \(1998\)](#), who recognized that such an effect has been ruled out for the inner planets. Alternatively, the Mars ranging data can be used to estimate the amplitude of a modified gravitational potential in the Yukawa form of

$$\phi(r) = 1/r * [1 + \alpha e^{-r/\lambda}].$$

**Fig. 31** plots the estimated value of the dimensionless scale factor  $\alpha$  as a function of distance at the 95% confidence level. **Fig. 31** also shows estimates of  $\alpha$  at other length scales from other experiments as summarized by [Adelberger et al. \(2003\)](#). The shaded areas in the figure are excluded based on experiments including this analysis of Mars range data.

## 12. Conclusions

The global gravity field of Mars has been significantly improved using additional tracking data and model improvements. The recommended field is MRO110B2, since it has a looser constraint with less suppression of high frequency amplitudes. The lower altitude MRO tracking data is the main cause for the improved spherical harmonic gravity resolution of Mars from degree 70 (MGS95J) to degree 90. The near sectoral coefficients of the gravity field are better determined and their uses are a possible alternative for studies of features in an equatorial band of  $\pm 50^\circ$ . Other improvements such as thrust modeling on MGS and solar pressure modeling of atmospheric dust for Mars Odyssey have improved orbit determination

accuracy and resulted in consistent Love number determinations for all spacecraft.

Our best MGS  $k_2$  Love number solution is  $k_2 = 0.173 \pm 0.009$ . After correction for solid friction, atmospheric tides, and anelastic softening, we obtain  $k_2 = 0.159 \pm 0.009$ . With the improved precession solution ( $\dot{\psi} = -7594 \pm 10 \text{ mas/year}$ ) and polar moment ( $C/MR_c^2 = 0.3644 \pm 0.0005$ ) from additional years of orbiter tracking, the core radius is constrained to  $1630 \text{ km} \leq R_f \leq 1830 \text{ km}$  assuming a plausible range of internal models.

Time variations of the odd zonal gravity parameters and length-of-day solutions have been compared with predictions from two GCM models and two sets of Odyssey neutron spectrometer data detailing ice cap history. Orbiter LOD solutions data match well with GCM AMES and LMD predictions, with LMD being slightly better. The Odyssey NS data and LMD GCM model match best with observed seasonal gravity from MGS and Odyssey, while HEND and AMES GCM have about a factor of 2 larger residuals. The fit to the NS data is improved if we rescale its amplitude by a factor of 1.09 and this seems to be a plausible correction based on potential NS data error sources. We were unable to confirm inter-annual changes seen in 2 years of NS data for a complete Mars year. There is an intriguing signal in the doubly differenced  $\bar{J}_3$  data that cannot be explained. It is possible that atmospheric drag and AMD errors may contribute to MGS uncertainty in some subtle way that masks year to year changes.

With the increased time span of the data, Mars ranging data now allow for mass estimates of 21 asteroids, as compared to 5 asteroid mass estimates in previous results ([Konopliv et al., 2006](#)). Uncertainties in the mass estimates now account for uncertainties in other asteroid masses that are not estimated. Solutions mostly agree within uncertainties for results from independent data sets. The Mars ranging data also strongly determines the solar mass parameter ( $GM_{\text{Sun}} = 132712440042 \pm 10 \text{ km}^3/\text{s}^2$ ) and Earth–Moon mass ratio ( $M_{\text{Earth}}/M_{\text{Moon}} = 81.3005694 \pm 0.0000015$ ) and constrains mass loss of the Sun to be  $d(GM_{\text{Sun}})/dt * 1/GM_{\text{Sun}} = 0.1 \times 10^{-13}/\text{year} \pm 1.6 \times 10^{-13}/\text{year}$ . Variations of gravity models from general relativity are also constrained, although the PPN estimates are not as accurate as results from other spacecraft and LLR data.

Future MRO and Mars Odyssey spacecraft data will improve all aspects of the results discussed above, but only incrementally. Possible significant improvements in the Mars static gravity field are from lower altitude spacecraft or improved tracking accuracy such as Ka-band. Improvement of seasonal gravity detection most likely requires an onboard accelerometer together with improved tracking. Mars ranging accuracy of  $\sim 10$ -cm maybe possible with improved DSN station calibration. Although the Dawn mission will determine the masses of Vesta and Ceres, these constraints have a minimal effect on the separability of many asteroid perturbations, but may help estimates of asteroids that are strongly correlated such as Thalia.

## Acknowledgments

The research described in this paper was carried out at the Jet Propulsion Laboratory, California Institute of Technology, under contract with the National Aeronautics and Space Administration. OK acknowledges the support of Belgian PRODEX program managed by the ESA in collaboration with the BELSPO. Dolan Highsmith, Stuart Demcak, and Tung-Han You of the JPL navigation team provided spacecraft model information. Boris Semenov provided help with incorporating MRO attitude, solar array and HGA information. Alan Chamberlin provided the small body ephemerides necessary for the processing of the NEAR data. Bob Haberle, Jim Schaeffer, and Francois Forget provided data for the GCM models. Tom Prettyman provided maps and instruction for interpreting

Mars Odyssey NS data. We are grateful for the constructive reviews by Walter Kiefer and an anonymous reviewer.

## References

- Adelberger, E.G., Heckel, B.R., Nelson, A.E., 2003. Tests of the gravitational inverse-square law. *Annu. Rev. Nucl. Part. Sci.* 53, 77–121.
- Aharonson, O., Zuber, M.T., Smith, D.E., Neumann, G.A., Feldman, W.C., Prettyman, T.H., 2004. Depth, distribution and density of CO<sub>2</sub> deposition on Mars. *J. Geophys. Res.* 109, E05004. doi:10.1029/2003JE002223.
- Allison, M., 1997. Accurate analytic representations of solar time and seasons on Mars with application to the Pathfinder/Surveyor missions. *J. Geophys. Res.* 102, 1967–1970.
- Anderson, F.S., Grimm, R.E., 1998. Rift processes at the Valles Marineris: Constraints from gravity on necking and rate-dependent strength evolution. *J. Geophys. Res.* 103, 11113–11124.
- Anderson, J.D., Laing, P.A., Lau, E.L., Liu, A.S., Nieto, M.M., Turyshev, S.G., 1998. Indication, from Pioneer 10/11, Galileo, and Ulysses data, of an apparent anomalous, weak, long-range acceleration. *Phys. Rev. Lett.* 81, 2858–2861.
- Baer, J., Milani, A., Chesley, S.R., Matson, R.D., 2008. An observational error model, and application to asteroid mass determination. *Bull. Am. Astron. Soc.* 40, 493.
- Balmino, G., Marty, J.C., Duron, J., Karatekin, O., 2005. Mars long wavelength gravity field time variations: A new solution from MGS tracking. In: *Dynamic Planet, Proc. IAG Symposium*, Cairns, Australia. Springer, Berlin, doi:10.1007/978-3-540-49350-1.
- Belleguic, V., Lognonné, P., Wiczcerek, M., 2005. Constraints on the martian lithosphere from gravity and topography data. *J. Geophys. Res.* 110, E11005. doi:10.1029/2005JE002437.
- Bertotti, B., Iess, L., Tortora, P., 2003. A test of general relativity using radio links with the Cassini spacecraft. *Nature* 425, 374–376.
- Bierman, G.J., 1977. *Factorization Methods for Discrete Sequential Estimation*. Academic Press, New York.
- Bills, B.G., Neumann, G.A., Smith, D.E., Zuber, M.T., 2005. Improved estimate of tidal dissipation within Mars from MOLA observations of the shadow of Phobos. *J. Geophys. Res.* 110, E07004. doi:10.1029/2004JE002376.
- Christensen, P.C. et al., 2001. The Mars Global Surveyor Thermal Emission Spectrometer experiment: Investigation description and surface science results. *J. Geophys. Res.* 106, 23823–23871.
- Clancy, R.T., Wolf, M.J., Whitney, B.A., Smith, M.D., Cantor, B.A., 2008. High altitude dust global distribution, vertical mixing, and particle sizes during the 2001 planet-encircling dust storm. In: *3rd Int. Workshop: The Mars Atmosphere: Modeling and Observations*. Williamsburg, VA. 9084 pp.
- Defraigne, P., de Viron, O., Dehant, V., Van Hoolst, T., Hourdin, F., 2000. Mars rotation variations induced by atmosphere and ice caps. *J. Geophys. Res.* 105 (E10), 24563–24570. doi:10.1029/1999JE001227.
- Dorman, L.M., Lewis, B.T.R., 1970. Experimental isostasy. 1. Theory of the determination of the Earth's isostatic response to a concentrated load. *J. Geophys. Res.* 75 (17), 3357–3365.
- Eanes, R.J., Schutz, B., Tapley, B., 1983. Earth and ocean tide effects on Lageos and Starlette. In: Kuo, J.T. (Ed.), *Proc. 9th Int. Symp. on Earth Tides*. Schweizerbart'sche Verlagsbuchhandlung, Stuttgart, pp. 239–249.
- Einstein, A., Infeld, L., Hoffmann, B., 1938. The gravitational equations and the problem of motion. *Ann. Math.* 39, 65–100.
- Evans, A.J., Andrews-Hanna, J.C., Zuber, M.T., 2010. Geophysical limitations on the erosion history within Arabia Terra. *J. Geophys. Res.*, in press. doi:10.1029/2009JE003469.
- Fienga, A., Laskar, J., Morley, T., Manche, H., Kuchynka, P., Le Poncin-Lafitte, C., Budnik, F., Gastineau, M., Somenzi, L., 2009a. INPOP08, a 4-D planetary ephemeris: From asteroid and time-scale computations to ESA Mars Express and Venus Express contributions. *Astron. Astrophys.* 507 (3), 1675–1686. doi:10.1051/0004-6361/200911755.
- Fienga, A., Laskar, J., Kuchynka, P., Leponcin-Lafitte, C., Manche, H., Gastineau, M., 2009b. Gravity tests with INPOP planetary ephemerides. *Proc. Int. Astron. Union* 5, 159–169. doi:10.1017/S1743921309990330.
- Folkner, W.M., Yoder, C.F., Yuan, D.N., Standish, E.M., Preston, R.A., 1997. Interior structure and seasonal mass redistribution of Mars from radio tracking of Mars Pathfinder. *Science* 278, 1749–1752.
- Folkner, W.M., Williams, J.G., Boggs, D.H., 2009. The Planetary and Lunar Ephemeris DE 421. *JPL Interplanetary Network Progress Report*, 42-17. <[http://ipnpr.jpl.nasa.gov/progress\\_report/42-17/178C.pdf](http://ipnpr.jpl.nasa.gov/progress_report/42-17/178C.pdf)>.
- Forget, F., Hourdin, F., Fournier, R., Hourdin, C., Talagrand, O., Collins, M., Lewis, S.R., Read, P.L., Huot, J., 1999. Improved general circulation models of the martian atmosphere from the surface to above 80 km. *J. Geophys. Res.* 104 (13), 24155–24176. doi:10.1029/1999JE001025.
- Forsyth, D.W., 1985. Subsurface loading and estimates of the flexural rigidity of continental lithosphere. *J. Geophys. Res.* 90 (B4), 12623–12632.
- Frey, H.V., 2006. Impact constraints on, and a chronology for, major events in early Mars history. *J. Geophys. Res.* 111, E08S91. doi:10.1029/2005JE002449.
- Frey, H., Sakimoto, S.E.H., Roark, J.H., 1999. Discovery of a 450 km diameter, multi-ring basin on Mars through analysis of MOLA topographic data. *Geophys. Res. Lett.* 26 (12), 1657–1660.
- Haberle, R.M., Joshi, M.M., Murphy, J.R., Barnes, J.R., Schofield, J.T., Wilson, G., Lopez-Valverde, M., Hollingsworth, J.L., Bridger, A.F.C., Schaeffer, J., 1999. General circulation model simulations of the Mars Pathfinder atmospheric structure investigation/meteorology data. *J. Geophys. Res.* 104 (E4), 8957–8974.
- Haberle, R.M., Forget, F., Colaprete, A., Schaeffer, J., Boynton, W.V., Kelly, N.J., Chamberlain, M.A., 2008. The effect of ground ice on the martian seasonal CO<sub>2</sub> cycle. *Planet. Space Sci.* 56, 251–255.
- Heiskanen, W.A., Moritz, H., 1967. *Physical Geodesy*. W.H. Freeman and Company, San Francisco and London.
- Jacobson, R.A., 2007. The orbits of the martian satellites. In: *First International Conf. on the Exploration of Phobos and Deimos*. NASA Ames Research Center, Moffett Field, CA. LPI Contribution No. 1377, Lunar and Planetary Institute, Houston, TX.
- Jacobson, R.A., 2010. The orbits and masses of the martian satellites and the libration of Phobos. *Astron. J.* 139, 668–679. doi:10.1088/0004-6256/139/2/668.
- Jacobson, R.A., Rush, B., 2006. Ephemerides of the Martian Satellites – MAR063. *JPL Internal Document* 343R-06-004. Jet Propulsion Laboratory, Pasadena, CA.
- Jacobson, R.A., Synnott, S.P., Campbell, J.K., 1989. The orbits of the satellites of Mars from spacecraft and earthbased observations. *Astron. Astrophys.* 225 (2), 548–554.
- Justus, C.J., Johnson, D.L., James, B.F., 1996. A revised thermosphere for the Mars Global Reference Atmospheric Model (Mars-GRAM version 3.4). *NASA Tech. Memo.*, 108513.
- Kahn, R.A., Martin, T.Z., Zurek, R.W., Lee, S.W., 1992. The martian dust cycle. In: Kieffer, H.H., Jakosky, B.M., Snyder, C.W., Matthews, M.S. (Eds.), *Mars*. Univ. Ariz. Press, Tucson, pp. 1018–1953.
- Karatekin, O., Duron, J., Rosenblatt, P., Van Hoolst, T., Dehant, V., 2005. Mars' time-variable gravity and its determination: Simulated geodesy experiments. *J. Geophys. Res.* 110, E06001. doi:10.1029/2004JE002378.
- Karatekin, Ö., Van Hoolst, T., Tastet, J., de Viron, O., Dehant, V., 2006. The effects of seasonal mass redistribution and interior structure on Length-of-Day variations of Mars. *Adv. Space Res.* 38 (4), 739–744. doi:10.1016/j.asr.2006.04.01301R1.
- Kaula, W.M., 1966. *Theory of Satellite Geodesy*. Blaisdell, Waltham, MA.
- Khan, A., Connolly, J.A.D., 2008. Constraining the composition and thermal state of Mars from inversion of geophysical data. *J. Geophys. Res.* 113, E07003. doi:10.1029/2007JE002996.
- Kieffer, H.H., Titus, T.N., 2001. TES mapping of the Mars north seasonal cap. *Icarus* 154, 162–180. doi:10.1006/icar.2001.6670.
- Kieffer, H.H., Titus, T.N., Mullins, K.F., Christensen, P.R., 2000. Mars south polar spring and summer behavior observed by TES: Seasonal cap evolution controlled by frost grain size. *J. Geophys. Res.* 105, 9653–9699.
- Konopliv, A.S., Binder, A.B., Hood, L.L., Kucinskas, A.B., Williams, J.G., 1998. Improved gravity field of the Moon from lunar prospector. *Science* 281, 1476–1480.
- Konopliv, A.S., Banerdt, W.B., Sjogren, W.L., 1999. Venus gravity: 180th degree and order model. *Icarus* 139, 3–18.
- Konopliv, A.S., Miller, J.K., Owen, W.M., Yeomans, D.K., Giorgini, J.D., Garmier, R., Barriot, J.P., 2002. A global solution for the gravity field, rotation, landmarks, and ephemeris of Eros. *Icarus* 160, 289–299.
- Konopliv, A.S., Yoder, C.F., Standish, E.M., Yuan, D.N., Sjogren, W.L., 2006. A global solution for the Mars static and seasonal gravity, Mars orientation, Phobos and Deimos masses, and Mars ephemeris. *Icarus* 182, 23–50.
- Kuchynka, P., Laskar, J., Fienga, A., Manche, H., Somenzi, L., 2009. Improving the asteroids perturbations modeling in planetary ephemerides. In: Soffel, M., Capitaine, N. (Eds.), *Astrometry, Geodynamics, and Astronomical Reference Systems, Proc. of Journées-2008*. Dresden, pp. 84–85.
- Lambeck, K., 1980. *The Earth's Variable Rotation: Geophysical Causes and Consequences*. Cambridge University Press, Berlin, pp. 13–22.
- Lambert, S.B., Le Poncin-Lafitte, C., 2009. Determining the relativistic parameter  $\gamma$  using very long baseline interferometry. *Astron. Astrophys.* 499, 331–335.
- Lawson, C.L., Hanson, R.J., 1995. *Solving Least Squares Problems*. SIAM Classics in Applied Mathematics, vol. 15. Society for Industrial and Applied Mathematics, Philadelphia.
- Lebach, D.E., Corey, B.E., Shapiro, I.I., Ratner, M.I., Webber, J.C., Rogers, A.E.E., Davis, J.L., Herring, T.A., 1995. Measurement of the solar gravitational deflection of radio waves using very-long-baseline interferometry. *Phys. Rev. Lett.* 75, 1439–1442.
- Lemoine, F.G., 1992. *Mars: The Dynamics of Orbiting Satellites and Gravity Model Development*. Ph.D. Thesis, Univ. of Colo., Boulder.
- Lemoine, F.G., Smith, D.E., Rowlands, D.D., Zuber, M.T., Neumann, G.A., Chinn, D.S., 2001. An improved solution of the gravity field of Mars (GMM-2B) from Mars Global Surveyor. *J. Geophys. Res.* 106, 23359–23376.
- Lemoine, F.G., Bruinsma, S., Chinn, D.S., Forbes, J.M., 2006. Thermospheric studies with Mars Global Surveyor. In: *AIAA/AAS Astrodynamics Specialist Conference*, Keystone, CO. Paper AIAA 2006-6395, 1–13.
- Litvak, M.L., Mitrofanov, I.G., Kozyrev, A.S., Sanin, A.B., Tretyakov, V.I., Boynton, W.V., Shinohara, C., Hamara, D., Saunders, R.S., Drake, M., 2004. Seasonal carbon dioxide depositions on the martian surface as revealed from neutron measurements by the HEND instrument onboard the 2001 Mars Odyssey Spacecraft. *Solar Syst. Res.* 38, 167–177. doi:10.1023/B:SOLS.0000030856.83622.17.
- Litvak, M.L., Mitrofanov, I.G., Kozyrev, A.S., Sanin, A.B., Tretyakov, V.I., Boynton, W.V., Hamara, D., Shinohara, C., Saunders, R.S., 2005. Modeling of martian seasonal caps from HEND/ODYSSEY data. *Adv. Space Res.* 36 (11), 2156–2161. doi:10.1016/j.asr.2005.09.007.
- Litvak, M.L., Mitrofanov, I.G., Kozyrev, A.S., Sanin, A.B., Tretyakov, V.I., Boynton, W.V., Kelly, N.J., Hamara, D., Shinohara, C., Saunders, R.S., 2006. Comparison between polar regions of Mars from HEND/Odyssey data. *Icarus* 180, 23–37. doi:10.1016/j.icarus.2005.08.009.
- Malin, M.C., Caplinger, M.A., Davis, S.D., 2001. Observational evidence for an active surface reservoir of solid carbon dioxide on Mars. *Science* 294, 2146–2148.

- Marty, J.C., Balmino, G., Rosenblatt, P., Duron, J., LeMaistre, S., Rivoldini, A., Dehant, V., Van Hoolst, T., 2009. Martian gravity field model and its time variations from MGS and Odyssee data. *Planet. Space Sci.* doi:10.1016/j.pss.2009.01.004.
- Matson, D.L., Veeder, G.J., Tedesco, F.F., Lebofsky, L.A., Walker, R.G., 1986. IRAS survey of asteroids. *Adv. Space Res.* 6, 41–56.
- Matsuo, K., Heki, K., 2009. Seasonal and inter-annual changes of volume density of the martian CO<sub>2</sub> snow from time-variable elevation and gravity. *Icarus*. doi:10.1016/j.icarus.2009.02.023.
- Mazarico, E.M., Zuber, M.T., Lemoine, F.G., Smith, D.E., 2007. Atmospheric density during the aerobraking of Mars Odyssey from radio tracking data. *J. Spacecraft Rockets* 44, 1165–1171.
- Mazarico, E.M., Zuber, M.T., Lemoine, F.G., Smith, D.E., 2009. Effects of self-shadowing on nonconservative force modeling for Mars-orbiting spacecraft. *J. Spacecraft Rockets* 46 (3), 662–669. doi:10.2514/1.41679.
- McDunn, T.L., Bougher, S.W., Murphy, J., Smith, M.D., Forget, F., Bertaux, J.-L., Montmessin, F., 2010. Simulating the density and thermal structure of the middle atmosphere (80–130 km) of Mars using the MGCM–MTGCM: A comparison with MEX/SPICAM observations. *Icarus* 206, 5–17.
- McGovern, P.J., Solomon, S.C., Smith, D.E., Zuber, M.T., Simons, M., Wieczorek, M.A., Phillips, R.J., Neumann, G.A., Aharonson, O., Head, J.W., 2002. Localized gravity/shape admittance and correlation spectra on Mars: Implications for regional and global evolution. *J. Geophys. Res.* 107. doi:10.1029/2002JE001854.
- McGovern, P.J., Solomon, S.C., Smith, D.E., Zuber, M.T., Simons, M., Wieczorek, M.A., Phillips, R.J., Neumann, G.A., Aharonson, O., Head, J.W., 2004. Correction to “Localized gravity/topography admittances and correlation spectra on Mars: Implications for regional and global evolution”. *J. Geophys. Res.* 109. doi:10.1029/2004JE002286.
- Metivier, L., Karatekin, O., Dehant, V., 2008. The effect of the internal structure of Mars on its seasonal loading deformations. *Icarus* 194, 476–486.
- Moyer, T.D., 1971. Mathematical Formulation of the Double-Precision Orbit Determination Program (DPODP). JPL Technical Report 32-1527. Jet Propulsion Laboratory, California Institute of Technology, Pasadena, CA.
- Moyer, T.D., 2000. Formulation for Observed and Computed Values of Deep Space Network Data Types for Navigation. DESCANSO Monograph 2. JPL Publication 00-7. Jet Propulsion Laboratory, California Institute of Technology, Pasadena, CA. <[http://descanso.jpl.nasa.gov/Monograph/series2/Descanso2\\_all.pdf](http://descanso.jpl.nasa.gov/Monograph/series2/Descanso2_all.pdf)>.
- Neumann, G.A., Zuber, M.T., Wieczorek, M.A., McGovern, P.J., Lemoine, F.G., Smith, D.E., 2004. Crustal structure of Mars from gravity and topography. *J. Geophys. Res.* 109, E08002. doi:10.1029/2002JE002262.
- Nimmo, F., 2002. Admittance estimates of mean crustal thickness and density at the martian hemispheric dichotomy. *J. Geophys. Res.* 107. doi:10.1029/2000JE001488.
- Nunes, D.C., Smrekar, S.E., Konopliv, A.S., 2009. Survey of gravity admittance for Mars from the High-Resolution Mars Reconnaissance Orbiter data. *Lunar Planet. Sci.* 40. Abstract 2011.
- Piqueux, S., Christensen, P.R., 2008. Deposition of CO<sub>2</sub> and erosion of the martian south perennial cap between 1972 and 2004: Implications for current climate change. *J. Geophys. Res.* 113, E02006. doi:10.1029/2007JE002969.
- Pitjeva, E., 2005. Relativistic effects and solar oblateness from radar observations of planets and spacecraft. *Astron. Lett.* 31 (5), 340–349.
- Pitjeva, E., 2008. Ephemerides EPM2008: The updated model, constants, and data. In: *Proceedings Journées 2008: Space-Time Reference Systems*, 22–24 September 2008, Dresden, pp. 57–60.
- Prettyman, T.H. et al., 2004. Composition and structure of the martian surface at high southern latitudes from neutron spectroscopy. *J. Geophys. Res.* 109, E05001. doi:10.1029/2003JE002139.
- Prettyman, T.H., Feldman, W.C., Titus, T.N., 2009. Characterization of Mars’ seasonal caps using neutron spectroscopy. *J. Geophys. Res.* 114, E08005. doi:10.1029/2008JE00327.
- Reasenberg, R.D., 1977. The moment of inertia of Mars and isostasy of Mars. *J. Geophys. Res.* 82, 369–375.
- Reasenberg, R.D., King, R.W., 1979a. The rotation of Mars. *J. Geophys. Res.* 84, 6231–6240.
- Reasenberg, R.D., Shapiro, I.I., MacNeil, P.E., Goldstein, R.B., Briedenthal, J.C., Brinkle, J.P., Cain, D.L., Kaufman, T.M., Komarek, T.A., Zygielbaum, A.L., 1979b. Viking relativity experiment: Verification of signal retardation by solar gravity. *Astrophys. J.* 234, L219–L221.
- Redman, J.C., Fish, F.F., 1964. The luni-tidal interval in Mars and the secular acceleration of Phobos. *Icarus* 3, 87–91.
- Ries, J.C., Eanes, R.J., Shum, C.K., Watkins, M.M., 1992. Progress in determination of the gravitational coefficient of the Earth. *Geophys. Res. Lett.* 19 (6), 529–531.
- Robertson, D.S., Carter, W.E., 1984. Relativistic deflection of radio signals in the solar gravitational field measured with VLBI. *Nature* 310, 572–574.
- Robertson, D.S., Carter, W.E., Dillinger, W.H., 1991. New measurement of solar gravitational deflection of radio signals using VLBI. *Nature* 349, 768–770.
- Sanchez, B.V., Rowlands, D.D., Haberle, R.M., Schaeffer, J., 2003. Atmospheric rotational effects on Mars based on the NASA Ames general circulation model. *J. Geophys. Res.* 108. doi:10.1029/2002JE001984.
- Sanchez, B.V., Rowlands, D.D., Haberle, R.M., 2006. Variations of Mars gravitational field based on the NASA/Ames general circulation model. *J. Geophys. Res.* 111, E06010. doi:10.1029/2005JE002442.
- Seidelmann, P.K. et al., 2002. Report of the IAU/IAG working group on cartographic coordinates and rotational elements of the planets and satellites: 2000. *Celest. Mech. Dynam. Astron.* 82, 83–110.
- Semenov, B.V., Acton, C.H., 2007. Mars Reconnaissance Orbiter Spice Kernels V1.0. MRO-M-SPICE-6-V1.0. NASA Planetary Data System.
- Semenov, B.V., Elson, L.S., Acton, C.H., 1998. Mars Global Surveyor Spice Kernels V1.0. MGS-M-SPICE-6-V1.0. NASA Planetary Data System.
- Semenov, B.V., Elson, L.S., Acton, C.H., 2004. Odyssey Spice Kernels V1.0. ODY-M-SPICE-6-V1.0. NASA Planetary Data System.
- Shapiro, I.I., 1964. Fourth test of general relativity. *Phys. Rev. Lett.* 13, 789–791.
- Shapiro, S.S., Davis, J.L., Lebach, D.E., Gregory, J.S., 2004. Measurement of the solar gravitational deflection of radio waves using geodetic very-long-baseline interferometry data, 1979–1999. *Phys. Rev. Lett.* 92, 121101.
- Simons, M., Solomon, S.C., Hager, B.H., 1997. Localization of gravity and topography: Constraints on the tectonics and mantle dynamics of Venus. *Geophys. J. Int.* 131, 24–44.
- Smith, D.E., Sjogren, W.L., Tyler, G.L., Balmino, G., Lemoine, F.G., Konopliv, A.S., 1999a. The gravity field of Mars: Results from Mars Global Surveyor. *Science* 286, 94–97.
- Smith, D.E., Zuber, M.T., Haberle, R.M., Rowlands, D.D., Murphy, J.R., 1999b. The Mars seasonal CO<sub>2</sub> cycle and the time variation of the gravity field: A general circulation model simulation. *J. Geophys. Res.* 104, 1885–1896.
- Smith, D.E. et al., 1999c. The global topography of Mars and implications for surface evolution. *Science* 284, 1495–1503.
- Smith, D.E., Zuber, M.T., Neumann, G.A., 2001a. Seasonal variations of snow depth on Mars. *Science* 294, 2141–2146.
- Smith, D.E. et al., 2001b. Mars Orbiter Laser Altimeter: Experiment summary after the first year of global mapping of Mars. *J. Geophys. Res.* 106, 23689–23722.
- Smith, M.D., Pearl, J.C., Conrath, B.J., Christensen, P.C., 2001c. Thermal Emission Spectrometer results: Mars atmospheric thermal structure and aerosol distribution. *J. Geophys. Res.* 106, 23929–23945.
- Smith, D.E., Zuber, M.T., Torrence, M.H., Dunn, P.J., Neumann, G.A., Lemoine, F.G., Fricke, S.K., 2009. Time variations of Mars’ gravitational field and seasonal changes in the masses of the polar ice caps. *J. Geophys. Res.* 114, E05002. doi:10.1029/2008JE003267.
- Smrekar, S.E., 1994. Evidence for active hotspots on Venus from analysis of Magellan gravity data. *Icarus* 112, 2–26.
- Sohl, F., Schubert, G., Spohn, T., 2005. Geophysical constraints on the composition and structure of the martian interior. *J. Geophys. Res.* 110, E12008. doi:10.1029/2005JE002520.
- Standish, E.M., 1990. The observational basis for JPL’s DE 200, the planetary ephemerides of the astronomical almanac. *Astron. Astrophys.* 233, 252–271.
- Standish, E.M., 1998. Time scales in the JPL and CfA ephemerides. *Astron. Astrophys.* 336, 381–384.
- Turcotte, D.L., Sherbatkov, R., Malamud, B.D., Kucinkas, A.B., 2002. Is the martian crust also the martian elastic lithosphere? *J. Geophys. Res.* 107, 1–20.
- Van den Acher, E., Van Holst, T., deViron, O., Defraigne, P., Forget, F., Hourdin, F., Dehant, V., 2002. Influence of winds and the CO<sub>2</sub> mass exchange between the atmosphere and the polar caps on Mars rotation. *J. Geophys. Res.* 107. doi:10.1029/2000JE001539.
- Wieczorek, M.A., Zuber, M.T., 2004. Thickness of the martian crust: Improved constraints from geoid-to-topography ratios. *J. Geophys. Res.* 109, E01009. doi:10.1029/2003JE002153.
- Williams, J.G., 1984. Determining asteroid masses from perturbations on Mars. *Icarus* 57, 1–13.
- Williams, J.G., Boggs, D.H., 2009. Lunar core and mantle. What does LLR see? In: Schilliak, S. (Ed.), *Proc. 16th Int. Workshop on Lunar Laser Ranging*, Poznan, Poland, October 2008, pp. 101–120.
- Williams, J.G., Turyshev, S.G., Boggs, D.H., 2004. Progress in lunar laser ranging tests of relativistic gravity. *Phys. Rev. Lett.* 93, 261101.
- Williams, J.G., Turyshev, S.G., Boggs, D.H., 2009. Lunar laser ranging tests of the equivalence principle with the Earth and Moon. *Int. J. Modern Phys. D* 18 (7), 1129–1175. doi:10.1142/S021827180901500X.
- Withbroe, G.L., Noyes, R.W., 1977. Mass and energy flow in the solar chromosphere and corona. *Annu. Rev. Astron. Astrophys.* 15, 363–387.
- Yoder, C.F., 1982. Tidal rigidity of Phobos. *Icarus* 49, 327–346.
- Yoder, C.F., 1995. Venus’ free obliquity. *Icarus* 117, 250–286.
- Yoder, C.F., Standish, E.M., 1997. Martian precession and rotation from Viking lander range data. *J. Geophys. Res.* 102 (E2), 4065–4080.
- Yoder, C.F., Konopliv, A.S., Yuan, D.N., Standish, E.M., Folkner, W.M., 2003. Fluid core size of Mars from detection of the solar tide. *Science* 300, 299–303.
- You, H., Halsell, A., Graat, E., Demcak, S., Highsmith, D., Long, S., Bhat, R., Mottinger, N., Higa, E., Jah, M., 2007. Mars Reconnaissance Orbiter interplanetary cruise navigation. In: *20th Int. Symp. on Space Flight Dyn.*, Annapolis, MD, 1–16.
- Yuan, D.N., 1991. The Determination and Error Assessment of the Earth’s Gravity Field Model. Ph.D. Thesis, Univ. of Tex. at Austin.
- Yuan, D.N., Sjogren, W.L., Konopliv, A.S., Kucinkas, A.B., 2001. Gravity field of Mars: A 75th degree and order model. *J. Geophys. Res.* 106, 23377–23401.
- Zuber, M.T. et al., 2000. Internal structure and early thermal evolution of Mars from Mars Global Surveyor topography and gravity. *Science* 287, 1788–1793.
- Zuber, M.T., Lemoine, F.G., Smith, D.E., Konopliv, A.S., Smrekar, S.E., Asmar, S.W., 2007. Mars Reconnaissance Orbiter radio science investigation. *J. Geophys. Res.* 112, E05S07. doi:10.1029/2006JE002833.